

DEFECT ENGINEERING OF ELECTROCERAMICS: BISMUTH TRIIODIDE AND
BARIUM TITANATE

By

HYUKSU HAN

A DISSERTATION PRESENTED TO THE GRADUATE SCHOOL
OF THE UNIVERSITY OF FLORIDA IN PARTIAL FULFILLMENT
OF THE REQUIREMENTS FOR THE DEGREE OF
DOCTOR OF PHILOSOPHY

UNIVERSITY OF FLORIDA

2014

© 2014 HyukSu Han

To my future self

ACKNOWLEDGMENTS

At the very first, I sincerely appreciate my advisor Dr. Juan C. Nino for his support and guidance. His knowledge, care, optimism, diligence, and aspirations inspired me to work hard and expand my potential. In addition, I am also deeply grateful to my other committee members (Dr. Kelly Jordan, Dr. James Baciak, Dr. Yong Yang, and Dr. Jason Weaver) for their guidance.

I would like to acknowledge all the collaborators who significantly improved my research: Dr. Susan B. Sinnott and Dr. Minki Hong for their great help on all the computational work, Dr. Dipankar Ghosh, Dr. Jacob L. Jones, Dr. Sophie Guillemet-Fritsch, and Dr. Christophe Voisin for their contributions on the synthesis of dielectric materials and analysis of dielectric properties. I also want to acknowledge Mr. Rudy Strohschein from Southern Scientific, Inc. for his glass-ware work. I would like to thank the people who were involved and helped me through the entire project, Dr. Valentin Craciun, Dr. Tanner, Dr. Burger, Dr. Holland Smith, and Evan Thatcher.

I deeply thank the current and previous NRG group members: Dr. Wei Qui, Dr. Beverly Hinojosa, Dr. Wei Zhou, Roberto Esquivel-Elizondo, Donald Moore, Luping Li, Robert Kasse, Chris Turner, Trey Davis, George Baure, Mehrad Mehr, Sasmit Gokhale, and etc., for providing me with an excellent research environment and being helpful.

Last but not least, I want to give my special thanks to my parents and my friends (KeKis) for their loving encouragement. Their love has encouraged me to endure the hard times. I cannot imagine myself having any of my progress without their strong support behind me.

TABLE OF CONTENTS

	<u>page</u>
ACKNOWLEDGMENTS.....	4
LIST OF TABLES.....	8
LIST OF FIGURES.....	9
LIST OF ABBREVIATIONS.....	12
ABSTRACT.....	13
CHAPTER	
1 INTRODUCTION.....	15
1.1 Statement of Problem and Motivation.....	15
1.2 Scientific Approach.....	16
1.3 Organization of Dissertation.....	19
1.4 Contributions to the Field.....	20
2 BACKGROUND.....	23
2.1 Defect Chemistry.....	23
2.1.1 The Kröger – Vink Notation.....	23
2.1.2 Intrinsic Point Defect Reactions in Stoichiometric Compounds: Schottky and Frenkel.....	24
2.1.3 Diffusion and Electrical Conductivity.....	30
2.2 Dielectric Polarizations in Solids.....	34
2.2.1 Polarization Mechanisms.....	35
2.2.2 Space Charge Polarization.....	38
2.2.2.1 Hopping polarization.....	39
2.2.2.2 Interfacial polarization.....	40
2.2.3 The Universal Dielectric Response.....	41
2.3 Crystal Structures of BiI_3 and BaTiO_3	45
2.3.1 BiI_3	45
2.3.2 BaTiO_3	47
3 EXPERIMENTAL PROCEDURES AND PROCESSING.....	52
3.1 Sample Preparation.....	52
3.1.1 BiI_3 Single Crystals.....	52
3.1.1.1 PVT powder synthesis technique.....	52
3.1.1.2 TMZ purification technique.....	53
3.1.1.3 Single crystal growth of Te and Sb doped BiI_3	54
3.1.2 BaTiO_3 Ceramics.....	55

3.1.2.1	Microwave sintering	55
3.1.2.2	Spark plasma sintering.....	55
3.1.2.3	Conventional pressureless sintering	56
3.2	Characterization.....	57
3.2.1	X-ray Diffraction.....	57
3.2.2	Scanning Electron Microscopy	57
3.2.3	X-ray Photoelectron Spectroscopy	58
3.2.4	Inductively Coupled Plasma – Atomic Emission Spectroscopy	58
3.2.5	Dielectric Characterization.....	58
3.2.6	Electrical Property Characterization	59
3.2.7	Radiation Response Measurement	60
3.2.8	Computational Methods.....	60
4	ENHANCED ELECTRICAL PROPERTIES AND RADIATION RESPONSE OF ULTRA PURE BISMUTH TRI-IODIDE SINGLE CRYSTAL DETECTORS	61
4.1	Introduction	61
4.2	Ultra High Pure BiI ₃ Powder Synthesis by PVT and TMZ Techniques.....	61
4.3	Electrical Properties and Radiation Response of Ultra-Pure BiI ₃ Single Crystal Detectors	62
4.4	Conclusion	65
5	DEFECT MODELING AND ENGINEERING OF BISMUTH TRI-IODIDE SINGLE CRYSTALS: ENHANCED ELECTRICAL AND RADIATION DETECTION PERFORMANCE	67
5.1	Introduction	67
5.2	Defect Modeling of BiI ₃ Single Crystals: Donor (Te) Doped BiI ₃	67
5.3	Defect Engineering of BiI ₃ Single Crystals: Sb doped BiI ₃ Single Crystal.....	72
5.4	Enhanced Electrical and Radiation Performance of Sb doped BiI ₃ Single Crystal Detectors for Room Temperature Gamma-Ray Detection.....	81
5.5	Conclusion	86
6	COLOSSAL PERMITTIVITY IN FAST-FIRED BARIUM TITANATE CERAMICS ...	88
6.1	Introduction	88
6.2	Microstructure, Density, and Phase Purity of Pressureless, Spark-Plasma, and Microwave-Sintered BaTiO ₃	89
6.3	Dielectric Properties of Pressureless, Spark-Plasma, and Microwave- Sintered BaTiO ₃	93
6.4	Effect of Annealing on Dielectric Properties of Microwave-Sintered BaTiO ₃ Ceramics	97
6.5	Conclusion	102
7	DIELECTRIC POLARIZATION MECHANISMS AND VARIABLE HOPPING CONDUCTION IN FAST-FIRED BARIUM TITANATE CERAMICS.....	103
7.1	Introduction	103

7.2 Microstructure, Density, and XRD of Spark Plasma Sintered BaTiO ₃ Using Co-Precipitated Nanocrystalline Powder	103
7.3 Broadband Dielectric Spectroscopy and Polarization Mechanism Investigation on Colossal Permittivity of Barium Titanate Ceramics	106
7.4 Variable Range Hopping Conduction in Barium Titanate Ceramics Exhibiting Colossal Permittivity	118
7.5 Tailoring Contributions of Each Polarization Mechanism to Colossal Permittivity of Barium Titanate Ceramics.....	127
7.6 Conclusion	131
8 SUMMARY AND FUTURE WORK	133
8.1 Summary	133
8.1.1 Defects and Electrical Property Relationships in BiI ₃	133
8.1.2 Colossal Permittivity in Fast-fired BaTiO ₃	134
8.2 Future Work	135
8.2.1 Defect Engineering of BiI ₃ : Controlling Atmospheric Pressure	135
8.2.2 Polarization Mechanism in (Nb+In) Co-doped TiO ₂ Ceramics Exhibiting Temperature-frequency Independent Colossal Permittivity	137
LIST OF REFERENCE.....	139
BIOGRAPHICAL SKETCH.....	149

LIST OF TABLES

<u>Table</u>	<u>page</u>
2-1 Experimentally determined Schottky defect formation enthalpy in Alkali halide compounds.....	28
2-2 Examples of Frenkel defect formation enthalpy.....	30
2-3 Defect characterization tools.	34
2-4 Examples for numerical values of the exponent "s" for different materials.	45
2-5 Crystal structure information for BiI ₃	47
2-6 Crystal structure information for tetragonal BT.	51
4-1 Impurity concentrations of PVT and TMZ synthesized BiI ₃ powder measured by using ICP-AES.....	62
5-1 Te ⁴⁺ substitutional donor dopant for Bi ³⁺	67
5-2 Summary of the dominant defect type and concentration for and the slope in the Log(T) vs. 1/T plot.	69
5-3 ICP-AES analysis on (a) BiI ₃ and (b) SBI single crystals.....	75
5-4 Sb-I and Bi-I bond lengths in Sb incorporated BiI ₃ on Bi-site.....	80
6-1 Summary of sintering conditions, densities, and dielectric properties.....	92
6-2 Dielectric properties and bulk resistivity of as-sintered MWS, SPS, and PS BT ceramics at room temperature and 1 kHz.	97
6-3 Effect of annealing on dielectric of MWS BT.....	101
6-4 Dielectric properties of the annealed MWS BT (950°C for 12 hours) with various electrodes (Au, Ag, Ni, and Al) at room temperature and 1 kHz.	101
7-1 Summary of chemical composition, grain size and relative density of the sintered ceramics.	105
7-2 Dielectric property of SPS BT 0.95 and 1.00 at room temperature and 1, 10, and 100 kHz.	108
7-3 Related fitting parameters for the SPS BT using Koop's equivalent circuit model.....	129

LIST OF FIGURES

<u>Figure</u>	<u>page</u>
2-1 Representative defects in MO oxide.....	26
2-2 Schematics of four main polarization mechanisms.....	37
2-3 Contributions of each polarization mechanism to the total relative permittivity as a function of frequency.	38
2-4 Hopping polarization due to the hopping of the charged particle over the barrier from one site to the other.	39
2-5 A dielectric material comprising of two different components.	40
2-6 Examples of dielectric behaviors departed from the Debye theory.....	43
2-7 Schematic representations of the two types of dielectric response.	44
2-8 Polyhedral schematic for corner sharing octahedra in BiI ₃ and empty octahedral sites in one I-Bi-I layer.	47
2-9 Crystal structure of BT.....	48
2-10 Phase transformation and relative permittivity change of BT.....	50
2-11 Approximate ion displacements in tetragonal BT.....	51
4-1 IV characteristics of the PVT and commercial BiI ₃ detectors.....	63
4-2 Leakage current comparison between PVT and commercial BiI ₃ detectors.	64
4-3 ²⁴¹ Am α -particle spectrum recorded from the ultra-pure PVT BiI ₃ detector at room temperature.	65
5-1 Anticipated slopes in Log(σ T) vs. Temp plot for donor doped BiI ₃	70
5-2 Te doped BiI ₃ single crystal.	70
5-3 ICP analysis for Te concentrations along the distance from the tip.	71
5-4 Ionic conductivity of Te doped BiI ₃ single crystals as a function of temperature.	72
5-5 XRD patterns for BiI ₃ and SBI single crystals.	74
5-6 Calculated formation energies as a function of Fermi energy.....	77

5-7	Crystal structures of SBI and total density of states (DOS) for SBI and pure BiI_3	79
5-8	Electrical properties of BiI_3 and SBI single crystal detectors.....	82
5-9	^{241}Am alpha source radiation response tests for single crystal detectors under bias at different time periods.	84
5-10	Electron rise time of the SBI detector from alpha particles.	86
6-1	SEM micrographs of starting nano powder and fractured surfaces.	90
6-2	MWS BT annealed in air at different temperatures and times (1050°C for 12 h, 1100°C for 24 h, 1250°C for 24 h from left to right).	91
6-3	XRD patterns of nano powder, as-sintered PS, MWS, SPS, and annealed MWS BT.	93
6-4	Dielectric properties of as-sintered BT at 1, 10, 100, 500 kHz, and 1 MHz.	95
6-5	Effect of annealing on the dielectric properties of MWS BT (at 1 kHz and room temperature).....	98
6-6	Dielectric properties (at 1 kHz) of MWS BT with different annealing temperatures (1050°C, 1000°C, and 900°C) for 12 hrs.	100
6-7	Dielectric properties of MWS BT annealed at 950°C for 12 hrs as a function of frequency in the temperature range from room temperature (27°C) to (-233°C).	101
7-1	SEM images for SPS 0.95 and SPS 1.00 sintered ceramics.....	104
7-2	The X-ray diffraction patterns for the starting powders (BT 1.00 and 0.95) and the sintered ceramics (SPS BT 1.00 and 0.95).....	105
7-3	Dielectric property of SPS BT as a function of temperature (20 ~ 300 K).....	107
7-4	Activation energy of thermally activated relaxations.	109
7-5	$\text{Log}_{10}(\epsilon''f)$ vs. $\text{log}_{10}f$ plot for the SPS (1150°C) BT at different temperatures (30 K ~ 300 K).	112
7-6	Dielectric properties of SPS BT 0.95 sample as a function of frequency (40 Hz – 1 MHz) at different temperatures (40 K – 300 K).....	113
7-7	Dielectric properties of SPS BT 0.95.	115
7-8	The imaginary part of the relative permittivity changes for SPS BT 0.95 as a function of frequencies (40 Hz ~ 1 MHz) at 300 K ~ 100 K.....	117

7-9	Activation energy for polaron hopping polarization at 300 K ~ 200 K.	118
7-10	Dielectric properties and conductivity of SPS BT as a function of frequency (1 kHz ~ 4 MHz) at different temperatures (110 K ~ 220 K).....	121
7-11	Temperature dependence of dc conductivity (σ_{dc}) with respect to $1/T$ and $1/T^{1/2}$. Black lines are the linear fits of the data.....	125
7-12	Activation energies and hopping distance as a function of temperature for VRH conduction in SPS BT.	127
7-13	Experimental data with fitting data of the real and imaginary part of permittivity for SPS BT.	129
7-14	Interfacial and hopping polarization model for the colossal permittivity of BT ceramics.	131
8-1	Kroger-Vink diagram for iodine and bismuth vacancies with respect to iodine partial pressure.....	136

LIST OF ABBREVIATIONS

DFE	Defect Formation Energy
DFT	Density Functional Theory
DOS	Density of State
EIS	Electrochemical Impedance Spectroscopy
FWHM	Full Width at Half Maximum
IBLC	Inter Barrier Layer Capacitance
ICP-AES	Inductively Coupled Plasma – Atomic Emission Spectroscopy
LDA	Local Density Approximation
MCA	Multi Channel Analyzer
NIM	Nuclear Instrumentation Module
PAW	Projector Augmented Wave
PVT	Physical Vapor Transportation
SEM	Scanning Electron Microscope
SCCM	Standard Cubic Centimeters per Minute
SCFH	Standard Cubic Feet per Hour
T_c	Curie Temperature
TMZ	Traveling Molten Zone
UDR	Universal Dielectric Response
XRD	X-ray Diffraction

Abstract of Dissertation Presented to the Graduate School
of the University of Florida in Partial Fulfillment of the
Requirements for the Degree of Doctor of Philosophy

DEFECT ENGINEERING OF ELECTROCERAMICS: BISMUTH TRIIODIDE AND
BARIUM TITANATE

By

HyukSu Han

May 2014

Chair: Juan C. Nino

Major: Materials Science and Engineering

Defect engineering has a significant potential to improve materials' functional properties, and thus much attention has been focused on the defect-functionality relationships in the fields of materials science and engineering. Point defects in compounds have great impact on electrical properties of the material and the fabricated devices as well. The migration and concentration of point defects are two key parameters being attributed to functional properties of the compound. These parameters can be optimized by intentionally introducing extrinsic defects (i.e. dopants) or changing processing conditions (i.e. temperature and time). In this work, the defect-electrical property relationships were investigated for two different materials (BiI_3 and BaTiO_3).

BiI_3 is a promising material as room temperature gamma-ray detector due to its high atomic number, high density, and wide bandgap. However, the high concentration and mobility of iodine vacancies in the compound increases the leakage current in the device and degrades detector performance. Thus, defect engineering has a potential to resolve this problem and improve the electrical properties of the detector. BaTiO_3 is a one of the best dielectric material in the world. Recently, it has been reported that fast-

fast-fired BaTiO₃ shows abnormally high relative permittivity due to induced defect dipoles. However, the precise defect dipole polarization mechanisms acting in fast-fired BaTiO₃ ceramics have not been understood, and therefore here a comprehensive investigation was performed to reveal the polarization mechanisms associated with defect dipoles in fast-fired BaTiO₃.

CHAPTER 1 INTRODUCTION

1.1 Statement of Problem and Motivation

In the modern microelectronics industry, attention has been focused on modifying the functionality of materials in order to optimize their electrical, optical, magnetic, and mechanical properties.¹⁻³ These functional properties are significantly influenced by various dimensional defects in the material such as vacancies, impurities, grain boundaries, dislocations, and pores, etc. Thus, in the field of microelectronics, a tremendous amount of studies have been conducted on the nature, concentration, and arrangement of defects, especially in semiconducting materials such as silicon (Si) and gallium-arsenide (GaAs), which have resulted in remarkable developments in modern electronic devices.⁴⁻¹¹

Recently, electroceramic compounds are receiving much attention as functional electronic materials in the fields of sensors and actuators, energy conversion and storage devices, and high-K dielectrics and ferroelectrics, given their high susceptibility with excellent thermal and mechanical stabilities.¹²⁻¹⁹ In electroceramics, optimization of many functional properties relies on precise control of the zero-dimensional defects in the material (i.e. point defects).²⁰⁻²⁷ However, only a few studies have been completed for electroceramic compounds on understating how point defects can affect the functionality of the material. Thus, the key objective of this dissertation is to investigate relationships between point defects and electrical properties of electroceramics studied here, bismuth tri-iodide (BiI_3) and barium titanate (BaTiO_3 , BT), and thus to provide defect engineering strategies for the compounds to further improve their functionalities.

1.2 Scientific Approach

BiI_3 is a promising material as room temperature semiconductor for gamma-ray radiation detectors given its high detection efficiency.²⁸⁻³⁰ However, to date the potential of BiI_3 as a semiconductor radiation detector compound has not been realized mainly due to its high ionic conductivity that can lead to degradation in detection performance over time.²⁸ At low and room temperature the ionic conduction of BiI_3 can be attributed to the high concentration of intrinsic defects, mainly iodine vacancies, resulting from the high volatility of iodine. The large number of intrinsic and/or extrinsic defects reduces the dark resistivity of BiI_3 and increases the leakage current and polarization effects, all of which consequently degrade radiation detection performance of the device.³¹⁻³⁵ Based on this, it is clear that limiting the formation and migration of the intrinsic and extrinsic defects is essential to enhance the electrical property of BiI_3 and realize its potential as a radiation detection material. Thus, defect engineering has the potential to mitigate the obstacles currently associated with the material.

In order to understand and control intrinsic defects in BiI_3 , a prevalent ionic conduction defect model of BiI_3 will be established by donor (tellurium, Te) doping. To reduce the formation and migration of iodine vacancies, antimony (Sb) dopants will be doped into BiI_3 based on crystallographic concepts. Details of the scientific approach for dopant selection are given in Chapter 5.2 and 5.3, respectively. Table 1-1 summarizes the main intrinsic defect reactions in BiI_3 and extrinsic defect reactions by external dopants that will be used to extract thermodynamic parameters for intrinsic defects of BiI_3 and to control iodine vacancy formation.

Table 1-1. Main intrinsic and extrinsic defect reactions in BiI₃.

Intrinsic defect reaction		Extrinsic defect reaction	
Shottky defect	$null \leftrightarrow V_{Bi}''' + 3V_I^\bullet$	Donor doping	$DI_{4_{BiI_3}} \leftrightarrow D_{Bi}^\bullet + 3I_I^X + e' + \frac{1}{2} I_2(g)$
Iodine volatilization	$I_I^X \leftrightarrow V_I^\bullet + e' + \frac{1}{2} I_2(g)$	Interstitial I doping	$2DI_3 \xleftrightarrow{BiI_3} D_I^{\bullet\bullet} + D_{Bi}^X + 3I_I^X + \frac{3}{2} I_2(g) + 2e'$

*D: Dopant

In order to prove this defect engineering strategy, pure BiI₃ and doped BiI₃ single crystals were grown by using a modified vertical Bridgman method with a previously optimized temperature profile (growth rate of 0.5 mm/h and temperature gradient of 10°C/cm).²⁹ Then, the grown single crystals were characterized by various techniques. The crystal structure and phase purity was determined using X-ray diffraction (XRD). The chemical composition and impurity concentration of the crystal were characterized by inductively coupled plasma – atomic emission spectroscopy (ICP-AES). Ionic conductivity was measured using two-point AC electrochemical impedance spectroscopy (EIS). I-V characterization was performed to determine bulk resistivity of the crystal. Leakage current and radiation response measurements were also performed on the fabricated single crystal detector. Density functional theory (DFT) calculations were employed to provide insight into the most energetically favorable site where Sb might be incorporated in BiI₃ lattice and how the dopants bond with surrounding ions. In addition, efforts were made to reduce extrinsic impurity defects in the crystal by purifying BiI₃ starting powder through physical vapor transportation (PVT) and travelling molten zone (TMZ) techniques.

As a second part of this dissertation, dielectric properties associated with point defects such as space charge were also investigated for BT compounds. Recently, an

unusual dielectric response has been reported for BT ceramics when synthesized through certain fast-firing processing techniques.³⁶ These studies indicate that abnormally high relative permittivity ($\epsilon_r' = 10^4 \sim 10^5$) with low dielectric loss ($\tan \delta < 0.05$) can be achieved in BT ceramics, and this extremely high relative permittivity has been referred to as colossal permittivity (CP).^{37,38} At first, it was originally thought that CP might be related to a new intrinsic polarization mechanism due to crystal structure and/or electrical charge ordering. However, recent investigations have revealed that CP can be possibly attributed to a well-known extrinsic Maxwell-Wagner (MW) polarization associated with induced point defects inside the material.^{36,39,40} However, there is an ongoing debate regarding the exact mechanisms and explanations for the origin of CP in BT ceramics.

In addition, while using fast-fired BT ceramics in conventional capacitive applications has been investigated, the strong temperature and frequency dependence of CP limits the use of fast-fired BT ceramics in actual applications.⁴¹⁻⁴⁸ It is widely accepted that the temperature and frequency dependence of CP is the result of extrinsic effects, such as interfacial polarization and hopping conduction, contributing to the bulk conductivity of the material.⁴⁹⁻⁵¹ Thus, understanding the fundamental mechanisms of the bulk conduction in fast-fired BT ceramics is essential for tailoring the temperature- and frequency-dependent dielectric response and fully realizing their potential.

In order to address these issues, the first step of this work is to synthesize BT ceramics exhibiting CP through fast-firing techniques such as spark plasma sintering (SPS) and microwave sintering (MWS). Processing variables, such as sintering and annealing conditions, were optimized to improve the dielectric properties of fast-fired BT

ceramics. For comparison purposes, BT ceramics were also sintered by a conventional pressureless sintering (PS) process. Then, the second step is to characterize dielectric properties of synthesized BT ceramics at different temperatures and frequencies via broadband dielectric spectroscopy. Measured dielectric data was analyzed following Debye relaxation and Jonscher's universal dielectric response (UDR) models to reveal polarization and conduction mechanisms in fast-fired BT ceramics. In addition, the contributions of each polarization mechanism to the relative permittivity and the conductivity of fast-fired BT ceramics were estimated based on corresponding analytical models.

1.3 Organization of Dissertation

Chapter 2 provides a brief introduction and background information on the defect chemistry in electroceramics. The correlations between the point defects and electrical properties are discussed. Chapter 2 also introduces the dielectric polarization mechanisms linked with point defects. A brief crystallographic overview and a summary of relevant physical properties of BiI_3 and BT are presented.

Chapter 3 describes the main experimental procedures and characterization techniques used in this study.

Chapter 4 reports the effect of extrinsic impurities on the electrical properties and radiation response of BiI_3 detectors. PVT and TMZ techniques are utilized to reduce the concentration of extrinsic impurities. The electrical properties and radiation response of BiI_3 detectors fabricated using commercial and ultra-pure BiI_3 powders are compared.

Chapter 5 presents the defect engineering strategies to further improve the electrical properties and radiation response of BiI_3 detectors. Defect models are theoretically established for BiI_3 system by donor doping. Defect engineering through

Sb doping into BiI_3 lattice is proposed in order to reduce formation and migration of iodine vacancy related with current obstacles for iodine compound semiconductor detectors. DFT calculations are used to determine most probable doping site of Sb in BiI_3 lattice and to investigate how Sb bonds with surrounding atoms. The electrical properties and radiation response of Sb doped BiI_3 and pure BiI_3 detectors are compared.

Chapter 6 covers fast-firing synthesis methods to induce CP in BT ceramics. Dielectric properties of fast-fired BT synthesized through SPS and MWS are discussed with comparison to those of PS sintered BT ceramics. Moreover, the effect of annealing on dielectric properties of MWS BT ceramics is present.

Chapter 7 identifies the dielectric polarization mechanisms in fast-fired BT ceramics exhibiting CP. Broadband dielectric spectroscopy (40 Hz ~ 4 MHz, 300 K ~ 20 K) is performed in order to reveal dielectric polarization mechanisms and also bulk conduction mechanisms in fast-fired BT ceramics exhibiting CP. In addition, the contributions of the each polarization mechanisms to the relative permittivity were estimated.

Finally in Chapter 8, a summary of the dissertation is presented and the future work in the relevant research areas is discussed.

1.4 Contributions to the Field

The main contributions of this dissertation to the development of BiI_3 single crystal as a room temperature gamma-ray detector and fast-fired BT as a high-K dielectrics.

Improved electrical properties, such as low leakage current and high resistivity, were achieved in ultra-pure BiI_3 detectors (total impurity level below 10 ppm) which were

fabricated by using PVT synthesized ultra-pure BiI_3 powder. This demonstrated that extrinsic impurities have significant influence on the functionality of the BiI_3 detector. This work was submitted to the *Journal of Instrumentation* with the title of “Growth, fabrication and testing of bismuth tri-iodide semiconductor radiation detectors”. The author was responsible for all the sample synthesis and preparations, data measurements for impurity analysis, and writing part of the manuscript.

A defect engineering strategy was developed to mitigate obstacles associated with BiI_3 detectors (i.e. high ionic conductivity due to high concentration of iodine vacancy). To accomplish this defect engineering in BiI_3 , Sb was determined as an optimal extrinsic dopant with a concentration of 0.5 at%. Low leakage current, high resistivity, and less polarization effect were achieved in defect engineered BiI_3 single crystal detectors. This work was published in the *Journal of Physical Chemistry C* with the title of “Enhanced electrical and radiation detecting properties of Sb-doped BiI_3 single crystal as a room temperature gamma-ray detectors”. The author was responsible for leading the manuscript, all the sample synthesis and preparations, and the data measurements and analysis except for computational works, leakage current, and alpha spectrum.

CP was induced in BT ceramics synthesized by MWS techniques for the first time. Dielectric properties of MWS BT ceramics were optimized through various annealing conditions. This work was published in the *Journal of American Ceramic Society* with the title of “Colossal permittivity in microwave-sintered barium titanate and effect of annealing on dielectric properties”. The author was responsible for leading the

manuscript, all the data measurements and analysis, and all the sample synthesis and preparation except for SPS BT ceramics.

The origin of CP in fast-fired BT ceramics was determined to be a result of a hopping polarization within semiconducting grains in combination with interfacial polarization at the insulating grain boundary. The relative contributions of each polarization to CP of BT ceramics sintered by SPS technique were calculated as ~57 % hopping polarization, ~28 % interfacial polarization, and ~15 % electrode effect. This work was published in the *Journal of Applied Physics* with the title of “Origin of colossal permittivity in BaTiO₃ via broadband dielectric spectroscopy”. The author was responsible for leading the manuscript, all the data measurements except for ICP-AES data, and all the data analysis except for ICP-AES results.

Analysis of the temperature dependent bulk dc conductivity reveals that the bulk conduction in fast-fired BT exhibiting CP is the result of variable-range-hopping (VRH) rather than nearest-neighboring-hopping (NNH). This work was accepted by the *Journal of Physical Chemistry C* with the title of “Variable range hopping conduction in BaTiO₃ ceramics exhibiting colossal permittivity”. The author was responsible for leading the manuscript, all the data measurements and analysis.

CHAPTER 2 BACKGROUND

This chapter summarizes the theoretical background required for understanding the research work covered in the following chapters.

2.1 Defect Chemistry

The logic and flow of this section is chiefly based on the books “Defects in Solids” by Richard J.D. Tilley and “Fundamentals of Ceramics” by M. W. Barsoum.^{52,53}

2.1.1 The Kröger – Vink Notation

Point defects in the crystal lattice indicate a deviation from the long range periodicity. The physical and chemical properties of materials are significantly affected by various point defects. Thus, a simple and consistent way to describe point defects in the material is necessary. In ceramic compounds, the Kröger – Vink notation is widely used to describe point defects.⁵⁴ The Kröger – Vink notation allows to apply chemical thermodynamics to defect equilibria by incorporating defect formation into chemical equations.

In the Kröger – Vink notation, vacancies are indicated by the symbol V, and the absent atom at a normally occupied site is represented as a subscript by the chemical symbol for the element. For example, V_O represents an oxygen atom vacancy in the lattice. The position of a defect substituting for atom in the crystal is specified by the subscript chemical symbol of the originally occupied atom at the site. The impurity is written in its chemical symbol, and hence, if Mg atom substitutes Ni site in NiO, the Kröger – Vink notation for this defect would be Mg_{Ni} . Interstitial positions are noted by the subscript “i”. In addition, one or more lattice defects can associate with one another to form defect clusters. In this case, parentheses enclosing the components are used to

indicate the defect cluster. For instance, $(V_M V_X)$ indicates a defect cluster of a metal and non-metal vacancies pair.

The Kröger – Vink notation can also define the effective charges (q_e) of the defects. The effective charge of a defect is the relative charge of the defect with respect to that of the originally occupied atom at the site in a perfect crystal. For atomic or ionic species, $q_e = z_d - z_s$, where z_d and z_s are the real charges on the defect species and the site occupied in a perfect crystal, respectively. The superscripts “’” and “•” are used to denote each unit of effective negative and positive charges, respectively. In an imperfect crystal, free electrons exist in the lattice, which is denoted by the symbol of “e’”. The concentration of free electrons is given the symbol “n”. Moreover, holes which are the counterparts to electrons are indicated by the symbol of “h•”, and the concentration of holes is given the symbol of “p”.

2.1.2 Intrinsic Point Defect Reactions in Stoichiometric Compounds: Schottky and Frenkel

Traditional chemical equations can be modified in order to describe defect reactions in the crystal. This allows to applying chemical thermodynamics into the defect system, and thus possible to establish defect chemistry in which the defects are regarded as the chemical species in traditional chemistry.

The defect reaction can be considered as the formation of defects in a perfect crystal with dopant. The rules for writing defect reaction are similar to those of traditional chemistry, however, defects have to be quantified with respect to crystallographic sites rather than molecules or moles. The following rules have to be followed:

- *Mass balance: mass cannot be created or destroyed. Vacancies have zero mass.*
- *Charge balance: charges cannot be created or destroyed.*
- *Site balance: the ratio between the numbers of regular cation and anion sites must remain constant and equal to the ratio of the parent lattice.*

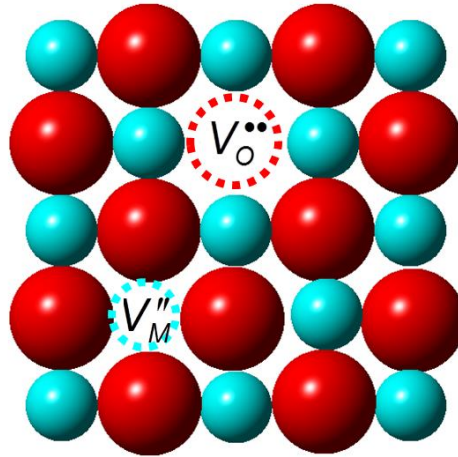
In stoichiometric compounds which the composition of the crystal is fixed, the point defects should be formed maintaining the composition of the material. There are two representative intrinsic point defects in stoichiometric compounds which called Schottky and Frenkel defects, respectively. Schottky defects are defines as the defects arising from balanced populations of cation and anion vacancies in any crystal. For example, in MO oxide, one Schottky defect is equal to one pair of cation vacancy (V_M'') and anion vacancy (V_O^{**}) in the crystal, and each vacancy does not necessarily to be near each other. In addition, if only Schottky defect exists in the crystal, the total number of anion vacancies should be consistent with that of cation vacancies in order to maintain the composition and charge neutrality. Thus, the total number of Schottky defect should be equal to one half of the total number of vacancies. The defect reaction for MO oxide can be written as,



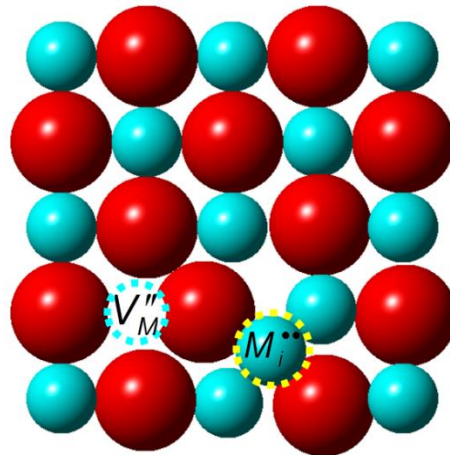
For Frenkel defect, one atom or ion is displaced from the original lattice and moves into an interstitial site in the crystal. The original lattice left as a vacancy site. Thus, a Frenkel defect consists of one interstitial ion and one vacancy in the lattice, which means the number of interstitials is equal to that of vacancies forming a Frenkel defect. The defect reaction for a cation Frenkel defect in MO oxide can be represented as,



Figure 2-1 depicts graphical images of Schottky and cation Frenkel defects in MO oxide.



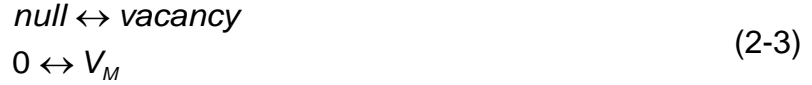
A



B

Figure 2-1. Representative defects in MO oxide A) Schottky and B) Frenkel defects.

The equilibrium of defect formation can also be treated as a chemical equilibrium. In the defect formation, the concentration of defects replaces the activity of species in chemical equilibrium. Therefore, in the case of vacancy formation,



and, at equilibrium, the change in Gibbs free energy (ΔG_v) can be given by,

$$\Delta G_v = -kT \ln K_v \quad (2-4)$$

K_v is the equilibrium constant for a single vacancy formation, and k is Boltzmann constant. Thus, K_v can be expressed as,

$$K_v = \frac{n_v}{N} = \exp\left(\frac{-\Delta G_v}{kT}\right) \quad (2-5)$$

n_v is a concentration of vacancy at equilibrium in N lattices. Thus, n_v can be written as,

$$n_v = N \exp\left(-\frac{\Delta G_v}{kT}\right) \quad (2-6)$$

If neglect entropy term, n_v can be expressed as follow.

$$n_v \approx N \exp\left(-\frac{\Delta H_v}{kT}\right) \quad (2-7)$$

where ΔH_v is the enthalpy change for vacancy formation..

Equilibrium of Schottky defect in a crystal can be considered in a same manner described above. For a crystal of composition MX , Schottky defect formation can be written as,



where V_M and V_X represent vacancies on cation and anion sites, respectively. The law of mass action can yield the equilibrium constant for the formation of Schottky defects, K_S ,

$$K_S = \left(\frac{n_{cv}}{N}\right)\left(\frac{n_{av}}{N}\right) = \exp\left(\frac{-\Delta G_S}{RT}\right) \quad (2-10)$$

where n_{cv} and n_{av} denote the number of cation vacancies and the number of anion vacancies, and N is the number of cation sites, which is equal to the number of anion sites in the crystal. ΔG_S is the molar Gibbs free energy of the formation of the Schottky defect, and R represents the gas constant. Since n_{cv} is equal to n_{av} for the Schottky defect, the number of Schottky defects (n_s) can be described as,

$$n_{cv} = n_{av} = n_s = N \exp\left(\frac{-\Delta G_S}{2RT}\right) \quad (2-11)$$

, n_s indicates the number of Schottky defects per unit volume in the crystal. By neglecting entropy terms,

$$n_s \approx N \exp\left(\frac{-\Delta H_s}{2RT}\right) \quad (2-12)$$

where ΔH_s is the enthalpy required to form 1 mol of Schottky defects in the crystal.

Table 2-1 summarizes the enthalpy of Schottky defects for some of Alkali halide compounds (MX) which have sodium chloride (NaCl) structure.

Table 2-1. Experimentally determined Schottky defect formation enthalpy in Alkali halide compounds.

Compound	ΔH_s (kJ/mol)	Δh_s (eV/atom)
LiF	225.2	2.33
LiCl	204.1	2.12
LiBr	173.4	1.80
LiI	102.4	1.06
NaF	233.1	2.42
NaCl	225.8	2.34
NaBr	203.0	2.10
NaI	140.9	1.46
KF	262.0	2.72
KCl	244.5	2.53
KBr	224.6	2.33
KI	153.0	1.59

For Frenkel defects on the cation sublattice, the chemical equilibrium can be expressed by,



where V_M and M_i are a vacancy on a cation site and a cation interstitial, respectively. Hence, the equilibrium constant for the formation of Frenkel defects, K_{cF} , can be written as,

$$K_{cF} = \left(\frac{n_{cv}}{N} \right) \left(\frac{n_{ci}}{N_i} \right) = \exp\left(\frac{-\Delta G_{cF}}{RT} \right) \quad (2-15)$$

here, n_{cv} represents the number of cation vacancies and n_{ci} is the number of cation interstitials. In addition, N and N_i indicate the number of cation and interstitial sites, respectively. ΔG_{cF} is the molar Gibbs free energy for the formation of cation Frenkel defects. In the case of Frenkel defects, n_{cv} is equal to both of n_{ci} and n_F (the number of Frenkel defects), and thus following equation can be established for the Frenkel defects in the crystal.

$$n_{cv} = n_{ci} = n_{cF} = \sqrt{NN_i} \exp\left(\frac{-\Delta G_{cF}}{2RT} \right) \quad (2-16)$$

$$n_{cF} \approx \sqrt{NN_i} \exp\left(\frac{-\Delta H_{cF}}{2RT} \right) \quad (2-17)$$

where n_{cF} and ΔH_{cF} are the number of cation Frenkel defects per unit volume and the enthalpy of Frenkel defect formation in the crystal. The same approach can be applied for deriving defect equilibria equations for Frenkel defects on the anion sublattice, and the following equations are obtained.

$$n_{av} = n_{ai} = n_{aF} = \sqrt{NN_i} \exp\left(\frac{-\Delta G_{aF}}{2RT}\right) \quad (2-18)$$

$$n_{aF} \approx \sqrt{NN_i} \exp\left(\frac{-\Delta H_{aF}}{2RT}\right) \quad (2-19)$$

Experimentally determined Frenkel defects formation energies are given in Table 2-2 for some compounds.

Table 2-2. Examples of Frenkel defect formation enthalpy.

Compound	ΔH_F (kJ/mol)	Δh_F (eV/atom)
AgCl	139.7	1.45
AgBr	109.0	1.13
β - AgI	57.8	0.60
CaF ₂	261.4	2.71
SrF ₂	167.4	1.74
BaF ₂	184.3	1.91

2.1.3 Diffusion and Electrical Conductivity

Diffusivity and electrical conductivity of ceramics are significantly influenced by the presence of point defects. Point defects increase the number of available jumping sites for the diffusion in the material. In addition, since point defects have effective charges, it can be migrated under an electric potential gradient which affects electrical conductivity of the material. Theoretical relationships between point defects and diffusion or electrical conductivity will be given in the following discussions.

The diffusivity (D) of an atom or ion is a measure of the ease and frequency with which that atom or ion jumps around in a crystal lattice. It is widely accepted that D is thermally activated and can be written as,

$$D = D_o \exp\left(-\frac{Q}{kT}\right) \quad (2-20)$$

where Q is the temperature independent activation energy and D_0 is the temperature dependent constant for the diffusion. In addition to temperature, it also has been understood that diffusivity of the material is strongly dependent on the stoichiometry and purity level of the material.

The following equation (2-21) can be used to fundamentally relate the diffusion coefficient D to the atomistic diffusion process in a solid.

$$D = \alpha \Omega \lambda^2 \quad (2-21)$$

where Ω is the number of successful jumps per second, λ is the jumping distance, and α is a geometric parameter which depends on the crystal structure. For cubic lattices, $\alpha = 1/\zeta$, where ζ is the coordination of the vacancy. Furthermore, Ω is the product of the probabilities of an atom's to have the sufficient energy to jump (ν) and to have empty adjacent site for diffusion (θ).

$$\Omega = \nu \theta \quad (2-22)$$

According to the Boltzman distribution law, the probability (P) of a particle to have an energy (ΔH_m^*) or greater is defined by,

$$P = (const.) \exp\left(-\frac{\Delta H_m^*}{kT}\right) \quad (2-23)$$

Thus, if an adjacent site is vacant, ν can be expressed as,

$$\nu = \nu_0 \exp\left(-\frac{\Delta H_m^*}{kT}\right) \quad (2-24)$$

where ν_0 is the vibrations of the atoms. Moreover, θ is significantly lower than 1 since most of the sites are surrounded by other atoms, and θ can be assumed to equal with

the concentration of vacancies (Λ) in a crystal. Thus, considering the vibrational entropy, the diffusion coefficient can be driven by,

$$D_{ion} = \alpha \lambda^2 \Lambda \zeta v_o \exp\left(-\frac{\Delta G_m^*}{kT}\right) \quad (2-25)$$

where ΔG_m^* is given by,

$$\Delta G_m^* = \Delta H_m^* - T\Delta S_m^* \quad (2-26)$$

The vibration entropy of ΔS_m^* is associated with the frequencies of the ions in ground (v) and activated (v') states by,

$$\Delta S_m^* \approx kT \ln(v'/v) \quad (2-27)$$

Putting all together, a final expression for the diffusion coefficient can be obtained as,

$$D_{ion} = v_o \lambda^2 \alpha \zeta \Lambda \exp\left(\frac{\Delta S_m^*}{k}\right) \exp\left(-\frac{\Delta H_m^*}{kT}\right) = D_o \exp\left(-\frac{Q}{kT}\right) \quad (2-28)$$

In the presence of electric field, an ion is diffusing under an electrical potential gradient of $\frac{d\varphi}{dx}$, where φ is the electric potential in volts. Ions diffuse from higher to lower electric potentials, and the diffusion process is no longer random however is biased in the direction of decreasing free energy. In such situations, the driving force for the diffusion can be expressed by,

$$f_i = -z_i e \frac{d\varphi}{dx} \quad (2-29)$$

where z_i is the net charge on the moving ion. The ionic flux, J_{ion} (atoms/m² · s), is related with the current density, I_i (C/m² · s), by

$$I_i = z_i e J_{ion} \quad (2-30)$$

Substituting equation (2-29) into (2-30),

$$I_i = -\frac{z_i e c_{ion} D_{ion}}{kT} \left[z_i e \frac{d\phi}{dx} \right] \quad (2-31)$$

by comparing equation (2-31) with Ohm's law, the ionic conductivity (σ_{ion}) can be given as,

$$\sigma_{ion} = \frac{z_i^2 e^2 c_{ion} D_{ion}}{kT} \quad (2-32)$$

This equation which is known as the Nernst-Einstein equation relates the diffusion coefficient to the ionic conductivity.

Furthermore, for the mobile ions drifting with an average velocity (v_d), the current density can be given by,

$$I_i = |z_i| e v_{d,i} c_{m,i} \quad (2-33)$$

where c_m is the concentration of the mobile ions (number of carriers per cubic meter). In addition, the electric mobility of the carrier, μ_d ($m^2 / V \cdot s$), is defined as the average drift velocity per electric field.

$$\mu_d = -\frac{v_{d,i}}{d\phi/dx} \quad (2-34)$$

By substituting equation (2-33) and (2-34) into Ohm's law, the important relationship can be driven,

$$\sigma_{ion} = c_{m,i} e |z_i| \mu_{d,i} \quad (2-35)$$

If there are more than one type of mobile charged species, the total ionic conductivity should be,

$$\sigma_{tot} = \sum_i c_{m,i} e |z_i| \mu_{d,i} \quad (2-36)$$

Moreover, by comparing equation (2-35) with (2-32), one can expect that the electric mobility of the charged mobile ion can be written as,

$$\mu_{d,i} = \frac{|z_i| e_i D_{ion}}{kT} \quad (2-37)$$

This equation implies that the mobility of a charged species is directly related to the diffusivity of the species.

Several experimental techniques and computational tools can be utilized to extract the key thermodynamic and kinetic parameters related with defect formation and migration. Some of the most useful techniques for defect characterizations are summarized in Table 2-3.²⁵

Table 2-3. Defect characterization tools.

Technique	Thermodynamic parameters related with defects
Impedance spectroscopy ⁵⁵⁻⁵⁷	Diffusivity measurements via conductivity relaxation Defect concentrations by measuring chemical capacitance Separation of bulk and interfacial contributions to the electrical properties by measuring frequency-dependent complex impedance
Thermogravimetric analysis (TGA) / coulometric titration ^{56,58}	Defect concentration by measuring mass change or electrochemically induced stoichiometry changes
Secondary ion mass spectroscopy ⁵⁹	Chemical composition profiles and tracer diffusion measurements
X-ray and neutron diffraction ^{60,61}	Defect ordering and concentration by investigating atomic occupancy factors and lattice strain
Optical absorption and emission ^{62,63}	Electronic structure and defect energy states

2.2 Dielectric Polarizations in Solids

This section is chiefly based on books “Dielectric Phenomena in Solids” by K. C. Kao and “Electroceramics” by A. J. Moulson.^{64,65}

2.2.1 Polarization Mechanisms

Polarization in dielectrics is defined as short-range movement or a limited rearrangement of charge carriers under an applied electric field (E). The polarization (P) is given by,

$$P = N\mu = Nq\delta \quad (2-38)$$

where N , q , and δ represent the number of the dipole moments per unit volume, the charge, and the distance between the charges, respectively. The dielectric permittivity (ϵ_r') of the material is related with P by,

$$\epsilon_r' - 1 = \frac{P}{\epsilon_o E} = \frac{Nq\delta}{\epsilon_o E} \quad (2-39)$$

where ϵ_o is the vacuum permittivity (8.854×10^{-12} F/m).

Furthermore, the polarizability (α) of an atom or ion is described by,

$$\alpha = \frac{P}{NE_{loc}} \quad (2-40)$$

where E_{loc} is the local electric field, and is determined for a cubic lattice as,

$$E_{loc} = \frac{E}{3} (\epsilon_r' + 2) \quad (2-41)$$

by substituting equation (2-40) and (2-41) into (2-39),

$$\epsilon_r' - 1 = \frac{N\alpha / \epsilon_o}{1 - N\alpha / 3\epsilon_o} \quad (2-42)$$

which can be rearranged as,

$$\frac{\epsilon_r' - 1}{\epsilon_r' + 2} = \frac{\alpha N}{3\epsilon_o} \quad (2-43)$$

This equation, which is known as the Clausius-Mossotti equation, links the microscopic property (α) of the material with its macroscopic property (ϵ_r').

It is important to note that four main polarization mechanisms exist in dielectric materials: space charge polarization, dipolar polarization, ionic polarization, and electronic (atomic) polarization. Electronic (atomic) polarization indicates the displacement of the electron cloud relative to the nucleus under the applied electric field. This polarization can respond up to frequencies of $\sim 10^{15}$ Hz. Ionic polarization is the displacements of cation and anion toward the negative and positive bias, respectively. The displacements of both positive and negative ions result in ionic dipoles, which can respond to an applied electric field up to $\sim 10^{13}$ Hz. Dipolar polarization is attributed to the alignment of randomly oriented dipoles under an external field, and it can respond at relatively lower frequencies (up to $\sim 10^8$ Hz). Lastly, space charge polarization is due to an inhomogeneous spatial distribution of charge centers over the microstructure. Space charge polarization can respond up to only $\sim 10^6$ Hz. Figure 2-2 depicts schematics of four main polarization mechanisms, and Figure 2-3 represents the contributions of each polarization mechanism to the total relative permittivity as a function of frequency.

Since charged point defects can be significantly attributed to space charge polarization at interfaces (grain boundaries) and in grains through interfacial polarization and hopping polarization, respectively, more details about space charge polarization is given in the following section.

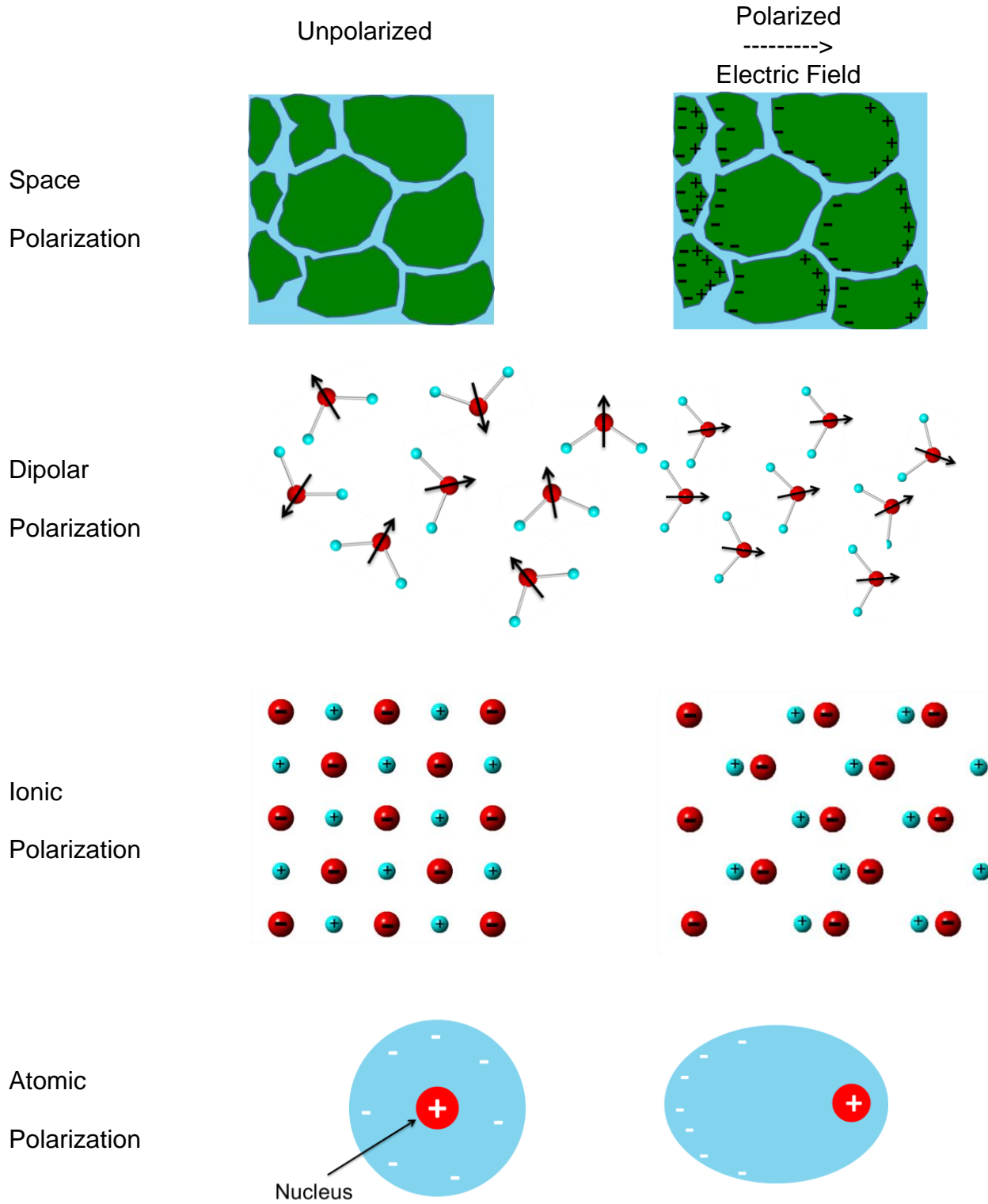


Figure 2-2. Schematics of four main polarization mechanisms.

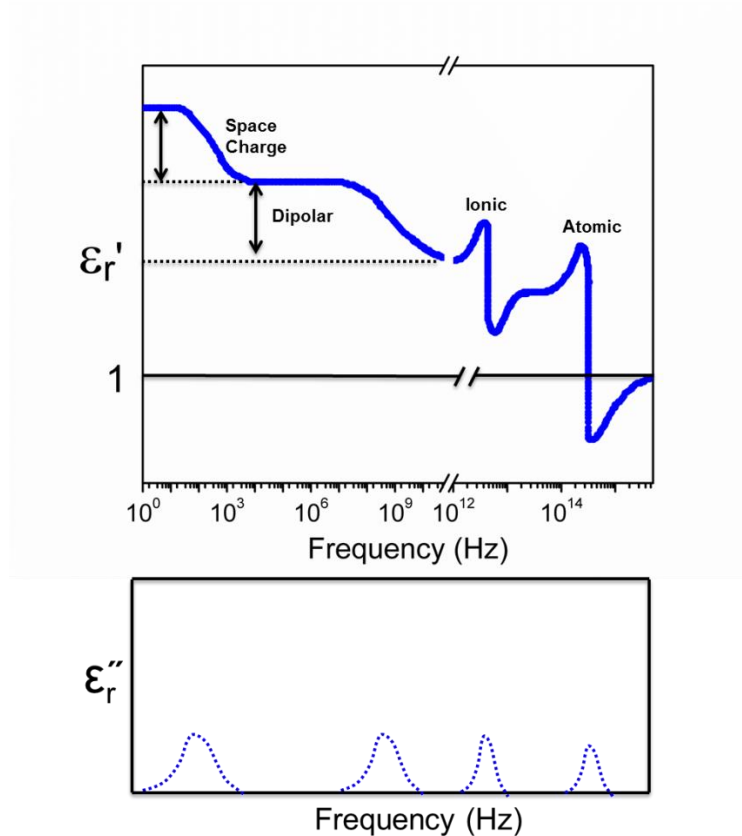


Figure 2-3. Contributions of each polarization mechanism to the total relative permittivity as a function of frequency.

2.2.2 Space Charge Polarization

Dielectric polarization can be associated with localized electronic defects, such as electrons and holes, and ionic defects, such as vacancies and impurities. These charge carriers can move under the applied electric field, and build inhomogeneous spatial charge distribution through the material, which is generally referred to as space charge. Moreover, the opposite charges may form electrical dipoles, which can be polarized under a.c. field, and thus contribute to the dielectric properties of the material. This polarization phenomenon is defined as space charge polarization, which can be considered following two possible ways.

2.2.2.1 Hopping polarization

Localized charge carriers in a dielectric material can hop together by jumping from one site to the neighboring site, which results in forming hopping dipoles. Under applied electric field, these hopping dipoles can affect dielectric response of the material in the same manner with dipolar polarization, and is commonly referred to as hopping polarization. In hopping polarization, charge carriers should overcome a potential barrier between neighboring sites to hop, and thus the hopping process is normally temperature activated process. Therefore, in thermal equilibrium, the probability (p_o) for a charged particle to form a hopping dipole can be written as,

$$p_{o(A \rightarrow B)} = C \exp(-E_A / kT) \quad (2-44)$$

which is the case for the negatively charged particle that hop from site A to B, leaving behind a positive charge at site A and creating a negative charge at site B. Here, C and E_A are a constant and the activation energy for hopping process, respectively (Figure 2-4).

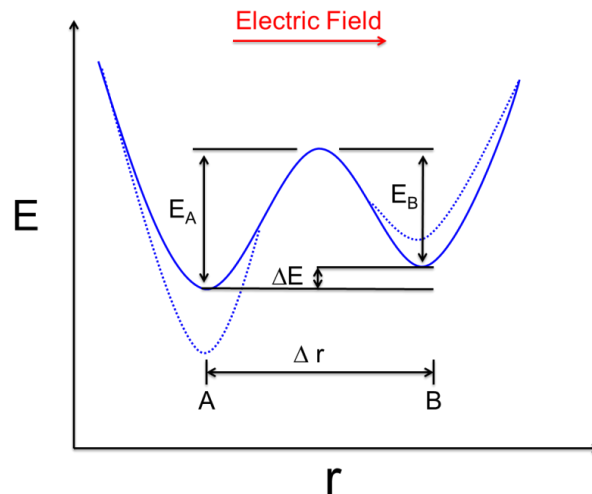


Figure 2-4. Hopping polarization due to the hopping of the charged particle over the barrier from one site to the other.

2.2.2.2 Interfacial polarization

The interfacial polarization is due to the positive and negative space charges at the interfaces between different materials or microstructures such as grain boundaries (Figure 2-2). In this case, equivalent circuit can be established with two components in series, and each component is composed of two parallel elements, i.e., a capacitance and a conductance (Figure 2-5). This model is referred to as internal barrier layer capacitance (IBLC) model, and widely used to describe dielectric response of the material being attributed to interfacial polarization.

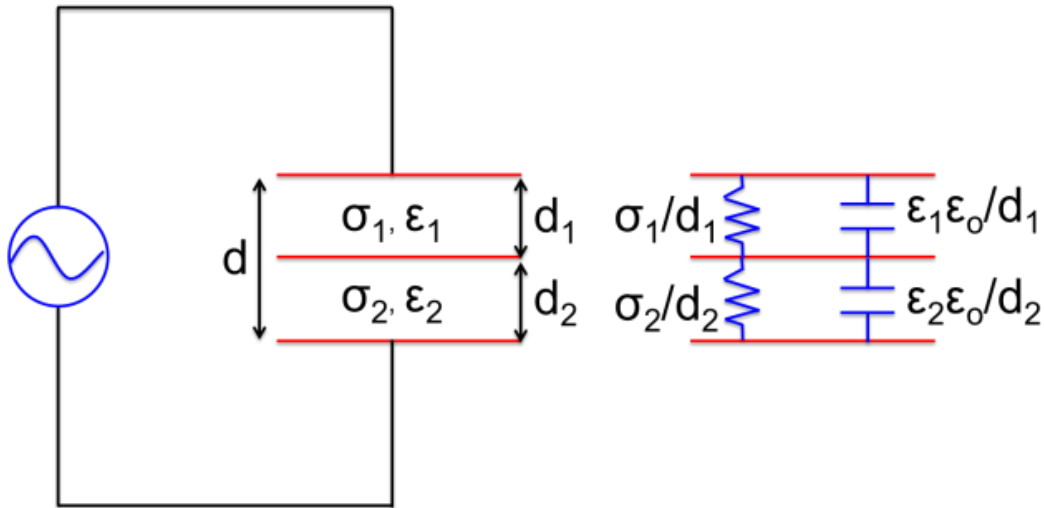


Figure 2-5. A dielectric material comprising of two different components.

In IBLC model, one component is highly conductive while the other component is highly capacitive, and conductive phases are separated by very thin layers of capacitive phases. Thus, space charges in conductive component can be attributed to dielectric polarization while not conducting through the material. Then, the effective relative permittivity (ϵ_{eff}) according to IBLC model can be represented by,

$$\epsilon_{eff} = \frac{\epsilon_1 d_1}{d_2} \quad (2-45)$$

where, ϵ_1 and d_1 are the relative permittivity and thickness of conductive component, and d_2 represents the thickness of capacitive thin layer.

2.2.3 The Universal Dielectric Response

The frequency dependence of P can be given by,

$$P(\omega) = \epsilon_o \epsilon_r(\omega) E(\omega) \quad (2-46)$$

where $\omega = 2\pi f$, f is the circular frequency in Hz, and ϵ_r is the complex permittivity, which can be written as,

$$\epsilon_r(\omega) = \epsilon'_r - i\epsilon''_r(\omega) \quad (2-47)$$

here $i = \sqrt{-1}$. The components of polarization in phase and out of phase with the external field are respectively associated with the real part (ϵ'_r) and the imaginary part (ϵ''_r) of ϵ_r . The component of imaginary part is known as the dielectric loss, and is directly related to the energy lost per radian given by,

$$E_{lost} = \epsilon_o \epsilon''_r(\omega) E_o^2 / 2 \quad (2-48)$$

where E_o is a peak amplitude of applied electric field. Since the power lost due to phase difference is defined by $\sigma_{a.c.}(\omega) E_o^2 / 2$, the a.c. conductivity of dielectrics can be driven by,

$$\sigma(\omega) = \omega \epsilon_o \epsilon''_r(\omega) \quad (2-49)$$

This equation reveals the relationship between the dielectric loss and the a.c. conductivity of the material.

The responses of electronic and ionic polarizations are so rapid that they can contribute to a purely real value of the permittivity (ϵ_∞) below GHz frequencies. However, permanent dipoles such as dipolar ionic defects and hopping charge carriers

have much slower response such that the total permittivity of a medium can be written as,

$$\epsilon_r(\omega) = \epsilon_\infty + \epsilon_0 \sum_{\alpha} \epsilon_{\alpha}(\omega) \quad (2-50)$$

where index α indicates the various polarization mechanisms.

Debye's model describes the classical case of dipolar dielectric response by thermal excitation between two preferred sites separated by a potential barrier. The Debye susceptibility can be expressed by,

$$\chi(\omega) \propto \frac{1}{1 + i\omega\tau} = \frac{1}{1 + \omega^2\tau^2} - i \frac{\omega\tau}{1 + \omega^2\tau^2} \quad (2-51)$$

where τ is the relaxation time which is equal to the inverse of the relaxation frequency (ω_p). ω_p is also identical to the loss peak frequency, and is normally thermally activated,

$$\omega_p = 1/\tau = \nu_o \exp(-E_A / kT) \quad (2-52)$$

where ν_o and E_A are the jump frequency and the activation energy, respectively. It is important to note that in the Debye model, the loss peak given by the imaginary part in equation (2-51) is symmetric with a width of 1.144 decades at the half max height on a $\log \omega$ scale. However, it is often observed that the dielectric loss in real materials strongly deviates from the Debye response. Figure 2-6 shows some examples of dielectric behaviors departed from the Debye theory. For the comparison purpose, the typical Debye response is also presented.

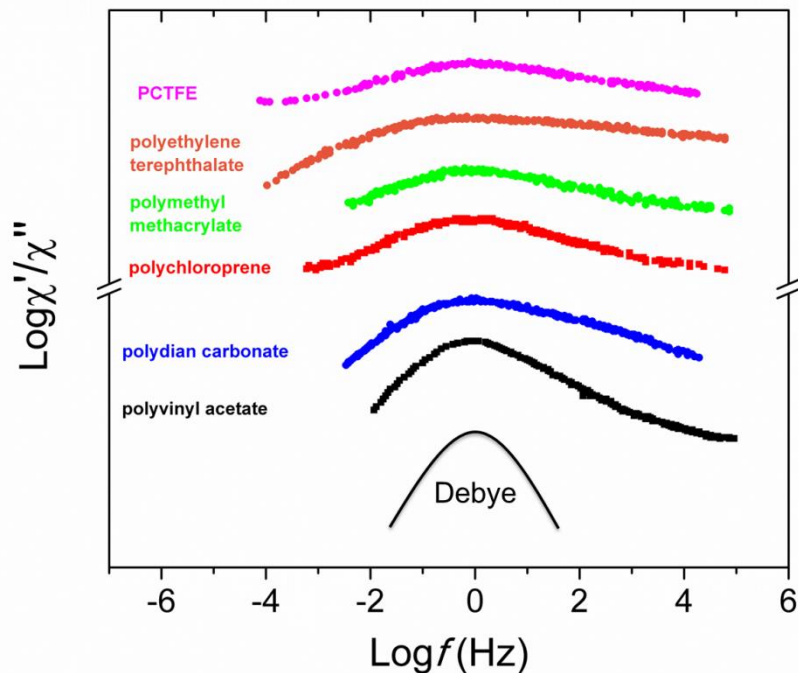


Figure 2-6. Examples of dielectric behaviors departed from the Debye theory.

A. K. Jonscher firstly pointed out that the asymmetric dielectric loss behavior of the various materials can be characterized by the relation,

$$\chi''(\omega) \propto \omega^{s-1} \text{ with } 0 < s < 1 \quad (2-53)$$

which is referred to as Jonscher's UDR model. According to the UDR model, the dielectric response of solids can be represented by the diagrams shown in Figure 2-7. The dielectric response dominated by the dipoles may be represented as Figure 2-7 (A), while the diagram of Figure 2-7 (B) represents when the mobile carriers dominates low-frequency response. However, for both cases, the UDR law (equation (2-53)) obeys the responses at the extended range of frequencies. Furthermore, the Kramers-Kronig transformation of $\chi''(\omega)$ gives rise to the real part of susceptibility, $\chi'(\omega)$, which has

the same functional form but with a constant factor of $\cot(s\pi/2)$. Thus, the ratio of the real and the imaginary parts of susceptibility can be represented as,

$$\chi''(\omega) / \chi'(\omega) = \cot(s\pi/2) = \text{const.} \quad (2-54)$$

, which is completely contrast with the Debye theory where the ratio is equal to $\omega\tau$.

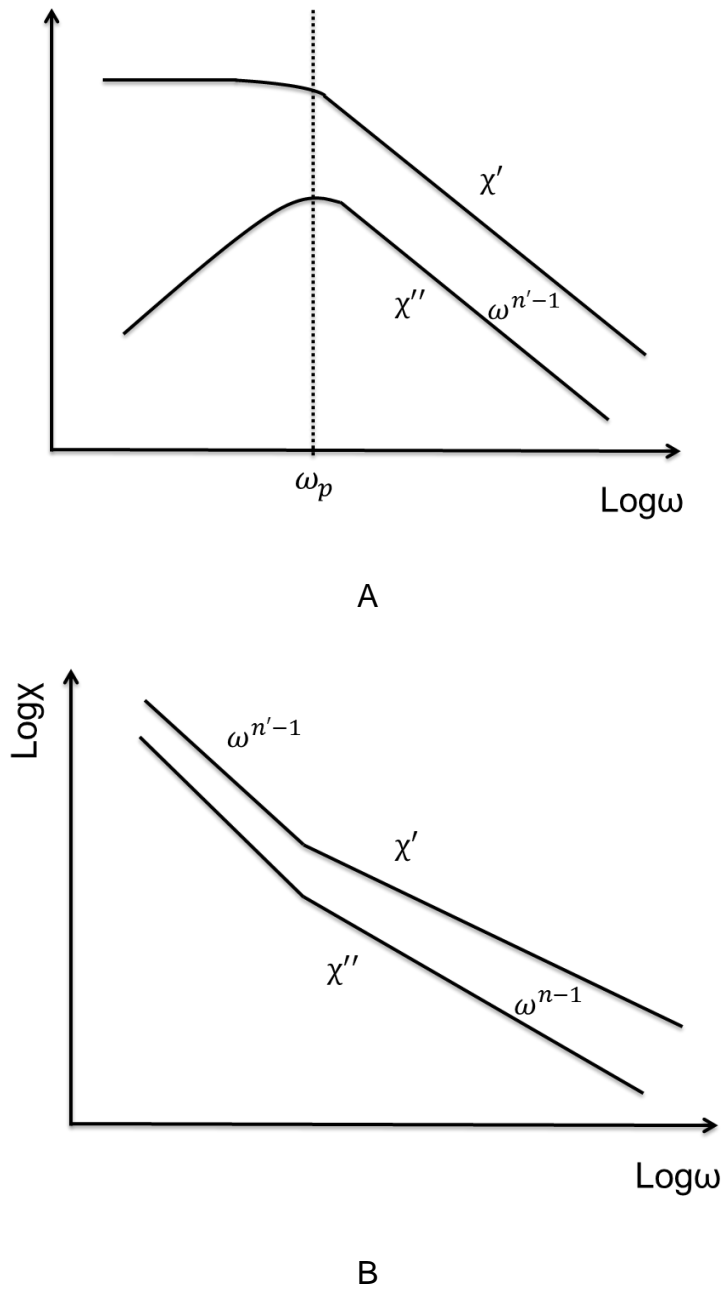


Figure 2-7. Schematic representations of the two types of dielectric response, A) response dominated by dipoles and B) response dominated by mobile

carriers at low frequencies.

By substituting equation (2-53) into (2-49), it is clear that the frequency dependence of the electrical conductivity of the materials follows the expression,

$$\sigma(\omega) = \sigma_{d.c.} + \sigma_o \omega^s \quad (2-55)$$

where σ_o and s are constants, and $\sigma_{d.c.}$ is the direct current conductivity. It should be noted that the exponent s represents the degree of localization related charge dipoles, and s value closer to 1 indicates that the charge carriers are more highly localized. In addition, the response with s values close to unity is associated with the intrinsic lattice response, whereas the response with the s values between $0.5 < s < 0.9$ are strongly related with the extrinsic carrier such as hopping electrons, induced defects, and impurities. Table 2-4 shows some examples of the numerical s values for different materials.

Table 2-4. Examples for numerical values of the exponent "s" for different materials.

Material	Temperature (K)	Exponent s
Si	3 ~ 12	0.79 ~ 0.74
β -Al ₂ O ₃	77 ~ 87	0.75 ~ 0.70
Sb _x As _{2-x} S ₃	293	1.0
As ₂ Se ₃	300	1.0
Se	300	0.95
As ₂ S ₃	300	0.92
As ₂ Se ₃	300	0.92
P2O5-FeO-CaO glass	300	0.85 ~ 0.89
SiO _x	211 ~ 297	0.6 ~ 0.7

2.3 Crystal Structures of BiI₃ and BaTiO₃

2.3.1 BiI₃

Effective defect engineering relies on the understanding of the crystal structure of the compound. Therefore, it is important to recall that the crystal structure of BiI₃ is a

rhombohedral structure ($C_{3i}^2(R\bar{3})$, space group No. 148) with the lattice parameters of $a = 7.516 \text{ \AA}$ and $c = 20.718 \text{ \AA}$, respectively. In the structure, Bi ions reside on the 6c Wyckoff positions with coordinates (0, 0, 0.1667) and I ions occupy the 18f positions with coordinates (0.3415, 0.3395, 0.0805).^{66,67} BiI_3 is comprised of layers of corner sharing BiI_6 octahedra stacked in the [001] with weak van der Waals forces between the layers (Figure 2-8 (A)). While I-Bi-I layers are bonded by weak van der Waals forces, bismuth and iodine are bonded by strong ionic bonds. Thus, this anisotropic crystallography leads to (001) cleavage planes in BiI_3 crystals and the preferred crystal growth direction along (001) planes. In addition, BiI_3 shows various anisotropic physical properties, such as optical, thermal and electrical properties, due to crystallographic anisotropy.⁶⁸⁻⁷⁰ Three close-packed layers stack in the sequence of I-Bi-I in each I-Bi-I layer. A polyhedral schematic for one I-Bi-I layer with empty octahedral sites is presented in Figure 2-8 (B). The red (lighter on the top and darker below the bismuth layer) and blue atoms represent iodine anions and bismuth cations, respectively. Bismuth ions can occupy three different sites within the iodine layers. It can be seen in Figure 2-8 (A) that two-thirds of the bismuth sites (A and B) are occupied by bismuth ions and one third of the C sites remain empty octahedral sites, which follow the sequence ABCABCABC... In the crystal structure of BiI_3 , it is hard to expect perfect stacking of the layers, however stacking faults usually exist in BiI_3 crystals leading to unique electrical properties such as stacking fault excitons.⁷¹ Table 2-5 tabulates crystal structure information for BiI_3 .

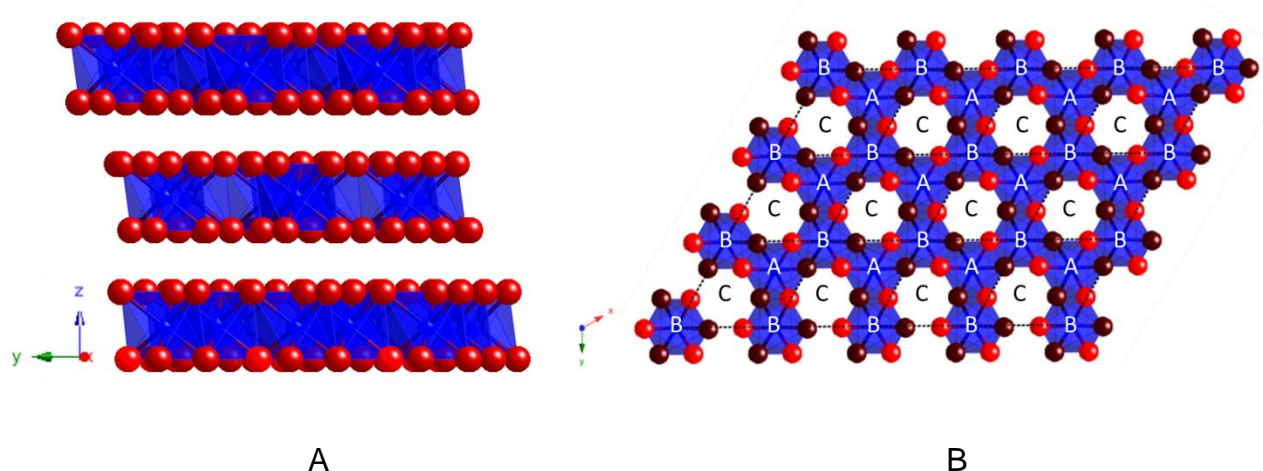


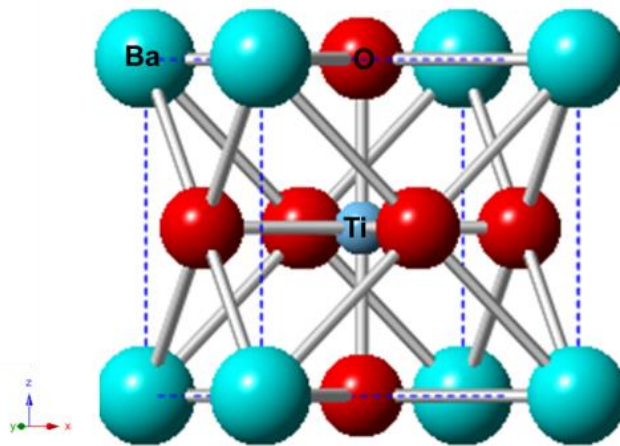
Figure 2-8. Polyhedral schematic for A) corner sharing octahedra in BiI_3 and B) empty octahedral sites in one I-Bi-I layer.

Table 2-5. Crystal structure information for BiI_3 .

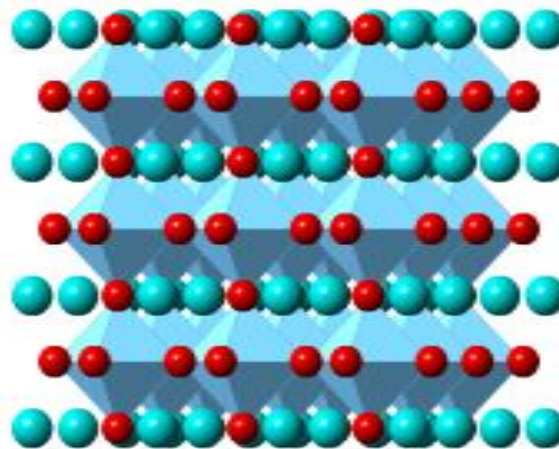
Space Group: $R\bar{3} (C_{3i}^2)$			
Atom	Coordination	Wyckoff position	Site symmetry
Bi	(0, 0, 0.1667)	6c	3-
I	(0.3415, 0.3395, 0.0805)	18f	1
Lattice parameters (\AA)			
a = 7.516		c = 20.718	

2.3.2 BaTiO_3

At ambient temperature, BT crystallizes in a tetragonal structure of which is identical with the mineral perovskite (CaTiO_3), and thus it is referred to as a “perovskite structure”. In a ABO_3 perovskite structure, it can be visualized that A-ions, which are cubic close-packed, coordinate with surrounding twelve O-ions, and B-ions reside in the octahedral interstitial sites (Figure 2-9).



A



B

Figure 2-9. Crystal structure of BT. A) Unit cell of tetragonal BT. B) Ti polyhedral schematic.

It can be easily seen that for the perovskite structure, the ionic radii of each ions should follow,

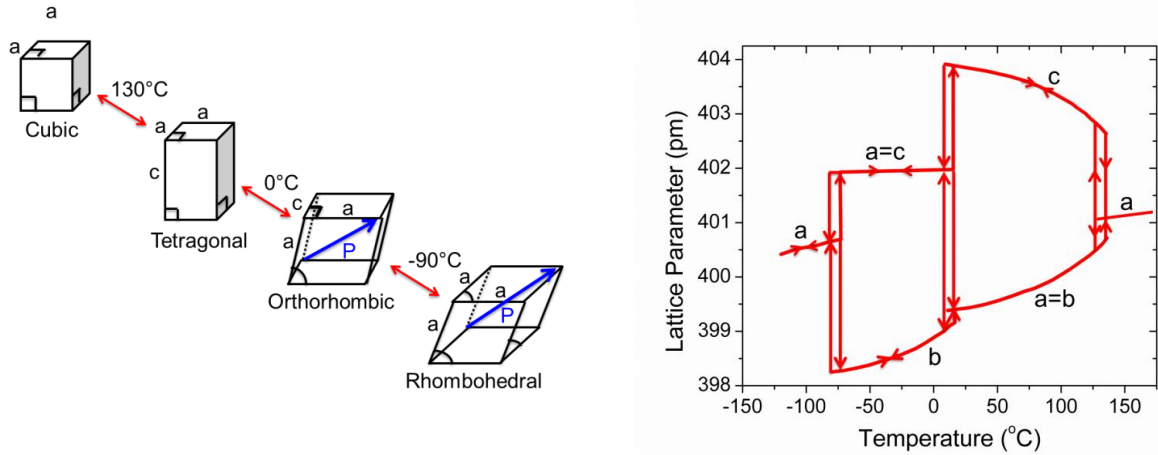
$$R_A + R_O = 2(R_B + R_O) \quad (2-56)$$

However, this equation does not hold exactly true for the most perovskite compounds due to small variations in the ionic radii of A and B ions. Therefore, one should invoke a tolerance factor “ t ” for the equation (2-56),⁶⁵ which can be written as,

$$R_A + R_O = 2t(R_B + R_O) \quad (2-57)$$

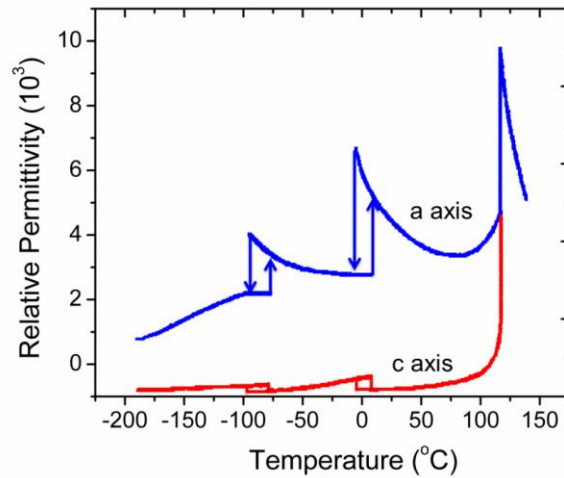
The value of “ t ” is typically in the range of between 0.95 and 1.06. Furthermore, it should be mentioned that when “ t ” is not equal to 1, small lattice distortions, which is also referred to as “octahedral tilting”, takes place in order to minimize lattice energy, and this distortion gives rise to an excellent dielectric properties into perovskite compounds.

The unit cell of BT is centrosymmetric above Currie temperature (T_c , 120°C), however below the Currie temperature, the structure is slightly distorted along c axis leading to non-centrosymmetric tetragonal structure with a dipole moment. In addition, BT exhibits two more distinguishable temperature-dependent phase transitions: (i) tetragonal to orthorhombic near 0°C and (ii) orthorhombic to rhombohedral near -90°.⁶⁵ Each crystal structure, tetragonal, orthorhombic, and rhombohedral, can be thought as elongated ABO_3 cubic structure along [001], [011], and [111], respectively. Net charge displacement between cations with respect to the oxygen anion octahedron exists in the BT crystal structures except centrosymmetric cubic crystal structure. Figure 2-10 illustrates (a) the transformations with (b) the corresponding lattice parameters changes, and (c) the relative permittivity of BT as a function of temperature.



A

B



C

Figure 2-10. Phase transformation and relative permittivity change of BT. A) The phase transformations. B) Lattice parameters change. C) Relative permittivity change.

The displacements of ions due to the cubic-tetragonal transformation can demonstrate how the spontaneous polarization can be coupled within unit cells. X-ray studies have revealed that the ions in the tetragonal unit cell are slightly (about 3 to 10 pm) displaced against the four central oxygen ions, which is depicted in Figure 2-11. It is obvious that in this figure, Ti ion at the central position is displaced toward one of the

oxygen ion marked as A, which consequently leads Ti ion on the opposite side of A to be displaced distantly from that oxygen ion. Hence, all the Ti ions in the same column are displaced in the same direction, and thus Ti ions in the next column are coupled with the displaced Ti ions resulting in ferroelectricity in BT.

Table 2-5 summarizes crystal structure information for tetragonal BT.⁷² Tetragonal BT has space group of $P4mm (C_{4v}^1)$ with the lattice parameters of 3.9909 Å for a and 4.0352 Å for c . Each atoms, Ba (0, 0, 0), Ti (0.5, 0.5, 0.5224), O1 (0.5, 0.5, -0.0244), and O2 (0.5, 0, 0.4895), occupy Wyckoff positions of $1a$, $1b$, $1b$, and $2c$ in the crystal structure, respectively. Thermal displacement and site symmetries for each site are also listed in Table 2-6.

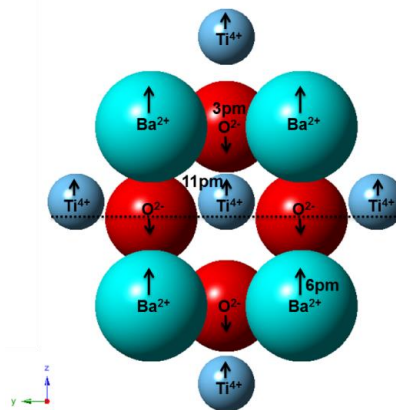


Figure 2-11. Approximate ion displacements in tetragonal BT.

Table 2-6. Crystal structure information for tetragonal BT.

Space Group: $P4mm (C_{4v}^1)$				
Atom	Coordination	Wyckoff position	Thermal displacement ($\text{\AA}^2 \times 1000$)	Site symmetry
Ba	(0, 0, 0)	1a	$U_{11}=U_{22}=2.90, U_{33}=3.50$	4mm
Ti	(0.5, 0.5, 0.5224)	1b	$U_{11}=U_{22}=0.02, U_{33}=5.40$	4mm
O1	(0.5, 0.5, -0.0244)	1b	$U_{11}=U_{22}=-0.30, U_{33}=4.80$	4mm
O2	(0.5, 0, 0.4895)	2c	$U_{11}=9.80, U_{22}=5.40, U_{33}=10.50$	2mm
		Lattice parameters (Å)		
		$a = 3.9909$	$c = 4.0352$	

CHAPTER 3
EXPERIMENTAL PROCEDURES AND PROCESSING

3.1 Sample Preparation

3.1.1 BiI₃ Single Crystals

3.1.1.1 PVT powder synthesis technique

Ultra-pure (total impurity level below 10 ppm) BiI₃ powder was synthesized by the PVT technique. Commercial bismuth polycrystalline lump (99.999%) and iodine lump (99.999%) from Alfa Aesar were used as the starting materials. The reaction between bismuth and iodine vapors was conducted in a quartz tube with diameter of 2" and length of 36". Bismuth and iodine lumps were weighed with a mole ratio of Bi : I₂ = 1 : 5 and loaded into a quartz boat separately. The extra iodine is added to compensate the loss of iodine due to high volatility of iodine. The boat with iodine lump was placed at one end of the quartz tube and kept at room temperature. The boat with bismuth lump was placed at center of the tube and heated up to 400°C. A Teflon sheet was placed at the other end of the quartz tube at room temperature to collect the synthesized BiI₃ powder. During the reaction, Ar gas (ultra high purity) was infused from the iodine side to facilitate the reaction between iodine and bismuth vapor, and the resulting BiI₃ powder was deposited on the Teflon sheet at lower temperature.

A gas flow meter (Digital High Performance Mass Flow, Smart-Track 100 Series from SIERRA) was used to consistently regulate the Ar flow. Optimal Ar flow rates were investigated between 80 and 160 standard cubic centimeter per minute (SCCM). Maximum yield was achieved at a 120 SCCM gas flow rate. Figure 3-1 shows the experimental set up for BiI₃ powder synthesis using the PVT technique.

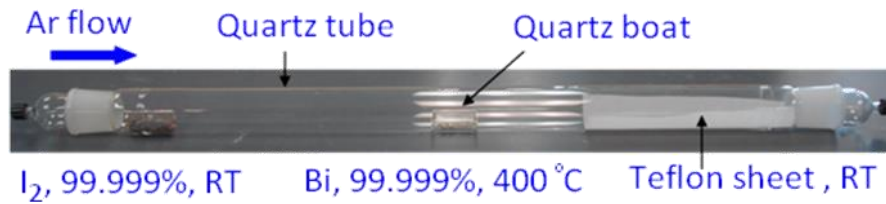


Figure 3-1. Experimental set up for BiI_3 powder synthesis using the PVT technique.

3.1.1.2 TMZ purification technique

The setup was built by Sasmit Gokhale under the guidance of Prof. Juan C. Nino. TMZ technique was employed for purifying BiI_3 starting powder. A band heater (MPP51101, TEMPCO Electric Heater corp.) was utilized to form a narrow molten zone in the ampoule. The maximum temperature of the heater was approximately 760°C . The heating zone was narrowed to 0.125 inch by using alumina insulation rings. A temperature controller (ATHENA Series 16C) combined with a thermocouple was used to control the temperature of band heater. The powder was sealed in a Pyrex glass ampoule of 0.75 inch inner diameter. The ampoule was mounted on a clamp, and the heater was moved about 90 zone refining passes at a rate of 4.4 cm / h. Figure 3-2 illustrates the experimental set up for the TMZ technique.



Figure 3-2. Experimental set up for the TMZ technique.

3.1.1.3 Single crystal growth of Te and Sb doped BiI₃

BiI₃ single crystals were grown by the modified vertical Bridgman method. Pyrex glass ampoule was selected as the growth chamber due to relatively low annealing (= 560°C) and softening point (= 815°C), however those temperatures are still higher than the maximum temperature (= 440°C) for the BiI₃ single crystal growth process. Customized Pyrex glass ampoules (inner diameter = 0.75 in, tip length \cong 5 cm, and tip angle \cong 70°) were purchased from Southern Scientific, Inc. The Pyrex ampoule was cleaned with glassware cleaning solution (Decon Contrad® 70) to remove residual organics. The ampoule was soaked with the solution for overnight under the fume hood, and then it was washed ten times with DI water ($\rho \cong 17.0 \text{ M}\Omega \cdot \text{cm}$) followed by baking at drying oven (120°C) for overnight. The amount of 20 g of BiI₃ powder with appropriate amount of TeI₄ and SbI₃ based on the doping concentration were weighed and loaded in the ampoule. TeI₄ and SbI₃ were initially added to the ampoule and loaded at the end of the tip. Before vacuuming the ampoule, a neck area with a diameter of approximately 0.25 inch was preformed at the middle of the ampoule using propane torch in order to facilitate sealing process. The ampoule was firstly vacuumed to a pressure of 4.0×10^{-2} mbar by using mechanical roughing pump, and then molecular turbo pump was turned on to finally evacuate the ampoule to 1.0×10^{-4} mbar. The vacuumed ampoule was then sealed by using a propane hand torch. The sealed ampoule was vertically mounted on a standing steel frame using galvanized steel wires, and placed in programmable 24 or 12 multi heating zone furnaces (EDG-13 and EDG-11, Mellen Company). The previously optimized growth condition, such as temperature

gradient of 10°C / cm and cooling rate of 0.5 mm / h, were utilized for all the single crystal growth process.^{28,29}

3.1.2 BaTiO₃ Ceramics

3.1.2.1 Microwave sintering

For MWS processing, commercially available nanocrystalline BT powder was purchased from Alfa Aesar (99+% metals basis, 50 to 70 nm average particle size). Before sintering, the starting powder was first ball-milled for 24 h in ethanol (70 ml) and dried in an oven at 120°C for 24 h.

To make green pellets, the dried powder was mixed with 1 wt % of PVA binder (Celvol 103), ground in a mortar and pestle for approximately 10 min, and then sieved through a 45 µm mesh. Green pellets (diameter 7 mm and thickness 1 mm) were formed initially in a uniaxial press of 170 MPa using a steel die and then isostatically pressed at a pressure of 200 MPa.

A Thermwave TW 1.3 (Microwave Systems, Inc., USA) apparatus was used for MWS process. Susceptors were used to heat the samples during MWS process. The following heating and cooling schedules were used during MWS; (i) first pellets were heated from room temperature to the sintering temperature of 1320°C at a rate of 65°C / min, (ii) then held at the sintering temperature for 30 min and (iii) finally cooled to room temperature in 2 h. Post-sintering annealing treatments were performed at different temperatures ranging between 900°C and 1200°C, and for 12 to 24 h in an air atmosphere at 10 standard cubic feet per hour (SCFH) flowing rate.

3.1.2.2 Spark plasma sintering

[This process was performed by Christophe Voisin, at Université Paul Sabatier in Toulouse France under the guidance of Dr. Sophie Guillemet-Fritsch] The starting

nanocrystalline BT powder was synthesized by an oxalate route. Briefly, $\text{BaCl}_2 \cdot 2\text{H}_2\text{O}$ and TiCl_3 were used as precursors to synthesize the starting powders. In order to control the powder stoichiometry, the precursors were weighted in appropriate proportions. The precursors were then dissolved in water and added to an ethanolic oxalic acid solution. The solution was stirred and aged approximately for 5 h, and it is centrifuged and then dried overnight at 80°C . After calcination at 850°C for 4 h in static air, the oxide powders were obtained.

SPS was performed on the synthesized powder by means of a Dr. Sinter 2080 from Sumimoto Coal Mining (SPS Syntx Inc., Dr. Sinter 2080). Approximately 0.9 g of powder without binder was placed in a 8 mm diameter graphite die and then sintered at different sintering temperatures (900°C , 1050°C , and 1150°C) with a dwell time of 3 minutes under 50 MPa of mechanical stress and electric current up to 350 A. A heating rate of $25^\circ\text{C} / \text{min}$ was used to reach the sintering temperature from 600°C . After 3 min dwelling, the sample was cooled down from the sintering temperature to room temperature at a rate of $100^\circ\text{C} / \text{min}$. A thin carbon layer was present at the surface of the as-sintered ceramic due to graphite contamination from the die. However, it was easily removed by polishing the surface of the ceramic. For annealing process, a furnace was preheated to 850°C and then the sample was placed into the furnace for 15 min dwell in air followed by air quenching.

3.1.2.3 Conventional pressureless sintering

Experimental procedures for preparing green pellets are same as MWS sintering (Chapter 3.1.2.1). The green pellets were then (i) first heated from room temperature to 400°C at a rate of $3^\circ\text{C} / \text{min}$ and (ii) held for 2 h with the aim to burn-out the added organic binder, and then (iii) heated from 400°C to the sintering temperature of 1350°C

at a rate of 3°C / min, (iv) held at the sintering temperature for 2 h, and (v) finally cooled to room temperature at a rate of 3°C / min. No annealing treatment was performed on conventionally sintered BT ceramics.

3.2 Characterization

3.2.1 X-ray Diffraction

Philips APD 3720 and Inel CPS X-ray diffractometers were used for structural characterization of BiI₃ single crystals and BT ceramics, respectively. The XRD data was measured using CuK α radiation, and the operation voltage and current were set as 40 kV and 20 mA for APD 3720, and 30 kV and 30 mA for Inel CPS, respectively. The CPS detector is one dimensional detector that measures data over a wide 2 θ range simultaneously, and therefore allows for rapid acquisition of diffraction data. For BT samples, all the XRD patterns were measured for a period of 5 min using the CPS detector, while APD 3720 was utilized for measuring XRD data of BiI₃ samples over the range of 2 θ from 10° to 60° with a step size of 0.02°.

3.2.2 Scanning Electron Microscopy

Scanning electron microscopy (SEM, JEOL 6335F FEG-SEM) was performed to reveal the particle size and morphology of the BT starting powders, and microstructure of the sintered BT ceramics. The operating voltage for the SEM was 15 kV with a probe current of 8 μ A. BT ceramics were fractured using a pestle and hammer, and subsequently sonicated in DI water for about 30 min. The sonicated samples were dried at drying oven (120°C) for approximately 1 h. The samples were mounted on SEM holder using copper (Cu) tape, and then it was coated by gold (Au) film with thickness of approximately 60 nm using sputter system (Cressington Scientific Inc., Cressington 108 Auto).

3.2.3 X-ray Photoelectron Spectroscopy

[This process was performed by Eric Lambers, at Major Analytical and Particle Analysis Instrumentation Centers (MAIC & PAIC) in University of Florida]. X-ray photoelectron spectroscopy (XPS) was performed on finely ground BT powders using a Perkin Elmer 5100 XPS system for investigation of Ti oxidation states. An Al $K\alpha$ monochromatic X-ray source (1486.6 eV) was used for collecting the XPS spectra. The take-off angle of 45° and the pass energy of 35.75 eV were used. Step size and integration time were set as 0.1 eV and 50 ms, respectively. The pressure inside the chamber was maintained below 10^{-9} torr during measurements.

3.2.4 Inductively Coupled Plasma – Atomic Emission Spectroscopy

The chemical compositions of BiI_3 starting powders and grown single crystals were determined by ICP-AES. ICP-AES equipment of Perkin-Elmer Optima 3200 RL was used for the measurements. The starting powder and crystals were dissolved in 10 % trace metal grade hydrochloric acid (HCl) solution with a concentration of 10 mg / ml. The elemental impurities were analyzed based on the reported impurity elements from the vendor. ICP-AES standard solutions (Quality Control standard 7 and 21, SPEX Certiprep. Inc.) were used for calibrating measurements. Standard solutions with the concentrations of 1 ppm, 0.1 ppm, and 0.01 ppm were used for the impurity analysis of synthesized BiI_3 powders, while 1 ppm, 10 ppm, and 100 ppm were exploited for the dopant concentration analysis. Error analysis was performed on the measured data by using standard deviation with the upper and lower 95 % confidence limits.

3.2.5 Dielectric Characterization

Sintered ceramics were coated with thin Au electrodes (thickness of ~30 nm) by sputtering (Cressington Scientific Inc., Cressington 108 Auto). The coated samples

were placed in a closed cycle cryonic workstation (CTI – Cryogenics, Model 22), and dielectric properties as a function of temperature (20 K ~ 300 K) were measured at the different frequencies (40 Hz - 100 kHz) through an Agilent 4284 LCR meter. Dielectric measurements from room to high temperature up to 473 K were performed in a temperature chamber and controller from Delta Design, Inc. Precision impedance analyzer (PIA, Agilent Ltd., Agilent 4294A) combined with cryonic workstation was used in order to perform broadband dielectric spectroscopy analysis (40 Hz – 1 MHz) in the temperature range from 20 K to 300 K. Error analysis was performed on the measured dielectric data by using standard deviation with the upper and lower 95 % confidence limits.

3.2.6 Electrical Property Characterization

Planar electrodes were deposited onto the fresh surfaces of BT ceramics and BiI_3 single crystals by sputter coating (KJL CMS-18 Multi-Source). For BT samples, various electrodes such as Al, Ni, and Ag were deposited using different targets in order to investigate the electrode effect on dielectric properties. For BiI_3 samples, based on previous electrode compatibility work, Au was selected as an electrode material with a thickness of approximately 100 nm.⁷³ I-V characterization was performed on both BT ceramics and BiI_3 single crystals by using a microprobe station (Micromanipulator 450PM Test Station) and a semiconductor parameter analyzer (Agilent 4156C). Leakage current measurements were performed on fabricated BiI_3 single crystal detectors by an electrometer (Keithley 6517B, Cleveland, Ohio, USA) under an electric field of ± 100 V/cm.

3.2.7 Radiation Response Measurement

This process was performed by Sasmit Gockhale under the guidance of Prof. Juan C. Nino and Prof. Kelly A. Jordan. The radiation response of BiI_3 single crystal detectors was investigated using Amptek A250 charge sensitive pre-amplifiers (Bedford, MA, USA) and standard nuclear instrumentation module (NIM) electronics. Spectrum acquisition was carried out by a multi-channel analyzer (MCA) and the spectrum acquisition software Maestro 32.

3.2.8 Computational Methods

This process was performed by Dr. Minki Hong under the guidance of Prof. Juan C. Nino and Prof. Susan B. Sinnott. DFT calculations were performed to explore the Sb incorporation in the BiI_3 lattice. Projector augmented wave (PAW)^{74,75} pseudopotentials method with LDA⁷⁶ was used as implemented in the VASP software⁷⁷ and the cutoff energy for plane waves was set to 400 eV. To minimize the artificial interaction of the dopant, $2 \times 2 \times 1$ supercell containing 96 atoms was used for all calculations and a $4 \times 4 \times 4$ Monkhorst-Pack⁷⁸ k-point mesh was used. The $\text{Bi}6s^26p^3$, $\text{I}5s^25p^5$, and $\text{Sb}5s^25p^3$ were treated as valence electrons. The equilibrium lattice parameters of undoped BiI_3 were found to be $a = 7.408 \text{ \AA}$ and $c = 20.035 \text{ \AA}$, which agree well with values of $a = 7.519 \text{ \AA}$ and $c = 20.721 \text{ \AA}$ determined by XRD.³⁰ Four different sites – Bi-site, I-site, C site of Bi layer (C-site), and interstitial site in between I layers (I_{I} site) – were considered as the possible Sb incorporation sites in the BiI_3 supercell. For a better description of the band structure of Sb-doped system, spin-orbit coupling was considered.

In the next chapter, the effect of extrinsic impurities on electrical properties of BiI_3 single crystal detectors will be discussed.

CHAPTER 4
ENHANCED ELECTRICAL PROPERTIES AND RADIATION RESPONSE OF ULTRA
PURE BISMUTH TRI-IODIDE SINGLE CRYSTAL DETECTORS

4.1 Introduction

It is well known that extrinsic defects, such as impurities, have significant impact on functional properties of semiconducting materials, and thus controlling impurity level is a key to achieve high performance of fabricated devices. Thus, in this chapter, the effect of impurity level on the electrical properties and radiation performance of BiI_3 single crystal detectors will be discussed.

4.2 Ultra High Pure BiI_3 Powder Synthesis by PVT and TMZ Techniques

Several techniques, such as PVT and TMZ, have been employed to synthesize high pure BiI_3 powder. Impurity analysis was performed on PVT and TMZ synthesized BiI_3 powder by using ICP-AES, and the results are tabulated in Table 4-1 with impurity levels of commercial BiI_3 powder included for the comparison. Impurity elements which have concentrations below the detection limit (~ 1 ppm) of the equipment were marked as ND (not detected) in the table.

The total impurity levels were measured as 7.9 ppm, 26.3 ppm, and 116.9 ppm for the PVT, TMZ, and commercial BiI_3 powders, respectively. It is clear that PVT and TMZ are effective techniques to decrease the total impurity level of synthesized BiI_3 powder. Major metallic impurities in commercial BiI_3 powder were Ni (63.73 ppm) and Fe (12.83 ppm). However, these elements were not detected in PVT BiI_3 , while detected in TMZ BiI_3 powder with a very low concentration (1.6 ppm). Boron was observed as a major impurity for both PVT and TMZ BiI_3 powder possibly coming from quartz glass boats and Pyrex glass ampoules.

Although the impurity level of TMZ BiI_3 powder is not as low as PVT BiI_3 powder, the TMZ technique has advantages in terms of a much higher yield and lower cost compared to the PVT technique. Specifically, the TMZ technique is able to purify 100 g of powder in a week, while the PVT technique can yield 1 g of purified BiI_3 powder in three days.

Table 4-1. Impurity concentrations of PVT and TMZ synthesized BiI_3 powder measured by using ICP-AES.

Element	PVT (ppm)	TMZ (ppm)	Com. ^{a)} (ppm)	Element	PVT (ppm)	TMZ (ppm)	Com. (ppm)
Cu	0.3	ND ^{b)}	ND	Cr	ND	ND	ND
Ag	ND	4.2	4.47	Mn	ND	ND	ND
Pb	ND	ND	ND	Co	ND	0.1	1.57
Ni	ND	1.6	63.73	Zn	ND	ND	ND
Fe	ND	ND	12.83	As	1.3	2.7	ND
Na	ND	ND	ND	Se	ND	ND	ND
Si	ND	ND	ND	Sr	ND	ND	ND
Li	ND	ND	ND	Mo	0.1	ND	0.75
Be	ND	ND	ND	Cd	0.1	0.1	0.1
Mg	1.1	ND	0.58	Sb	ND	ND	ND
Ca	ND	ND	6.59	Tl	ND	ND	ND
K	ND	ND	22.18	B	4.3	17.5	2.36
Ti	ND	ND	0.73	Al	ND	ND	1.03
V	ND	ND	ND	Ba	0.7	0.1	ND

a): commercial, b): not detected

4.3 Electrical Properties and Radiation Response of Ultra-Pure BiI_3 Single Crystal Detectors

BiI_3 single crystal detectors were fabricated using PVT BiI_3 powder, and electrical properties, such as resistivity and leakage current, and radiation response were characterized. It is important to note that the detectors fabricated by using TMZ BiI_3 powder did not show any improvement in terms of electrical properties and radiation response such that further discussion will be focused solely on PVT BiI_3 single crystal detectors.

In order to determine the resistivity of the fabricated detector, I-V characterization was performed on BiI_3 detectors with Au electrode (~ 100 nm) deposited by using sputtering, and the result is represented in Figure 4-1. The detectors showed Ohmic IV characteristic, and the resistivity of PVT BiI_3 detector was determined as $2.27 \times 10^{10} \Omega \cdot \text{cm}$, which is much higher (two orders of magnitude) than that of BiI_3 detector fabricated from commercial BiI_3 powder ($2.55 \times 10^8 \Omega \cdot \text{cm}$). This clearly demonstrates that extrinsic defects (i.e., metallic impurities) can significantly affect electrical properties of the device. Higher resistivity is favored for gamma-ray semiconductor detectors, since it ensures lower dark current flowing through the device and therefore high signal / noisy ratio can be expected.

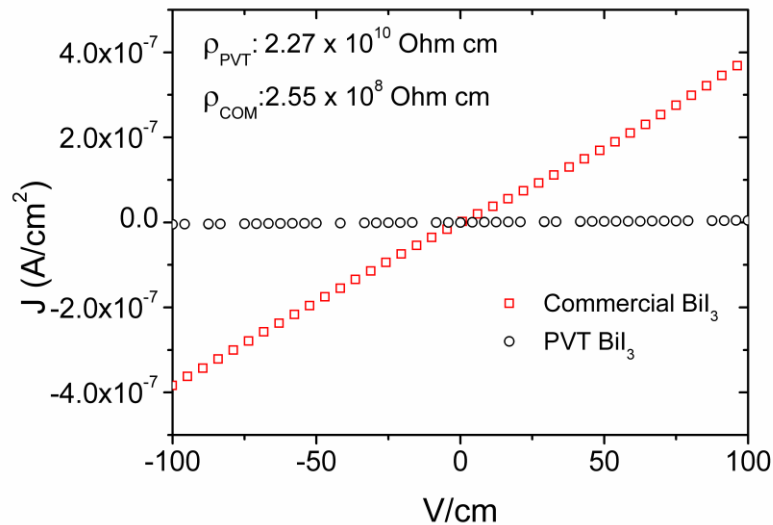


Figure 4-1. IV characteristics of the PVT and commercial BiI_3 detectors.

Leakage current was measured for the detectors to determine the variation of dark current flowing through the device under a constant bias for prolonged times. Figure 4-2 shows the results for leakage current measurements of the detectors fabricated from PVT and commercial BiI_3 crystals. It is shown in Figure 4-2 that the

leakage current of the PVT BiI_3 detector is orders of magnitude lower compared to that of the commercial BiI_3 detector. In addition, it is important to note that the ultra-pure PVT BiI_3 detector performed consistently during subsequent tests and had low leakage current compared to the commercial BiI_3 detector.

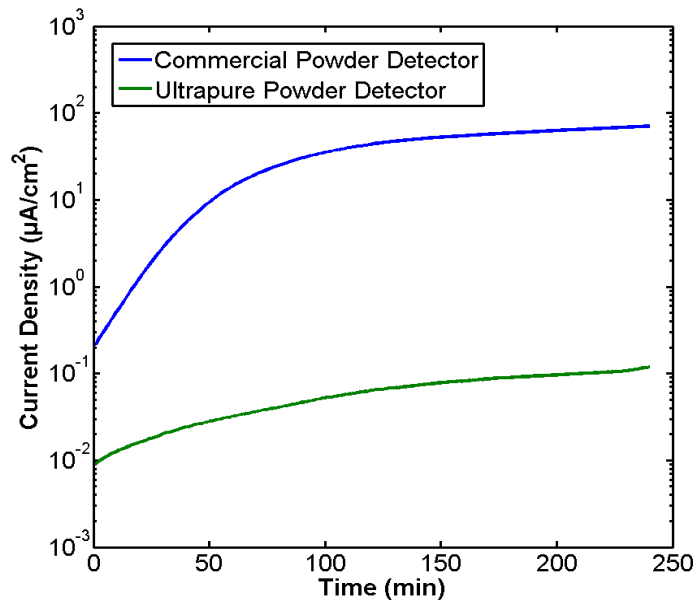


Figure 4-2. Leakage current comparison between PVT and commercial BiI_3 detectors.

Radiation responses of the ultra-pure PVT BiI_3 detector were recorded at room temperature using an Americium-241 (^{241}Am) α -particle source (Figure 4-3). The full width at half maximum (FWHM) for the spectrum was calculated as 1.46 MeV, which is 34 % improved energy resolution than previously reported value for commercial BiI_3 detectors.²⁹ However, the detector stopped working after approximately 1 ~ 2 h possibly due to background noisy and the leakage current in the detector overwhelmed the output signal preventing any true radiation signal from being recorded. This might be due to polarization effect of intrinsic defects in BiI_3 . The polarized intrinsic defects may build internal electric field in opposite direction to the external field such that prevents radiation-generated electron-hole pairs from being collected through the

circuit. The possible solution via defect engineering to overcome this problem will be further investigated in the following chapter.

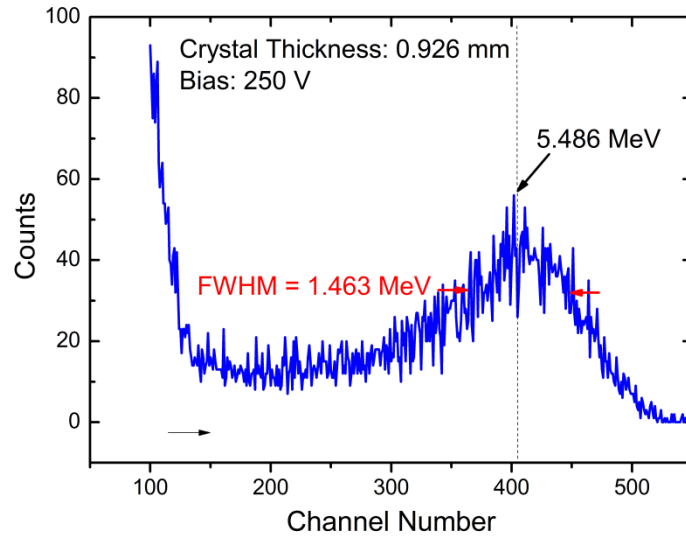


Figure 4-3. ^{241}Am α -particle spectrum recorded from the ultra-pure PVT BiI_3 detector at room temperature.

4.4 Conclusion

The effect of impurity level on electrical properties and radiation response was investigated for BiI_3 semiconductor detectors. Material purification techniques such as PVT and TMZ were applied to synthesize high pure BiI_3 starting materials. Ultra-pure BiI_3 powder was successfully synthesized through PVT method, which has total impurity level less than 10 ppm. BiI_3 single crystals were grown by using ultra-high pure PVT BiI_3 powder. The fabricated detectors show resistivity up to $10^{10} \Omega\cdot\text{cm}$, which is two orders of magnitude higher than that of BiI_3 detectors fabricated from commercially purchased powder (total impurity level of approximately 200 ppm). In addition, the leakage current of ultra-high pure BiI_3 detectors was significantly lower (two orders of magnitude) than that of commercial BiI_3 detectors. Furthermore, the energy resolution

for radiation detection of PVT detector (1.4 MeV) was improved up to ~ 34 % compared to commercial BiI₃ detector (2.2 MeV), while PVT BiI₃ detector showed polarization effect after a few hours under bias possibly due to high concentration of intrinsic defects and migration of those charged defects in the material.

CHAPTER 5
DEFECT MODELING AND ENGINEERING OF BISMUTH TRI-IODIDE SINGLE
CRYSTALS: ENHANCED ELECTRICAL AND RADIATION DETECTION
PERFORMANCE

¹5.1 Introduction

In this chapter, firstly, theoretical defect modeling for BiI₃ system will be discussed via extrinsic donor doping approach. Then, defect engineering strategies will be proposed in order to reduce high polarization effect in BiI₃ detector owing to high concentration and migration of iodine vacancies, and finally to achieve enhanced electrical properties and radiation detection performance of BiI₃ compound as a promising radiation detector material.

5.2 Defect Modeling of BiI₃ Single Crystals: Donor (Te) Doped BiI₃

Tuller and Bishop *et. al.* has proved that donor doping can complete theoretical defect modeling for certain material.^{24,79} Thus, in order to understand and establish an intrinsic defect model for BiI₃, Te has been selected as a donor dopant, based on Humm-Rothery rules (Table 5-1).

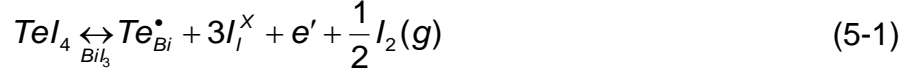
Table 5-1. Te⁴⁺ substitutional donor dopant for Bi³⁺.

	Coordination number	^{a)} Δr _{ion} (%)	^{b)} ΔE _{neg}
Te ⁴⁺	6	5.13	0.08

^{a)}Δr_{ion}: Ionic radius difference, and ^{b)}ΔE_{neg}: electronegativity differences between Te⁴⁺ and Bi³⁺.

Te will introduce compensating less mobile intrinsic defects (bismuth vacancies) by substituting for bismuth atoms (equations (5-1) and (5-2)).

¹ Reprinted with the permission from *Journal of Physical Chemistry C*, in press. Unpublished work copyright 2014 American Chemical Society. Titled “Defect Engineering of BiI₃ Single Crystals: Enhanced Electrical and Radiation Performance for Room Temperature Gamma-Ray Detection,” by HyukSu Han, Minki Hong, Sasmit S. Gokhale, Susan B. Sinnott, Kelly Jordan, James E. Baciak, and Juan C. Nino. It is reprinted with permission from Wiley-Blackwell. doi: 10.1021/jp411201k



For the overall charge neutrality, equation (5-2) should be satisfied.

$$[V_I^{\bullet}] + [Te_{Bi}^{\bullet}] = 3[V_{Bi}^{\bullet}] \quad (5-2)$$

Thus, extrinsic Te dopants will increase the concentration of intrinsic bismuth vacancies in BiI_3 . Furthermore, total ionic conductivity of BiI_3 where Schottky defects dominate defect equilibria can be written as,

$$\sigma_{total} = 3q[V_{Bi}^{\bullet}] \frac{\mu_{o,Bi}}{T} \exp\left(-\frac{\Delta H_{m,Bi}}{kT}\right) + q[V_I^{\bullet}] \frac{\mu_{o,I}}{T} \exp\left(-\frac{\Delta H_{m,I}}{kT}\right) \quad (5-3)$$

and the equilibrium constant for Schottky defect reaction in BiI_3 can be given as,

$$K_S = \frac{[V_{Bi}^{\bullet}][V_I^{\bullet}]^3}{[Bi_{Bi}^X][I_I^X]} = \exp\left(-\frac{\Delta H_S}{kT}\right) \quad (5-4)$$

where ΔH_S is the enthalpy for Schottky defect formation in BiI_3 lattice and, Bi_{Bi}^X and I_I^X represent the concentrations of Bi and I lattices, respectively.

In a donor doped BiI_3 system, two separate regions (intermediate and low temperature) at the extrinsic region of the $\text{Log}(\sigma T)$ vs. $1/T$ plot will appear due to increased bismuth vacancies introduced by Te dopants. For the extrinsic low temperature region, the slope in $\text{Log}(\sigma T)$ vs. $1/T$ plot should be equal to $\Delta H_{m,Bi} / k$, since the concentration of bismuth vacancies is much larger than iodine vacancies, neglecting the second term in equation (5-3). Also, the concentration of bismuth vacancies is equal to one third of the concentration of tellurium dopants by equation (5-2).

$$[Te_{Bi}^{\bullet}] \cong 3[V_{Bi}^{\bullet}] \quad (5-5)$$

However, at the extrinsic intermediate temperature region, even though the concentration of bismuth vacancies is larger than iodine vacancies, iodine vacancies can dominate the total ionic conductivity of BiI₃ owing to higher mobility at the elevated temperature when compared to bismuth vacancies. As such, the concentration of iodine vacancies can be calculated by substituting equation (5-5) into (5-4),

$$[V_I^*] = \left(\frac{3[Bi_x^{i\cdot}][I_x^{x\cdot}]K_S}{[Te_{Bi}^*]} \right)^{1/3} = \left(\frac{3[Bi_x^{i\cdot}][I_x^{x\cdot}]}{[Te_{Bi}^*]} \right)^{1/3} \exp\left(-\frac{\Delta H_S}{3kT}\right) \quad (5-6)$$

Thus, the slope of Log(σT) vs. 1/T plot at the extrinsic intermediate temperature region will be equal to $\left(-\frac{\Delta H_S}{3} - \Delta H_{m,I}\right)/k$ by substituting equation (5-6) into (5-3), neglecting the first term in equation (5-3). Combined with the information from the intrinsic high temperature region where intrinsic Schottky defects dominate defect formation, all the necessary variables for establishing a defect model of BiI₃ (i.e. Schottky defect formation energy, migration energies, concentrations, and mobilities for bismuth and iodine vacancies) can be extracted from the Log(σT) vs. 1/T plot. Table 5-2 summarizes the dominant defect types and concentrations for BiI₃ at separated extrinsic regions due to Te doping. Figure 5-1 illustrates anticipated slopes in the Log(σT) vs. 1/T plot for donor (Te) doped BiI₃.

Table 5-2. Summary of the dominant defect type and concentration for and the slope in the Log(σT) vs. 1/T plot.

	high temp region	intermediate temp region	low temp region
Dominant defect	V_I^*	V_I^*	V_{Bi}'''
Concentration	$(3[Bi_x^{i\cdot}][I_x^{x\cdot}])^{1/4} \exp\left(-\frac{\Delta H_S}{4kT}\right)$	$\left(\frac{3[Bi_x^{i\cdot}][I_x^{x\cdot}]}{[Te_{Bi}^*]}\right)^{1/3} \exp\left(-\frac{\Delta H_S}{3kT}\right)$	$\frac{[Te_{Bi}^*]}{3}$
Slope in Log(σT) vs.	$\left(-\frac{\Delta H_S}{4} - \Delta H_{m,I}\right)/k$	$\left(-\frac{\Delta H_S}{3} - \Delta H_{m,I}\right)/k$	$\Delta H_{m,Bi}/kT$

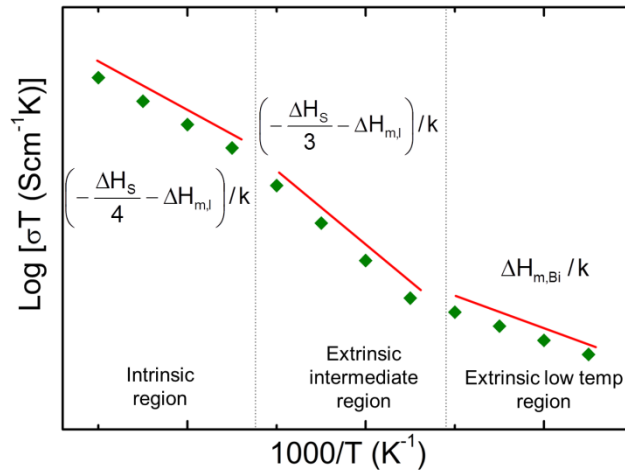


Figure 5-1. Anticipated slopes in $\text{Log}(\sigma T)$ vs. Temp plot for donor doped BiI_3 .

Based on the hypothesis above, efforts were made on single crystal growth of Te doped BiI_3 . Tellurium (IV) iodide (99.9 % - TeI_4) was purchased from Strem Chemicals, Inc. and doped into commercial BiI_3 powder with the concentrations of 40 and 120 ppm. These amounts were determined by following H. I. Tuller's work on the defect modeling for TlBr single crystal.⁷⁹ Figure 5-2 shows a successfully grown Te doped BiI_3 single crystal extracted from the as-grown polycrystalline boule.

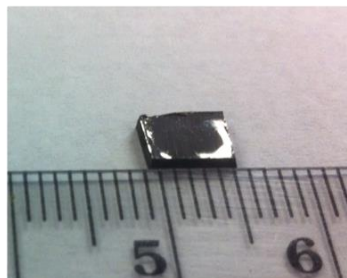


Figure 5-2. Te doped BiI_3 single crystal. Photo(s) courtesy of HyukSu Han.

In order to investigate Te concentrations in donor doped BiI_3 , the grown polycrystalline bulks were cut into several 10 mm segments and dissolved in HCl to perform

ICP-AES measurements. Figure 5-3 shows ICP-AES results for the 40 ppm and 120 ppm Te doped BiI_3 single crystals (TBI-40 and TBI-120), respectively. It was observed that for TBI-40, Te was homogeneously distributed with the average concentration of 31.3 ± 4.27 ppm along the crystal. However, relatively inhomogeneous dopant distribution was found in TBI-120, and dopants were segregated at the ends of the crystal while the middle of the crystal has an initially intended dopant concentration (120 ppm). Thus, all the samples were extracted from the middle of the crystal for the ionic conductivity measurements.

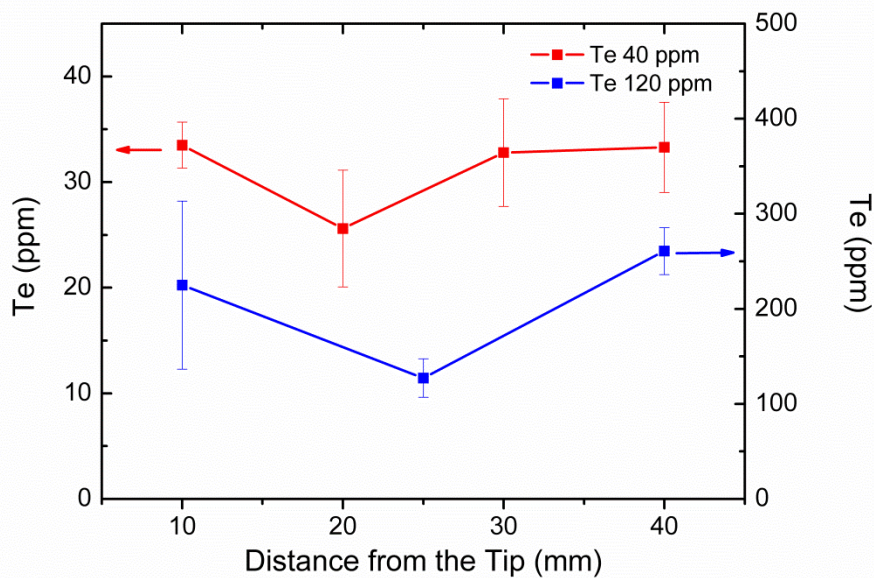


Figure 5-3. ICP analysis for Te concentrations along the distance from the tip.

Impedance analyses were performed on TBI crystals in order to extract formation and migration energies of intrinsic defects in BiI_3 , and Figure 5-4 shows Arrhenius plots for measured grain ionic conductivities from TBI-40 and TBI-120 respectively. Activation energy transition was observed at $\sim 80^\circ\text{C}$ due to activated Schottky defect formation at elevated temperature. However, activation energy transition at

intermediate temperature region was not presented for the ionic conductivity data of TBI-40 and TBI-120, which was expected based on the defect modeling for donor doped BiI_3 . This might be due to the low concentration of the compensating defects (bismuth vacancy for this case) introduced by extrinsic dopants (Te), and thus ionic conduction at low temperature may still be dominated by iodine vacancies with a higher mobility and concentration compared to bismuth vacancy. Therefore, BiI_3 single crystals dope with higher donor dopant concentration should be grown and tested for impedance measurements in order to investigate the characteristics of native defects in BiI_3 .

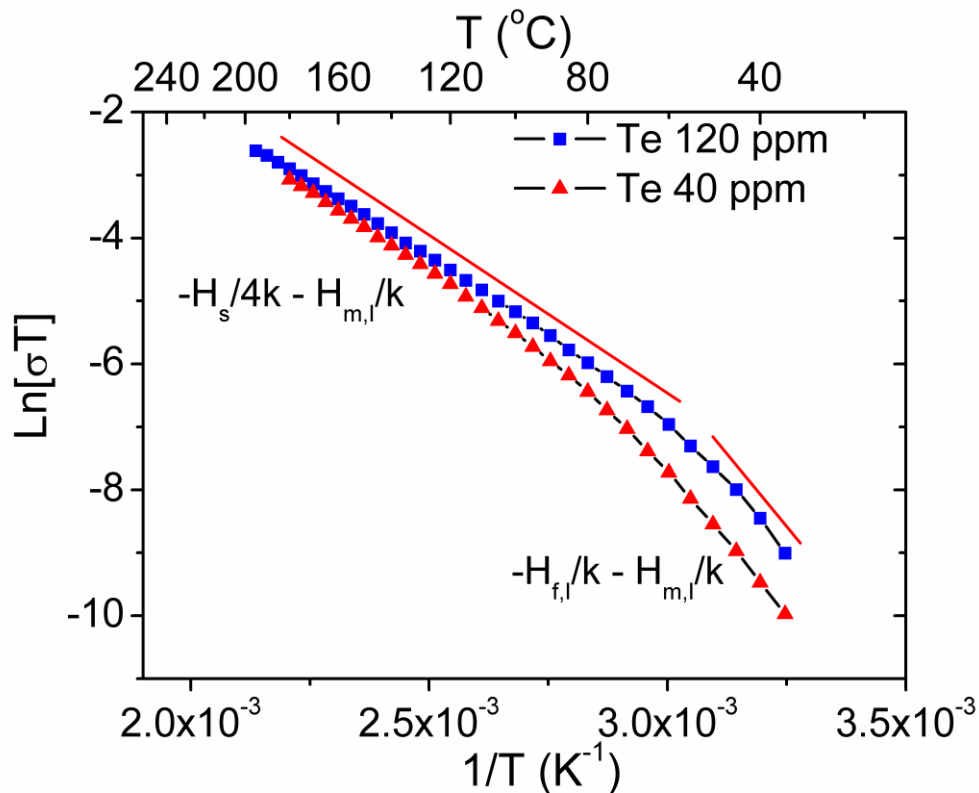


Figure 5-4. Ionic conductivity of Te doped BiI_3 single crystals as a function of temperature.

5.3 Defect Engineering of BiI_3 Single Crystals: Sb doped BiI_3 Single Crystal

Although all XI_3 ($X = \text{As}, \text{Sb}, \text{and Bi}$) compounds are isomorphic (space group $R\bar{3}$), it has been shown that the molecular characteristics of the XI_3 units increase from

BiI_3 to SbI_3 and to AsI_3 . As a result, AsI_3 can have three-fold coordination and the molecular geometry is almost the same as that of gas phase AsI_3 , while BiI_3 exhibits nearly perfect six-fold coordination of the metal, and the molecular character is lost in BiI_3 . The molecular characteristics of SbI_3 are in between those of BiI_3 and AsI_3 .^{66,67} This trend can be explained by the different types of bonding available for the metal atom. Namely, the electronic configuration of group-V metals (ns^2np^3) enables XI_3 compounds to have either ionic or covalent bonding characteristics. For the perfect ionic case, only three p electrons participate in the bonding and donate to the six iodine ions in neighboring octahedral sites. However, in the pure covalent case, the metal atoms tend to have complete sp^3 hybridization and form three covalent bonds with iodine atoms which leaves one lone pair of electrons belonging to the metal atom. As a consequence, although isomorphous, in the solid state XI_3 compounds exhibit distinct molecular characteristics. Taking advantage of this, the dopant of group V metal (i.e., Sb) was doped into the BiI_3 lattice to create covalent bonds with iodine atoms and thus successfully inhibit the formation and the migration of iodine vacancies resulting in reduced ionic conductivity in BiI_3 . As a result improved electrical properties as a high energy radiation detector, such as higher resistivity, lower leakage current, and less polarization effect, can be expected in Sb doped BiI_3 (SBI) system.

A series of doping levels, such as 0.5 at%, 1.0 at%, and 5.0 at%, were doped into BiI_3 , and SBI single crystals were grown using previously optimized growth conditions.^{28,29} The experimental XRD patterns of BiI_3 and SBI single crystals with the theoretical pattern are shown in Figure 5-5. Given the crystal habit, the XRD patterns only consist of reflections parallel to the (001) plane such as (003), (006), (009), and

(0012) and the observed peak positions for the BiI_3 single crystal were in good agreement with the published powder diffraction data for a rhombohedral crystal structure (JCPDS PDF# 48-1795). Peak shifts and intensity decreases were found in the XRD pattern of SBI single crystal possibly due to the lattice parameter change when Sb substitutes Bi atoms and the difference of atomic scattering factors between Bi and Sb atoms, respectively (Figure 5-5). In addition, the XRD pattern verified that no secondary phase exists in the SBI single crystal.

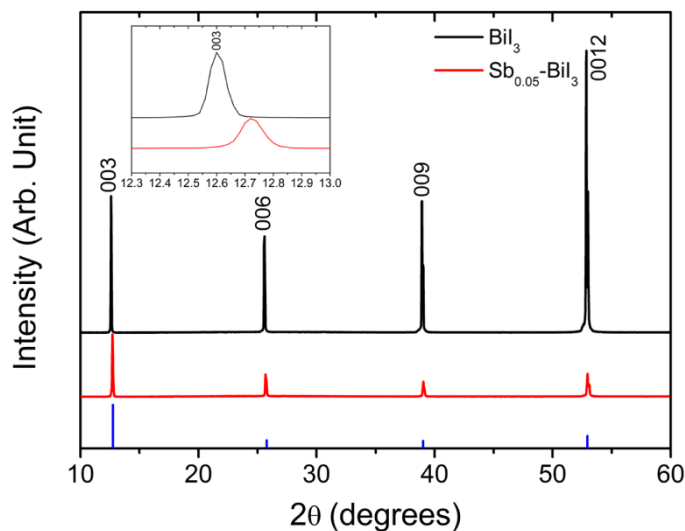


Figure 5-5. XRD patterns for BiI_3 and SBI single crystals.

The chemical composition of grown BiI_3 and SBI single crystals was investigated by ICP-AES measurements. Table 5-3 shows ICP-AES results for BiI_3 and SBI (Sb = 5 at%) single crystals. Total impurity levels of 137.5 ppm and 74.3 ppm were observed for BiI_3 and SBI single crystals, respectively. The major impurity for BiI_3 was Cu with a concentration of 130.4 ppm, while Ca with a concentration of 21.6 ppm was the major impurity for SBI. Furthermore, ~5 % of Sb was detected in the SBI single crystal while Sb was not detectable in the BiI_3 single crystal. This demonstrates that Sb is successfully doped into the BiI_3 single crystal during the crystal growth process. It is

important to note that although the starting materials were the same, different impurity levels were observed for BiI₃ and SBI crystals since each impurity element has different solubility in BiI₃ and SBI lattices, respectively.

Table 5-3. ICP-AES analysis on (a) BiI₃ and (b) SBI single crystals.
(a) BiI₃

element	c. ^{a)} (ppm)	element	c. (ppm)	element	c. (ppm)	element	c. (ppm)
Cu	130.4	Mg	1.7	Cr	ND	Mo	ND
Pb	ND ^{b)}	Ca	ND	Ti	0.4	Zn	ND
Ni	0.4	Fe	4.2	Co	0.4	Sb	ND

(b) SBI

element	c. (ppm)						
Cu	18.6	Mg	ND	Cr	ND	Mo	ND
Pb	ND	Ca	21.6	Ti	4.3	Zn	11.7
Ni	9.3	Fe	8.8	Co	ND	Sb	5 (%)

^{a)}Concentration, ^{b)} Not detectable (impurity level under 1 ppm)

To further support the defect engineering strategy, it is necessary to determine the precise incorporation site of the Sb dopants and investigate the bonding nature between Sb and neighboring ions. It has been proposed by Motsnyi *et al.* that dopants might reside mainly between the layers of BiI₃ single crystal forming covalent bonds between neighboring layers, which gives rise to “covalent bridges”.⁸⁰ However, there has not been any detailed, fundamental research on the incorporation of dopants in the BiI₃ lattice. To this end, the SBI system was modeled by DFT and the defect formation energy (DFE) of Sb at four possible incorporation sites was calculated. The DFE of a point defect or impurity (α) with charge q , $E^f(\alpha^q)$, is defined as follows:

$$E^f(\alpha^q) = E^{total}(\alpha^q) - E^{total}(\text{BiI}_3, \text{bulk}) - \sum n_i \mu_i + q(E_V + E_f + \Delta V) \quad (5-7)$$

where $E^{\text{total}}(\alpha^q)$ is the total energy of the system with a defect, $E^{\text{total}}(\text{BiI}_3, \text{bulk})$ is the total energy of the system in the absence of a defect, and μ_i is the chemical potential of species i , which is added ($n > 0$) or removed ($n < 0$) from the system. E_v and E_f indicate the valence band maximum (VBM) of the perfect supercell and the Fermi energy referenced to the VBM, respectively. Lastly, ΔV is the correction of the VBM deviation in the defective supercell.

The resulting DFEs are depicted in Figure 5-6. Bi-rich conditions, where the chemical potential of Bi reaches the maximum value ($\mu_{\text{Bi}} = \mu_{\text{Bi,metal}}$), were considered given that iodine compounds are normally iodine deficient during growth due to the high vapor pressure of iodine and BiI_3 dissociation into Bi and I_2 at 250 ~ 300°C.⁸¹⁻⁸³ The DFE of Sb_{Bi}^x is predicted to have the lowest energy and thus, Sb will preferably reside in the Bi-site (Figure 5-6 (B)). However, BiI_3 is normally under iodine deficient conditions that impose high concentrations of iodine vacancies in the system. Figure 5-6 (A) shows that bismuth vacancy formation is considerably suppressed over a wide range of E_f under iodine deficient conditions resulting in the significantly higher concentration of V_{I} than V_{Bi} in the BiI_3 lattice.

It is important to note that Bercha *et al.* have shown that, in theory, Sb atoms may not be incorporated in cation vacancy in the layered BiI_3 compound.⁸⁴ Interestingly, the DFE calculations in this work indicate that Sb_{I}^* , Sb_{C}^* , and $\text{Sb}_{\text{I-L}}^*$ have nearly the same DFEs and are in competition with each other for Fermi energies of 0.4 eV or less. However, for Fermi energies above this value, Sb_{Bi}^x is predicted to have the lowest DFEs compared to those of other charged defects except for the Sb_{Bi}^x (Figure 5-

6 (B)). It can thus be hypothesized that under Bi-rich conditions, the Bi-site and I-site become the preferred Sb incorporation sites within the BiI_3 lattice.

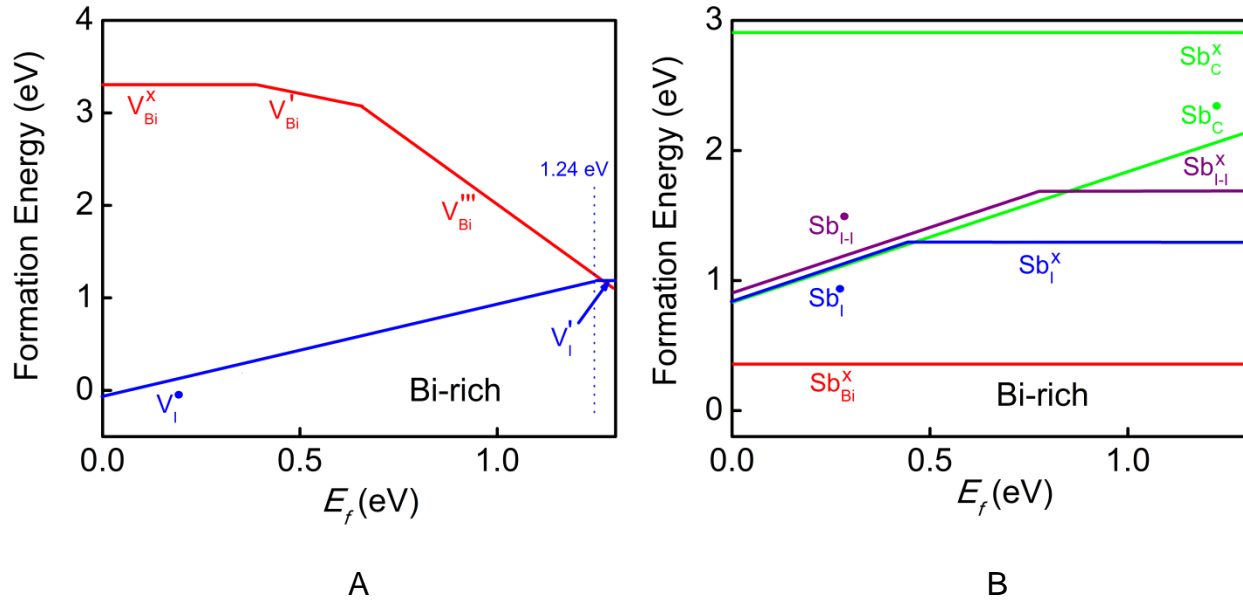
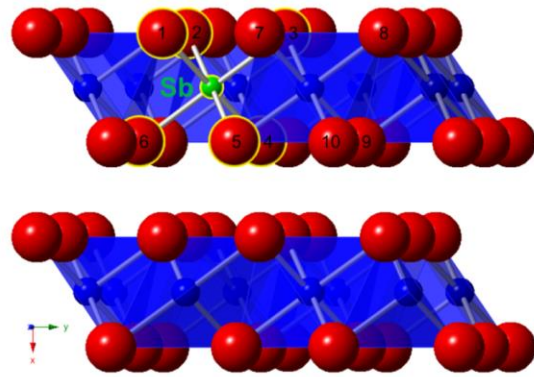


Figure 5-6. Calculated formation energies as a function of Fermi energy for A) iodine and bismuth vacancies and B) Sb_{Bi} , Sb_{I} , Sb_{C} , and $\text{Sb}_{\text{I-I}}$ in BiI_3 under Bi-rich conditions.

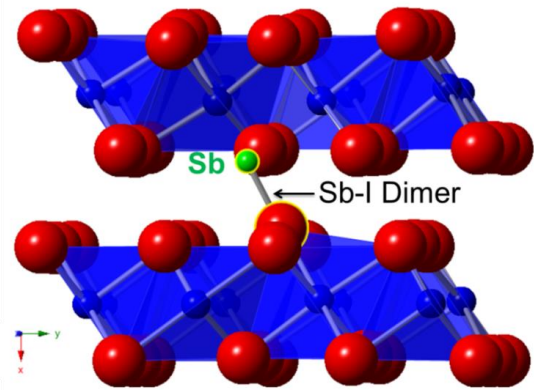
DFT calculation results for cases when Sb incorporates in the Bi-site and the I-site are represented in Figure 5-7 (A) and (B), respectively. The results predict that the resulting atomic configuration is almost identical to the pure BiI_3 system when Sb resides on the Bi-site, while Sb forms a dimer with a neighboring iodine when it incorporates in the I-site. Since Sb^{3+} has a smaller ionic radius ($r_{\text{sb}} = 90$ pm) than Bi^{3+} ($r_{\text{Bi}} = 117$ pm), it can thus be expected that the shorter and stronger Sb-I bonds, compared to the Bi-I bonds, should be formed when Sb incorporates in Bi-site.⁸⁵ Table 5- indicates the bond lengths of the Sb and Bi ions with the surrounding I ions, and clearly demonstrates that the above statement holds true for this system. In addition, Sb-I dimer formation was predicted by the DFT calculations with a shorter bond length

of ~ 2.8 Å compared to that of Bi-I at equilibrium (~ 3.06 Å) when Sb incorporates in the I-site (Figure 5-6 (B)).

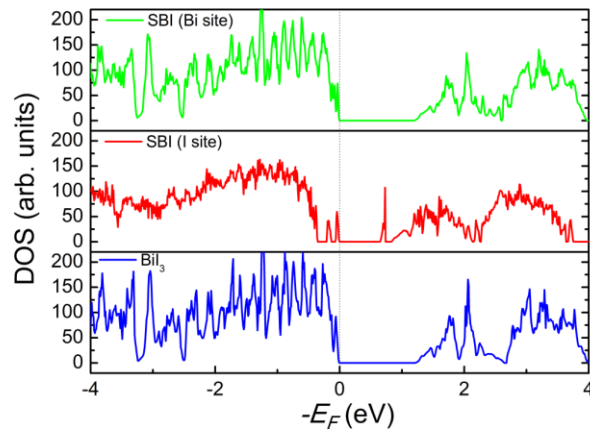
Figure 5-7 (C) represents the total density of state (DOS) for pure BiI_3 , SBI (Sb incorporated in Bi-site), and SBI (Sb incorporated in I-site), respectively. The band gap of ~ 1.3 eV was predicted for pure BiI_3 , which is a slight underestimation ($\sim 15\%$) relative to previous calculations; this is not unexpected as the local density approximation (LDA) pseudopotentials were used in these calculations.⁸⁶⁻⁸⁸ It is worth mentioning that spin-orbit coupling is required in order to establish the proper distribution of energy states near the band gap. The total DOS of Sb doped BiI_3 was predicted to be nearly identical to that of undoped BiI_3 when Sb incorporates in the Bi-site given that no additional energy states were created. In contrast, the total DOS for Sb doped BiI_3 at I-site shows that energy states were created just above the valance band and just below the conduction band; the energy states near the valance band are occupied by electrons, while the energy states near the conduction band are empty. The partial DOS analysis also confirmed that the energy states just above the valance band are due to Sb and the surrounding Bi and I ions while the states near the conduction band originated purely from the Sb-I dimer. Moreover, it was determined that a clear hybridization of $\text{Sb}5p$ and $\text{I}5p$ exists in the energy state of Sb-I dimer implying the bonding nature of Sb-I dimer is highly covalent (Figure 5-7 (C)). The difference between the states formed by Sb-I dimer and valance band (~ 1.0 eV) is almost equal to the energy of the observed peak from the photoluminescence spectra of Sb doped BiI_3 single crystal.⁸⁰



A



B



C

Figure 5-7. Crystal structures of A) SBI (Sb at Bi-site) B) SBI (Sb at I-site) and C) total density of states (DOS) for SBI (Sb at Bi-site), SBI (Sb at I-site), and pure BiI₃.

Table 5-4. Sb-I and Bi-I bond lengths in Sb incorporated BiI₃ on Bi-site.

	bond length (Å)		bond length (Å)
Sb-1	3.012	Bi-7	3.049
Sb-2	3.011	Bi-3	3.047
Sb-3	3.011	Bi-8	3.052
Sb-4	2.993	Bi-9	3.064
Sb-5	2.994	Bi-10	3.068
Sb-6	2.994	Bi-5	3.062

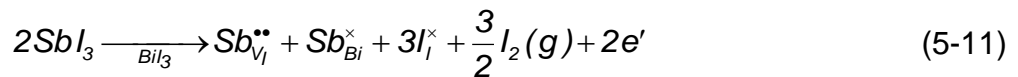
Recalling, the ionic conductivity (σ_i) of the material is related to the concentration of the vacancies and/or interstitials through equation (2-36), and the mobility of the charge carrier i can be defined by,

$$\mu_{d,i} = \frac{\mu_{o,i}}{T} \exp\left(-\frac{H_{m,i}}{kT}\right), \quad (5-8)$$

where $\mu_{o,i}$ and $H_{m,i}$ are the pre-exponential factor and the migration energy for the charge carrier i . Given that Schottky defects are the dominant defect complexes and iodine vacancy dominates ionic conduction in BiI₃, ionic conductivity of BiI₃ can be written as,^{32,34,35}

$$\sigma_i \cong q[V_I^\bullet] \frac{\mu_{o,i}}{T} \exp\left(-\frac{H_{m,i}}{kT}\right) \quad (5-9)$$

Moreover, the defect reaction when Sb is incorporated in the Bi-site (most likely substitutional) and the I-site (most likely iodine vacancy) can be respectively described by,



As demonstrated by the DFT calculations, substituted Sb atoms may be able to increase the formation energy of iodine vacancies by creating stronger and shorter bonds between Sb and neighboring I ions when Sb incorporates in the Bi-site (equation (5-10)). It has also been demonstrated that for CdTeZn (CZT), a certain amount of Zn dopants in CdTe will increase defect formation energies by forming less ionic Zn-Te bonds. Furthermore, according to equation (5-11), Sb will effectively decrease the number of jumping sites for iodine ions as they occupy V_I sites when Sb resides on the I-site. Through these defect engineering strategies, the ionic conductivity and dark current in BiI_3 are expected to be significantly reduced.

5.4 Enhanced Electrical and Radiation Performance of Sb doped BiI_3 Single Crystal Detectors for Room Temperature Gamma-Ray Detection

To validate this defect engineering approach, the resistivity of BiI_3 and SBI single crystals were measured using a microprobe station and the results are presented in Figure 5-8 (A). The measured resistivity of the 5.0 at% and 0.5 at% doped SBI single crystals was $2.63 \times 10^9 \Omega \cdot \text{cm}$ and $2.44 \times 10^9 \Omega \cdot \text{cm}$, respectively, while 1.0 at% doped SBI crystal shows almost identical resistivity value with undoped BiI_3 ($1.45 \times 10^8 \Omega \cdot \text{cm}$). However, as expected, SBI (5.0 and 0.5 at%) has a higher resistivity (about one magnitude order) compared to that of BiI_3 single crystal. Given the promising detection performance previously shown in undoped BiI_3 , SBI can be seen as an enhanced candidate for radiation detection, since higher resistivity leads to lower dark currents of the device resulting in sensitive sensor response.

It is also important to understand the behavior of single crystal detector under a constant bias for a prolonged period of time. As such, leakage current was measured in order to investigate the variation of leakage current flowing through BiI_3 and SBI single

crystal detectors. Figure 5-8 (B) shows the comparison of the leakage current in BiI_3 and SBI single crystal (5.0, 1.0, and 0.5 at%) detectors. As illustrated in Figure 5-8 (B), the leakage current in SBI single crystal detector regardless of doping concentration is orders of magnitude lower (about a factor of 10^{-4}) than that in the undoped BiI_3 single crystal detector. In addition, it was observed that leakage current of SBI single crystal detector was initially increased up to $10^{-1} \mu\text{A}/\text{cm}^2$ and then stabilized to $10^{-2} \mu\text{A}/\text{cm}^2$ after 150 min. In contrast, leakage current of BiI_3 single crystal detector kept increasing above $10 \mu\text{A}/\text{cm}^2$ after 150 min (Figure 5-8 (B)). This result, combined with the enhanced dark resistivity of SBI, demonstrates that V_i migration can be effectively controlled by defect engineering and in particular by Sb doping strategies. A detector with the higher resistivity and the lower leakage current should have a better response to radiation since a lower dark current and a higher signal to noise ratio can be achieved, and this is critically important for radiation spectroscopy measurements.

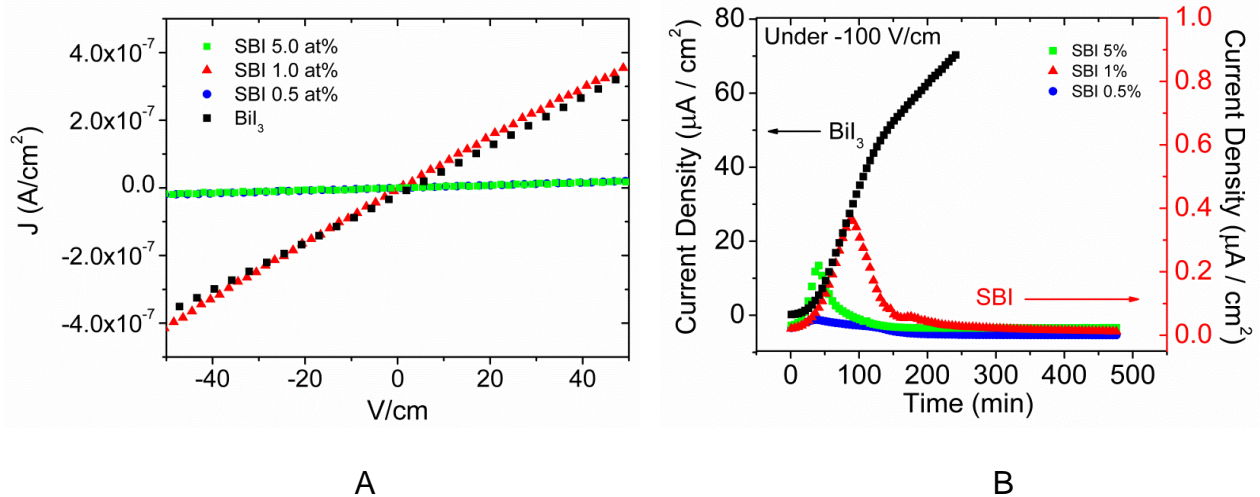


Figure 5-8. Electrical properties of BiI_3 and SBI single crystal detectors. A) IV characterization. B) leakage current measurements.

Figure 5-9 (B) shows the radiation response of SBI single crystal detector to a ^{241}Am α -source at room temperature. In addition, it is also worth noting that although the SBI crystals with different doping concentrations (5.0, 1.0, and 0.5 at%) produced distinct α -particle spectrums, SBI (5.0 at%) has been selected as the material discussed here for radiation response since it demonstrated superior radiation response in terms of long-term detector stability. Here, α -particle instead of gamma-rays has been utilized to characterize detector performances, since α -particle has a well-defined range and, thus the electrons are generated at the same depth within the detector. Therefore, using α -particle allows for a more direct measurement of the mobility and lifetime of electrons. A distinct α -spectrum was observed after 5 minutes under electric field of 532 V/cm (Figure 5-9 (B)). In our previous work, it was reported that α -spectrum for undoped BiI_3 single crystal detector disappeared only after 90 minutes under bias due to the high leakage current and the polarization effect in the detector at prolonged time (Figure 5-9 (A)).²⁸ However, in the case of SBI single crystal detector, while the count rate decreased possibly due to field variations in the detector, a clear α -spectrum was attained after 8 hours under electric field of 532 V/cm (Figure 5-9 (B)). It is a well-known phenomenon that the polarization effect is the main reason for the observed degradation of the detectors over time under steady state operating conditions. This result thus clearly demonstrates that the polarization effect in SBI single crystal detector is significantly lower with respect to that in undoped BiI_3 single crystal detector resulting in enhanced detector stability of SBI. A relative peak shift was observed in the spectrum measured after 8 hours, which is commonly observed after biasing a compound semiconductor detector for the first time spectrum measurements.⁸⁹

Resolution of the SBI detector was calculated as 62.66 % and 32.96 % for 5 min and 8 hours after biasing, respectively. Interestingly, resolution was improved after time periods possibly due to reduced and stabilized leakage currents in the detector. Although resolution of SBI detector is not as good as that of commercial CZT detectors, it is improved compared to previously reported value for undoped BiI₃ detectors (~40.15 %) ²⁹, and shows the potential of the material to function as a radiation detector.

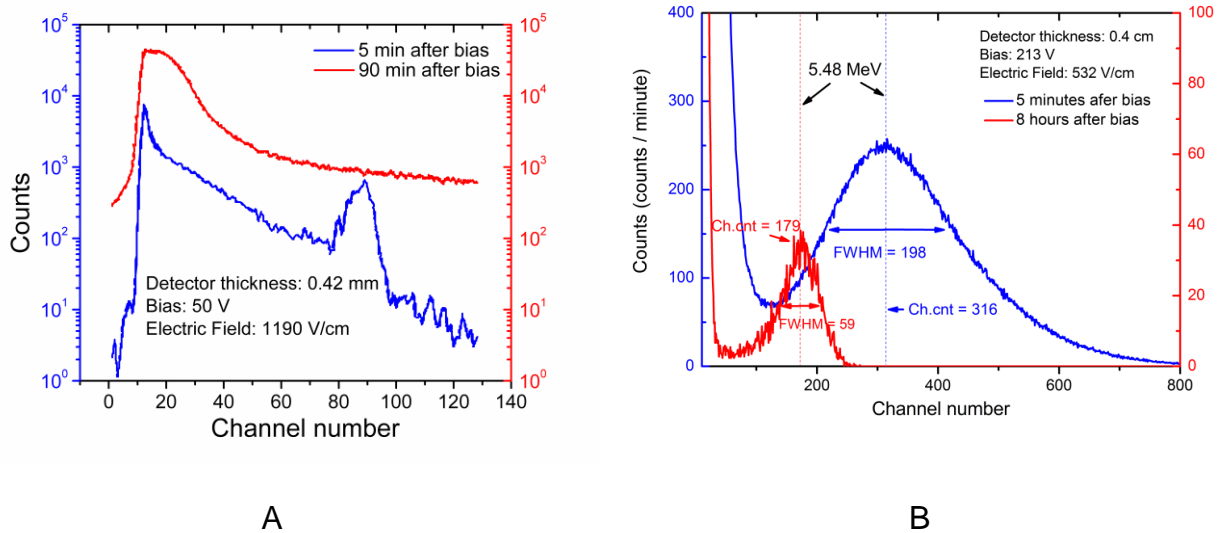


Figure 5-9. ²⁴¹Am alpha source radiation response tests for A) BiI₃ and B) SBI (5.0 at%) single crystal detectors under bias at different time periods. Ch.cnt and FWHM indicate channel number at the centroid and full width half max, respectively.

Finally, the electron mobility (μ_e) of the SBI detector was estimated by measuring the drift time (t_{drift}) for electrons from an interaction near the cathode since the electrons will drift the entire thickness of the detector. The μ_e can be calculated by,

$$\mu_e = \frac{D}{Et_{drift,e}} \quad (5-12)$$

D and E are the detector thickness (~ 0.4 cm) and the applied electric field (532.5 V/cm), respectively. ²⁴¹Am alpha source was used to irradiate the cathode of the

detector in order to estimate the drift time, and the electron rise time was recorded via output pulses. Figure 5-10 illustrates the recorded out pulse of the SBI detector using ^{241}Am alpha source. Several measurements (~10 times) of rise time were performed in order to enhance reliability of the data, and an average value of 785 ± 163 ns was calculated. It should be noted that the electron rise time is almost equal to the electron drift time since depth penetration of the α -particle is very small. Therefore, the electron mobility of the SBI detector was estimated as 1000 ± 200 cm^2/Vs . This value of electron mobility is on par with that of CZT, the leading room temperature detector material for γ - and X-rays.⁹⁰ Furthermore, defect engineering strategies in SBI have achieved the material with enhanced electron mobility (~70 %) compared to that of undoped BiI_3 detector (~600 cm^2/Vs).⁹¹ Here, the hole mobility was not measured due to the fact that wide bandgap iodine compounds experience severe hole trapping. However, a potential low hole mobility would not degrade the detector performance of SBI since single-polarity charge sensing technique can be employed to overcome this problem (i.e. hole trapping).^{92,93}

The defect engineering strategies proposed in this Chapter demonstrates the ability to tune enhanced electrical properties and radiation response of the material, though additional factors such as surface treatments and purification of starting materials are known to affect radiation detection properties of semiconductor detectors. The results of these experiments imply that controlling detrimental defects for radiation response should be considered for the search for the semiconductor materials with the superior detection properties. In particular, the present search for superior iodine compounds in

novel semiconductor detectors should consider iodine vacancy control as a dominant factor to realize enhanced electrical and radiation detection properties.

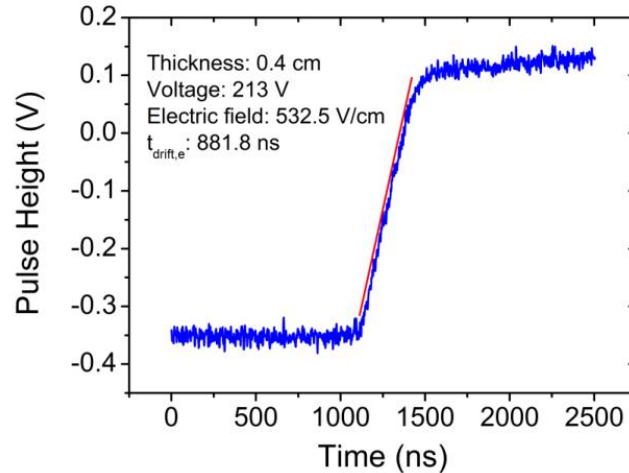


Figure 5-10. Electron rise time of the SBI detector from alpha particles.

5.5 Conclusion

Theoretical defect models for BiI_3 was established for BiI_3 system through donor doping approach, and efforts were made on extracting thermodynamical parameters for the native defects in BiI_3 , such as formation energy, migration energy, and mobility, by measuring ionic conductivities of TBI crystals as a function of temperature. Based on defect engineering strategies, the electrical properties, such as high resistivity and low leakage current, and radiation response were significantly improved in SBI single crystal detectors compared to undoped BiI_3 single crystal detectors. Leakage current measurements and α -particle radiation response demonstrate that time-dependent detection properties were also remarkably enhanced in SBI single crystal detector. In addition, the electron mobility of SBI detector was significantly enhanced (~70 %) compared to that of undoped BiI_3 detector. Density functional theory calculations and defect modeling verified that Sb dopants in BiI_3 can effectively reduce the formation and

the migration of iodine vacancies which is consistent with the enhanced electrical and radiation detecting properties in the SBI single crystal detector. Therefore, SBI single crystals can now be considered realizable materials for gamma-ray detectors surpassing undoped BiI_3 based on enhanced electrical properties and radiation response of the detector.

CHAPTER 6 COLOSSAL PERMITTIVITY IN FAST-FIRED BARIUM TITANATE CERAMICS²

6.1 Introduction

In this chapter, different processing techniques, such as SPS and MWS, will be investigated in order to induce CP in BT ceramics. Processing variables, such as sintering and annealing conditions, will be optimized to improve dielectric properties of fast-fired BT ceramics, i.e. high relative permittivity with low dielectric loss.

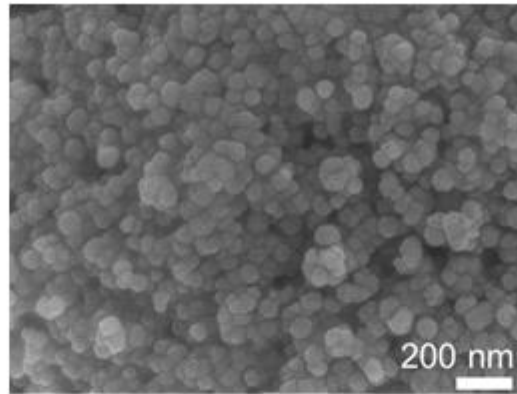
SPS and MWS are nonconventional fast-firing techniques that has been used to sinter several electronic ceramics such as $\text{Pb}(\text{Zr}_x\text{Ti}_{1-x})\text{O}_3$ (PZT) and Sr-doped PZT, and $\text{YBa}_2\text{Cu}_3\text{O}_{7-x}$.⁹⁴⁻⁹⁶ SPS and MWS also have several advantages over conventional sintering such as rapid heating rate and short sintering time.⁹⁷ These unique aspects of fast-firing techniques gives rise to severe reduction atmosphere during sintering, which results in high concentration of point defects, such as oxygen vacancies, electrons, and Ti^{3+} , in the sintered ceramics. Thus, the induced point defects in the fast-fired ceramic significantly affect dielectric properties of the material compared to the conventionally sintered ceramic.

In this study, we demonstrate that CP can be achieved in BT ceramics when sintered by SPS and MWS. In addition, post-sintering annealing conditions were optimized with the aim to reduce the dielectric loss, but to still maintain the high relative permittivity values in BT ceramics sintered by MWS technique.

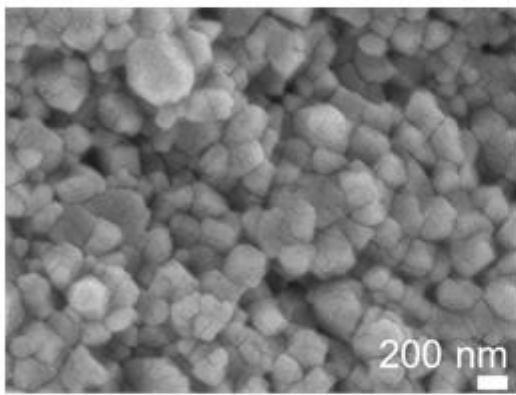
² Reprinted with the permission from Wiley-Blackwell, *Journal of American Ceramic Society*, **96** [2] 485-490 (2013), titled "Colossal Permittivity in Microwave-Sintered Barium Titanate and Effect of Annealing on Dielectric Properties," by H. Han, D. Ghosh, J. L. Jones, and J.C. Nino.

6.2 Microstructure, Density, and Phase Purity of Pressureless, Spark-Plasma, and Microwave-Sintered BaTiO₃

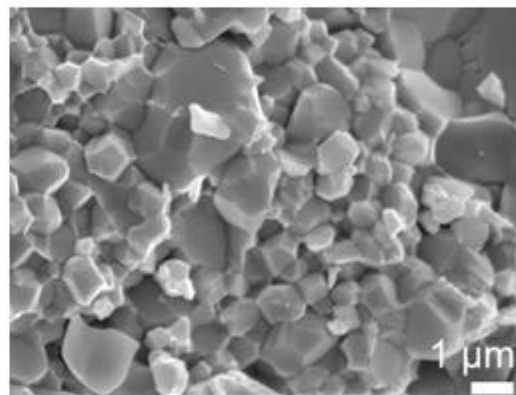
Figure 6-1 shows SEM images of the starting nanometer-sized BT powder and of the fractured surfaces of the as-sintered BT ceramics synthesized by PS, SPS, and MWS. Figure 6-1 (A) confirms that the particle size of starting BT powder was below 100 nm. Average grain sizes of $0.21 \pm 0.01 \mu\text{m}$, $0.67 \pm 0.11 \mu\text{m}$, $1.29 \pm 0.08 \mu\text{m}$, and $10.30 \pm 1.39 \mu\text{m}$ were estimated on as-sintered SPS (900°C), SPS (1050°C), MWS (1320°C), and PS (1350°C) BT samples, respectively (Figure 6-1). For the grain size measurements, the mean lineal intercept method by ASTM E112 standard, even though this method can only be used for planar grains, was applied on the SEM images from the fractured surfaces as the SPS and MWS samples were too brittle to investigate nice planar microstructures.⁹⁸ Overall, the SEM micrographs of the fractured surfaces of the sintered BT ceramics revealed that, as expected, the BT ceramic sintered by SPS at 900°C has the smallest grain size whereas the largest grain size BT ceramic was obtained when sintered by PS at 1350°C. The grain size was observed to increase from SPS BT (900°C) to SPS BT (1050°C) to MWS BT (1320°C) to PS BT (1350°C). Table 6-1 shows that the density of as-sintered SPS BT ceramics vary from 93.89% to 98.88% of theoretical value (6.02 g/cm^3) for sintering temperatures of 900°C and 1050°C, respectively. The average density of the as-sintered MWS samples was 94.15% and for the PS BT, 97.16% of theoretical density was achieved.



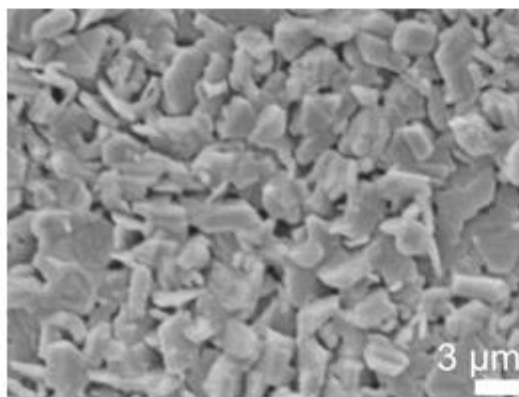
(a)



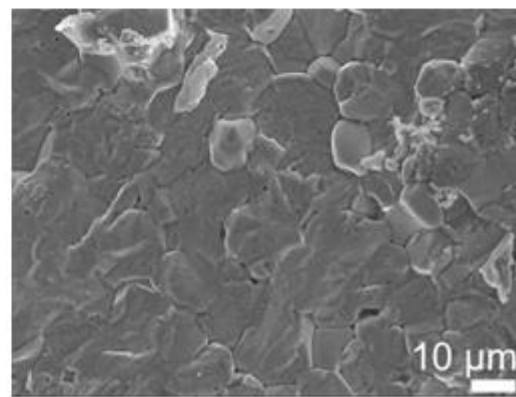
(b)



(c)



(d)



(e)

Figure 6-1. SEM micrographs of A) starting nano BT powder and fractured surfaces B) SPS 900°C C) SPS 1050°C D) MWS 1320°C E) PS 1350°C.

It was observed that all the as-sintered MWS BT (1320°C) ceramics as well as the SPS BT (1050°C) ceramic were dark blue, whereas the as-sintered SPS BT (900°C) and PS BT (1350°C) ceramics were slightly yellowish or white in color. This color change in the as-sintered MWS and SPS BT (dark blue) ceramics compared to the starting BT powder (white) can be attributed to the reduction in BT during sintering.³⁸ As mentioned previously, post-sintering annealing treatments were conducted for the MWS samples in the temperature range of 900°C ~ 1250°C in air. It was observed that color of the BT ceramics started to change gradually upon annealing and the final color after annealing was dependent on the annealing temperature and time. As the annealing temperature increased from 900°C to 1250°C, color of the BT samples gradually changed from dark blue to cream color to finally almost white at 1250°C when annealed for 24 hours. Figure 6-2 illustrates the gradual change in color of the MWS BT ceramics as a result of annealing process. In addition, sintered density of the MWS BT ceramics increased upon post-sintering annealing and the maximum density achieved after annealing at 1200°C for 24 hours was 96.30% of theoretical value (Table 6-1). These gradual color change and increased density upon annealing confirm that the reoxidation process with substantial elimination of oxygen vacancies has occurred during annealing process.

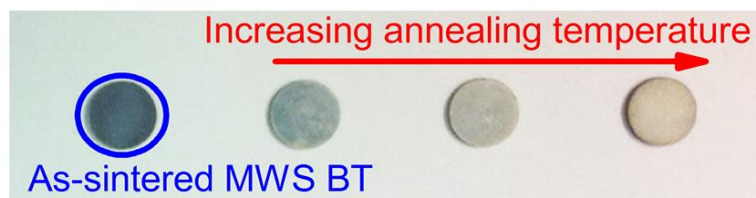


Figure 6-2. MWS BT annealed in air at different temperatures and times (1050°C for 12 h, 1100°C for 24 h, 1250°C for 24 h from left to right).

Table 6-1. Summary of sintering conditions, densities, and dielectric properties (secondary phase (5 ~ 8 %) of $Ba_6Ti_{17}O_{40-x}$ was included for density calculation of as-sintered MWS).

Sintering technique	Sintering temp (°C) / time	Heating rate	Density (%)	Grain size (μm)
MWS	1320 / 30 min	45°C / min	94.15 (as-sintered)	1.29 ± 0.08
			96.30 (annealed)	
SPS	900 / 5 min	50°C / min	93.89 (as-sintered)	0.21 ± 0.01
	1050 / 5 min		98.88 (as-sintered)	0.67 ± 0.11
PS	1350 / 2 hrs	3°C / min	97.16 (as-sintered)	10.30 ± 1.39

Figure 6-3 shows the XRD patterns of the starting BT powder and BT ceramics (before and after annealing) sintered by MWS, PS and SPS. The XRD pattern of the BT powder was typical of cubic structure (JCPDS-74-1968), however, a small amount of barium carbonate ($BaCO_3$, JCPDS-45-1471) was observed in the starting powder, which is commonly used for synthesis of BT powders. The XRD patterns of the as-sintered ceramics showed a mixture phase of cubic and tetragonal (JCPDS-05-0626) perovskite peak diffraction intensities. Although the XRD pattern of as-sintered PS BT did not reveal any secondary phase, as-sintered SPS and MWS BT ceramics showed a secondary phase (5 ~ 8 phase %) of $Ba_6Ti_{17}O_{40-x}$ (JCPDS-43-0559). This phase was still present in the MWS BT when annealed at 1050°C for 12 hours, but was completely removed when annealed at 1250°C for 24 hours. The absence of $Ba_6Ti_{17}O_{40-x}$ phase when annealed at 1250°C for 24 hours could be attributed to the reoxidation of BT ceramic during annealing process. This is consistent with the observed density and color changes.

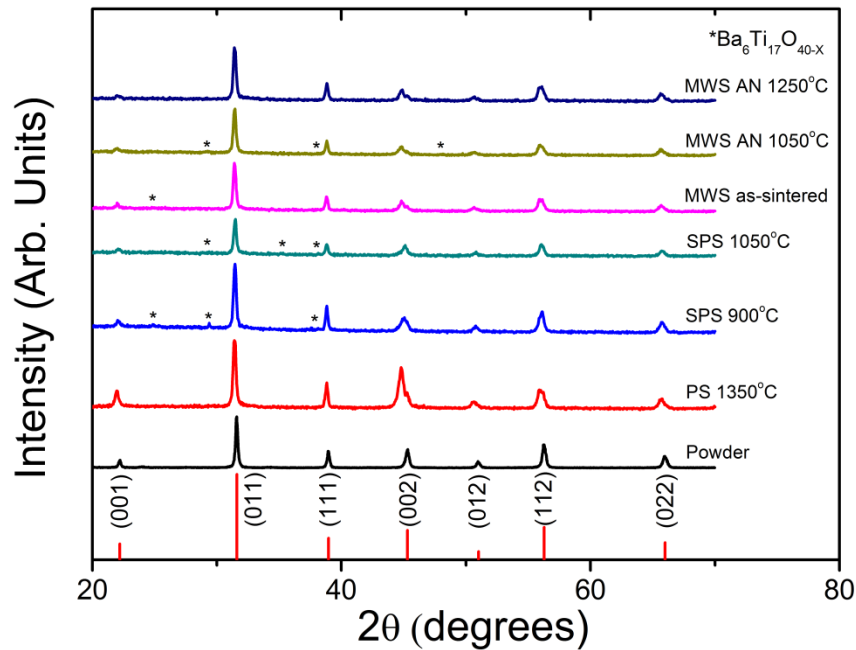


Figure 6-3. XRD patterns of nano powder, as-sintered PS, MWS, SPS, and annealed MWS BT.

6.3 Dielectric Properties of Pressureless, Spark-Plasma, and Microwave-Sintered BaTiO₃

The dielectric responses of as-sintered BT ceramics synthesized by MWS, SPS, and PS, measured in the temperature ranges of room (27°C) to 200°C and frequency ranges of 1 kHz–1 MHz, are presented in Figure 6-4. BT ceramics synthesized by PS at 1350°C showed maximum relative permittivity value of 6,810 which is typical value of BT ceramics (Figure 6-4 (A)). It is well known that BT ceramics exhibit a phase transition from cubic to tetragonal near 130°C, which is known as Curie temperature (T_c).⁹⁹ In the permittivity measurements of conventional BT ceramics, this phase transition is evidenced by sharp increase in the permittivity values near the transition temperature. The sharp peak at the transition temperature is clearly observed in the PS samples (see Figure 6-4 (A)). Figure 6-4 (B) shows dielectric properties of SPS BT

(900°C) ceramics. It was observed that the maximum relative permittivity of 6,350 was achieved near the phase transition temperature. Although permittivity values were similar to PS BT (1350°C), much higher dielectric losses ($\tan \delta \sim 0.483$) were observed above room temperature for SPS BT (900°C). The higher dielectric loss in the SPS BT (900°C) can be attributed to oxygen vacancies as a result of reduced sintering atmosphere (vacuum) and rapid heating rate in SPS.¹⁰⁰ Furthermore, it has been shown that the phase transitions in BT ceramics become diffuse in nature when the grain size approaches submicrometer range or lower,¹⁰¹ and thus the observed diffused peak at the phase transition temperature (Figure 6-4 (B)) might be due to submicrometer grain size of SPS BT (900°C) ceramic. Even though none of PS BT (1350°C) and SPS BT (900°C) samples show CP, considering the size-effect on permittivity of sintered BT ceramics,¹⁰¹ slightly higher permittivity of the PS BT than the SPS BT (900°C) at the phase transition temperature could be attributed to the higher grain size in the former than that in the latter. On the other hand, dielectric measurements of as-sintered BT ceramic synthesized by SPS at 1050°C revealed CP of the order of 10^5 at room (27°C) to 200°C (Figure 6-4 (C)). No discernible peak at the transition temperature was observed (Figure 6-4 (C)), and the increase in the sintering temperature from 900°C to 1050°C resulted in a significant increase in the dielectric loss. Table 6-2 summarizes relative permittivity and dielectric loss for as-sintered MWS, SPS, and PS BT ceramics.

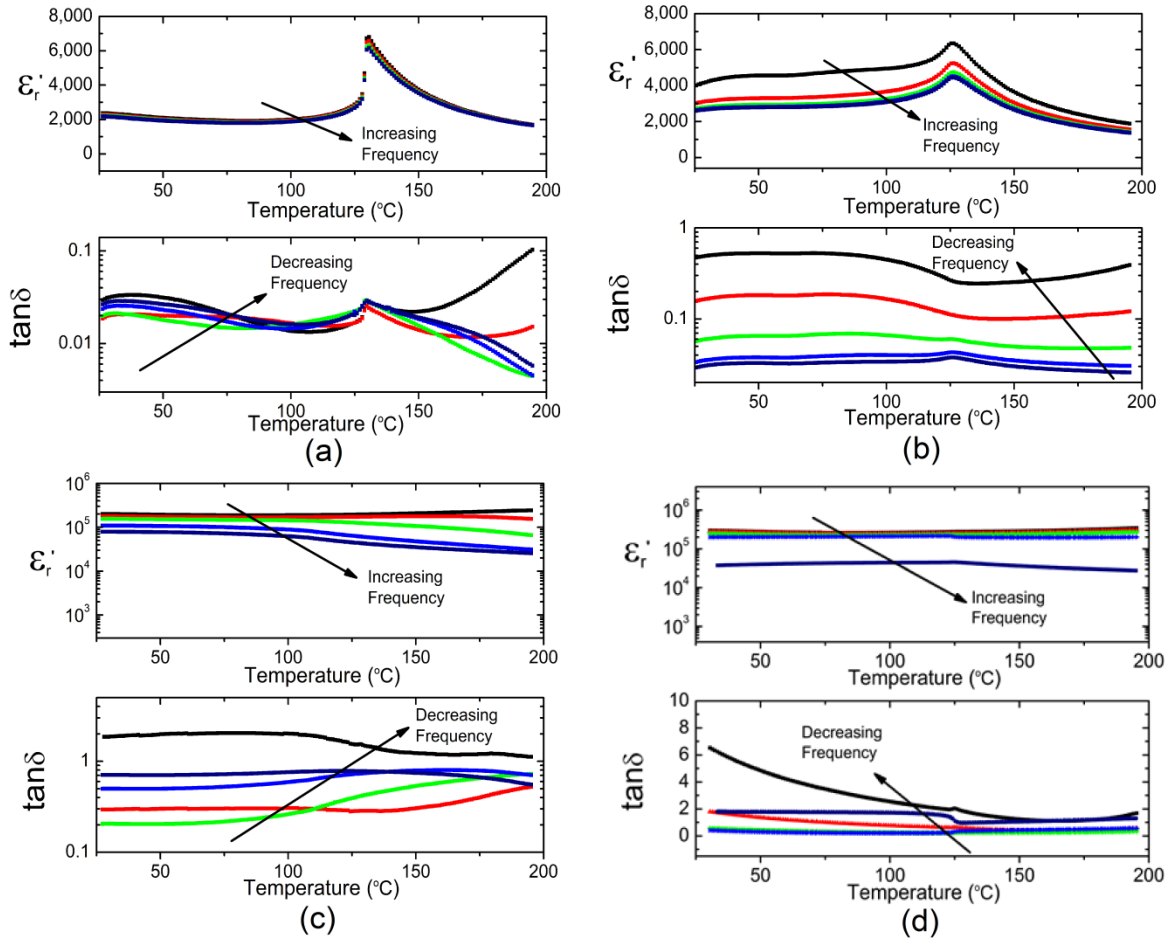


Figure 6-4. Dielectric properties of as-sintered A) PS (1350°C) B) SPS (900°C) C) SPS (1050°C) D) MWS (1320°C) BT at 1, 10, 100, 500 kHz, and 1 MHz.

Barium titanate ceramics synthesized using SPS readily lose oxygen due to reducing atmosphere because of high vacuum during sintering (see Eq. (6-1)). The charge imbalance due to large oxygen deficiency can be compensated by the reduction in Ti^{4+} to Ti^{3+} (see Eq. (6-2)).³⁸



During sintering, several factors such as sintering temperature, atmosphere, and heating and cooling rates can contribute to the extent of oxygen loss in the as-sintered BT ceramics. In the current study, comparing SPS BT (1050°C) with SPS BT (900°C), it can be suggested that a large amount of charge carriers such as oxygen vacancies, Ti^{3+} , and electrons in the sintered BT ceramic were readily induced due to higher sintering temperature (1050°C), and the observed CP resulted from polarization of the large amount of charge carriers under ac field (Figure 6-4 (C)). Similar to the SPS BT (1050°C), as-sintered MWS BT (1320°C) also exhibited CP with huge dielectric loss ($\tan \delta \sim 6.901$), and the maximum permittivity value achieved during the dielectric measurement was 301,484 at 27°C (Figure 6-4 (D)). In addition, the CP of MWS BT (1320°C) was dropped about one order of magnitude at 1 MHz. The resistivity of the as-sintered ceramics (Table 6-2) revealed that samples showing CP (SPS BT (1050°C) and MWS BT (1320°C)) are semiconductive while PS BT (1350°C) and SPS BT (900°C) are quite insulating. This also suggests that the induced large amount of charge carriers during sintering process may play significant role in achieving CP in BT ceramics. Although SPS sintering was performed under vacuum, MWS was conducted in air atmosphere, but at a significantly higher temperature than SPS. Interestingly, while the BT ceramics were synthesized by PS (1350°C) and MWS (1320°C) at comparable sintering temperatures and under similar atmosphere (air), colossal permittivity was only exhibited in the latter. Thus, it can be stated that apart from sintering atmosphere (reducing), high sintering temperature, and rapid heating rate play crucial roles in synthesizing BT ceramics with CP. While Valdez-Nava et al. showed CP for nanocrystalline BT ceramics (~300 nm grain size), the current investigation revealed

that CP can also be observed in microcrystalline BT ceramics ($\sim 1.3 \mu\text{m}$) synthesized by MWS.³⁸

Table 6-2. Dielectric properties and bulk resistivity of as-sintered MWS, SPS, and PS BT ceramics at room temperature and 1 kHz.

Sintering technique	Relative Permittivity	Dielectric Loss	Resistivity (M Ω ·cm)
MWS (1320°C)	301,484	6.901	0.56
SPS (900°C)	4,110	0.483	52.9
SPS (1050°C)	202,000	1.860	0.35
PS (1350°C)	2,359	0.030	>1,000

6.4 Effect of Annealing on Dielectric Properties of Microwave-Sintered BaTiO₃ Ceramics

It was observed that the as-sintered MWS BT has very high $\tan \delta$ value due to its conductive characteristic (Figure 6-4 (D)). Therefore, thermal annealing processes were performed in flowing air (10 SCFH) with the aim to reduce the conductivity and to recover insulating characteristics, although still maintaining high permittivity. Figure 6-5 shows the variation in relative permittivity and dielectric loss of the MWS BT ceramics as a function of annealing temperature. A significant change in the dielectric properties was observed upon annealing treatment. It can be seen that at the annealing temperature (900°C), a significant decrease in both permittivity and dielectric loss was observed relative to the as-sintered MWS BT ceramics (Figure 6-5). Although the as-sintered MWS BT showed relative permittivity of $\sim 301,000$ and dielectric loss of ~ 6.9 at 1 kHz and room temperature (27°C), a relative permittivity of $\sim 60,500$ with dielectric loss of ~ 0.123 was obtained when annealed at 900°C for 12 h (Table 6-3). Although a relative permittivity was decreased from $\sim 60,500$ to $\sim 36,000$, a low dielectric loss below

0.05 was achieved at further increased annealing temperature from 900°C to 950°C. As the annealing temperature increased from 950°C to 1100°C, the relative permittivity continued to decrease from ~36,000 to ~15,000 while keeping low dielectric loss values between 0.030 and 0.045 (Figure 6-5). Finally, when annealed at 1250°C for 24 h, almost fully annealed BT ceramic was obtained with the relative permittivity and dielectric loss of 1,257 and 0.031 (Table 6-3), respectively.

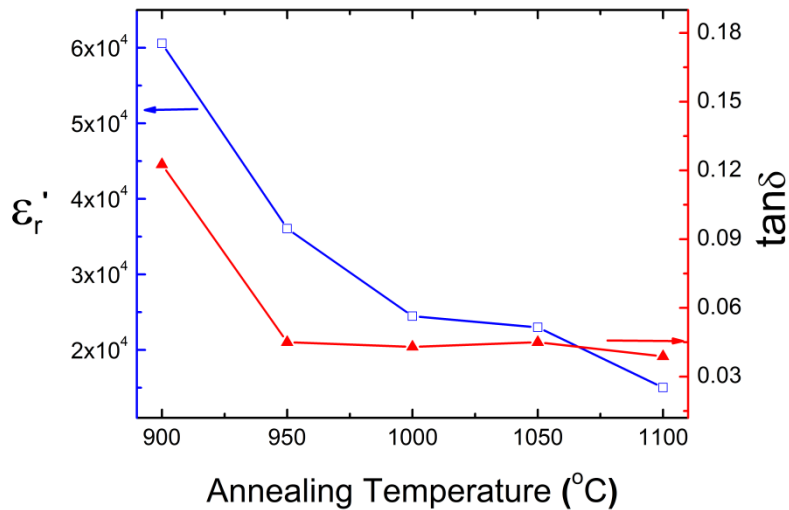


Figure 6-5. Effect of annealing on the dielectric properties of MWS BT (at 1 kHz and room temperature).

As mentioned previously, charge imbalance of reduced BT can be compensated by partial reduction in titanium (Eqs. (6-1) and (6-2)). Therefore, as BT reduced more, it has higher concentration of charge carriers and Ti^{3+} / Ti^{4+} ratio should be higher than less reduced BT. XPS results showed that the ratio of Ti^{3+} / Ti^{4+} were 0.023 and 0.016 for MWS BT samples annealed at 950°C and 1250°C, respectively. Thus, higher Ti^{3+} / Ti^{4+} ratio of MWS BT sample annealed at 950°C may indicate higher concentration of charge carriers and can explain observed high permittivity. Moreover, resistivity of annealed MWS BT samples was increased from 0.62 to 27 $M\Omega \cdot cm$ as annealing

temperature increased from 900°C to 1100°C. Resistivity up to 1 GΩ·cm was achieved when annealed at 1250°C for 24 h (Table 6-3). Thus, it can be stated that post sintering annealing process helps recover insulating properties of reduced semiconductive MWS BT ceramics to achieve high permittivity with low loss. The dielectric data and bulk resistivity for the annealed MWS BT are summarized in Table 6-3.

According to Heywang *et. al.*, noble metals tend to form Schottky junction with the surfaces of semiconducting barium titanate, and permittivity of the material can be increased via the extrinsic Schottky junction effect.¹⁰² Therefore, to test the effect of Schottky contact on high permittivity of annealed MW BT sample, I–V characteristic and dielectric property with various electrodes materials, including Au, Ag, Ni, and Al, were tested. The I–V curves showed that Au, Ag, and Ni formed Schottky junction while Al formed Ohmic contact with MWS BT sample annealed at 950°C for 12 h. Dielectric properties of the annealed MWS BT with various electrodes are listed in Table 6-4. The Extrinsic component could be estimated for the observed high permittivity of the annealed MWS BT by subtracting permittivity measured with Al electrode ($\epsilon'_r = 30,665$) from measured permittivity with Au electrode ($\epsilon'_r = 36,055$). The calculated result ($\epsilon'_r = 5,390$) implies that ~ 15 % of high permittivity of the annealed MWS BT ($\epsilon'_r = 36,055$) can be attributed to the extrinsic effect of Schottky junction between a metal contact (Au) and the surface of the semiconducting BT.

Figure 6-6 shows the temperature dependence of dielectric properties of the MWS BT ceramics for different annealing temperatures. Compared to the as-sintered MWS BT ceramics (Figure 6-4 (D)), sharp changes in relative permittivity values were

observed at T_c ($\sim 130^\circ\text{C}$) of BT ceramics, which is commonly observed in conventionally sintered (PS) BT ceramics.⁹⁹ Maximum relatively permittivity of 110,000 was achieved at 129.1°C in the MWS BT annealed at 950°C , which is 10 times higher than La-doped BT ($\epsilon'_{\text{max}} \sim 10,000$).¹⁰³ Dielectric losses of annealed BT were below 0.1 between room temperature (27°C) to 130°C (Figure 6-6).

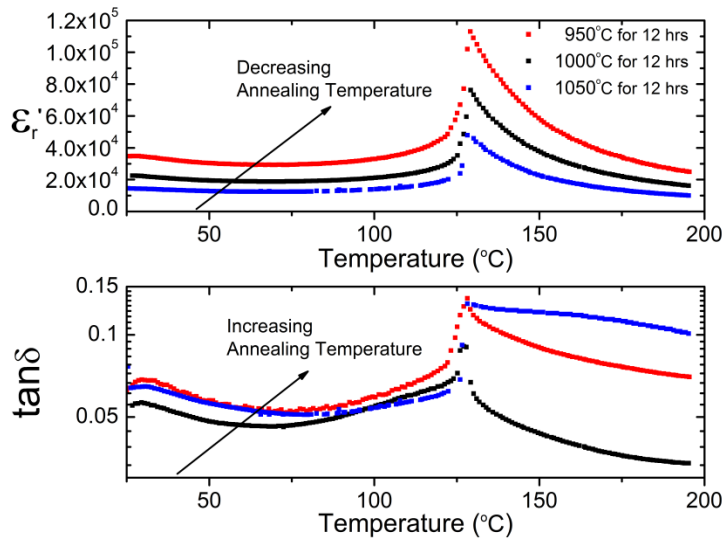


Figure 6-6. Dielectric properties (at 1 kHz) of MWS BT with different annealing temperatures (1050°C , 1000°C , and 900°C) for 12 hrs.

Frequency dependence of dielectric properties of annealed MWS BT sample (950°C for 12 h) in the temperature range from room temperature (27°C) to (233°C) is presented in Figure 6-7, where it can be seen that high dielectric constant was maintained up to 1 MHz at room temperature. However, it substantially decreased when frequency increased above 1 MHz. In addition, as temperature decreased, dielectric constant was dropped at lower frequencies and corresponding dielectric loss peaks were observed at the frequencies, which can be explained by Debye relaxation theory.⁵⁷ This is consistent with the origin of the high dielectric constant of the annealed MWS sample being the result of the interfacial polarization of charge carriers within

electrically inhomogeneous grains and grain boundaries. The precise mechanism of the origin of the CP in fast-fired BT ceramics will be discussed in the next chapter.

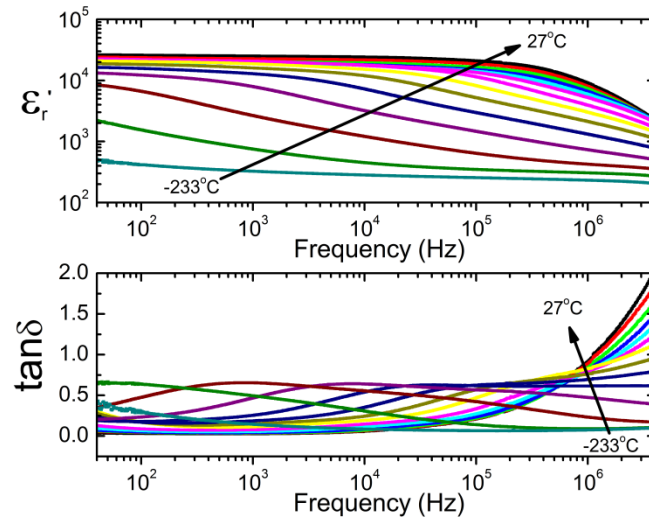


Figure 6-7. Dielectric properties of MWS BT annealed at 950°C for 12 hrs as a function of frequency in the temperature range from room temperature (27°C) to (-233°C).

Table 6-3. Effect of annealing on dielectric of MWS BT.

Annealing Temp (°C) / Time (hrs)	Permittivity / tanδ @ 1kHz and room temperature		Resistivity (MΩ·cm)
	Before Annealing	After Annealing	
900 / 12		60,584 / 0.123	0.62
950 / 12		36,055 / 0.045	1.75
1000 / 12	301,484 / 6.901	24,457 / 0.043	4.27
1050 / 12		22,990 / 0.045	7.62
1100 / 24		15,012 / 0.039	27.0
1250 / 24		1,257 / 0.031	>1,000

Table 6-4. Dielectric properties of the annealed MWS BT (950°C for 12 hours) with various electrodes (Au, Ag, Ni, and Al) at room temperature and 1 kHz.

Electrodes	Permittivity	tan δ
Au	36,055	0.04
Ag	8,189	0.07
Ni	27,543	0.10
Al	30,665	0.06

6.5 Conclusion

BT ceramics were synthesized using conventional pressureless sintering, SPS sintering, and MWS sintering techniques from nanocrystalline BT powder. For the first time, CP was observed in the MWS sintered BT ceramic sintered at 1320°C for 30 min. High sintering temperature and high heating rate of MWS were able to induce colossal permittivity in the sintered ceramics. There was no phase transition effect on permittivity change of as-sintered BT through MWS sintering. Post-sintering annealing treatments were performed to reoxidize the BT ceramics sintered by MWS with the aim to improve insulating characteristic while still maintaining high permittivity. The best dielectric properties ($\epsilon_r' > 10^4$ and $\tan\delta \sim 0.04$) of MWS sintered BT ceramics were achieved after annealing process at temperature range (950°C ~ 1100°C) for 12 ~ 24 hours.

CHAPTER 7
DIELECTRIC POLARIZATION MECHANISMS AND VARIABLE HOPPING
CONDUCTION IN FAST-FIRED BARIUM TITANATE CERAMICS

³7.1 Introduction

In this chapter, broadband dielectric spectroscopy analysis was performed on SPS BT ceramics in order to better understand and clarify the polarization mechanisms associated with CP of BT ceramic. Data analyses using Debye relaxation and Jonscher's UDR models were followed. In addition, bulk conduction mechanism in fast-fired barium titanate ceramics was determined based on various hopping conduction models. Furthermore, the contributions of each polarization mechanism to the colossal permittivity in SPS BT, such as a hopping polarization, IBLC effect, and electrode effect, were estimated by using experimental results.

7.2 Microstructure, Density, and XRD of Spark Plasma Sintered BaTiO₃ Using Co-Precipitated Nanocrystalline Powder

ICP-AES results show that starting BT powders synthesized by BaCl₂·2H₂O and TiCl₃ or BaCl₂·2H₂O and TiOCl₂ have Ba / Ti ratios of 0.95 (BT 0.95) and 1.00 (BT 1.00), respectively. Synthesized powders were sintered at 1150°C for 3 min. The sintered ceramics, SPS BT 0.95 and SPS BT 1.00 using BT 0.95 and 1.00 powders, were dark blue in color due to the reducing sintering atmosphere (vacuum) during SPS process.³⁷ The SEM images in Figure 7-1 shows the microstructures of freshly fractured surfaces of SPS BT 0.95 and SPS BT 1.00 ceramics with a respective average grain size of 56 ± 6 nm and 72 ± 8 nm. Grain sizes were measured by using the mean linear intercept

³ Reprinted with the permission from AIP Publishing LLC., *Journal of Applied Physics*, **113** 024102 (2013), titled "Origin of Colossal Permittivity in BaTiO₃ via Broadband Dielectric Spectroscopy," by H. Han, C. Voisin, S. Guillemet-Fritsch, P. Dufour, C. Tenailleau, C. Tuner, and J.C. Nino.

method of ASTM E112 standard.⁹⁸ As expected due to the fast-firing nature of SPS technique, no significant grain growth is observed after sintering and the grain sizes of the sintered ceramics are almost in the same size as the starting powders. Density measurement by Archimedes method reveals that the both sintered ceramics have theoretical densities up to 98 % (Table 7-1).

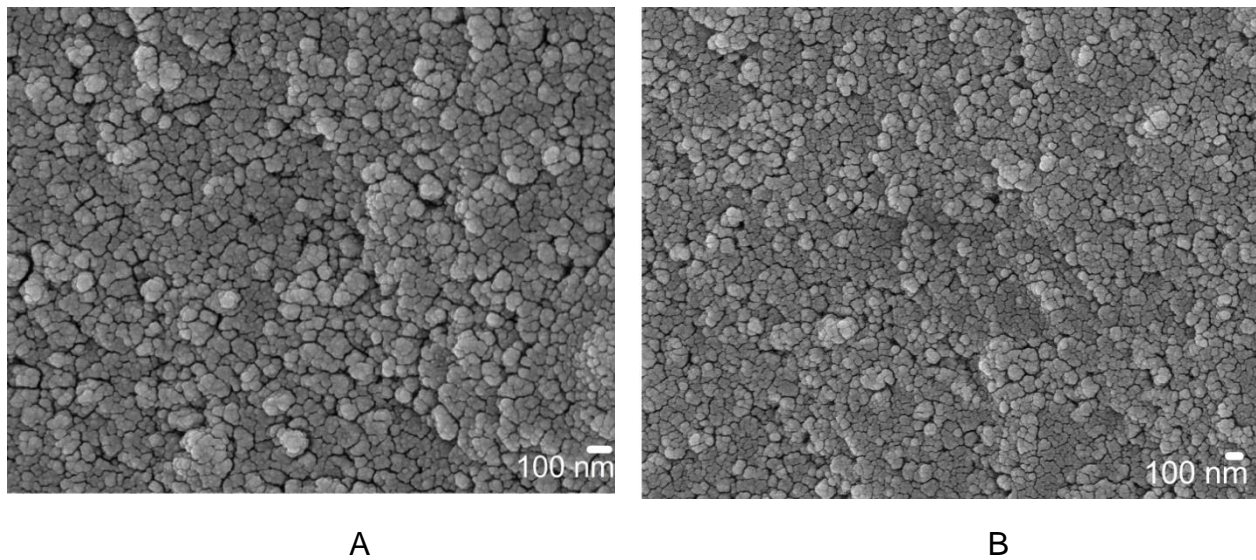


Figure 7-1. SEM images for A) SPS 0.95, and B) SPS 1.00 sintered ceramics.

The XRD patterns of the starting powders (BT 1.00 and BT 0.95) and the sintered ceramics (SPS BT 1.00 and SPS BT 0.95) are shown in Figure 7-2. No secondary phases are formed in BT 1.00 and SPS BT 1.00. However, secondary phases of BaTi_2O_5 (~ 5 vol % relative amount) and $\text{Ba}_4\text{Ti}_{12}\text{O}_{27}$ (~ 7 vol % relative amount) are observed for the Ti-rich BT 0.95 powder and SPS 0.95 ceramic, respectively. It is well known that $\text{Ba}_4\text{Ti}_{12}\text{O}_{27}$ phase is formed when Ti-rich BT powder is obtained under reduced (low P_{O_2}) conditions; here the reduction of a part of Ti^{4+} to Ti^{3+} give rise to the formation of $\text{Ba}_4\text{Ti}_2^{3+}\text{Ti}_{10}^{4+}\text{O}_{27}$.¹⁰⁴ Besides, both sintered ceramics of SPS BT 0.95 and 1.00 crystallized in a mixture of a cubic and a tetragonal perovskite

phases which can be demonstrated by the broadening of the (200) peak. On the contrary, all of the starting powders consisted of a single cubic phase (Figure 7-2). This result is also well in good agreement with previous results for SPS and MWS sintered ceramics in Chapter 6. Chemical composition, particle and grain sizes, theoretical density, crystal lattice, and phase purity for the starting powders and sintered ceramics are summarized in Table 7-1.

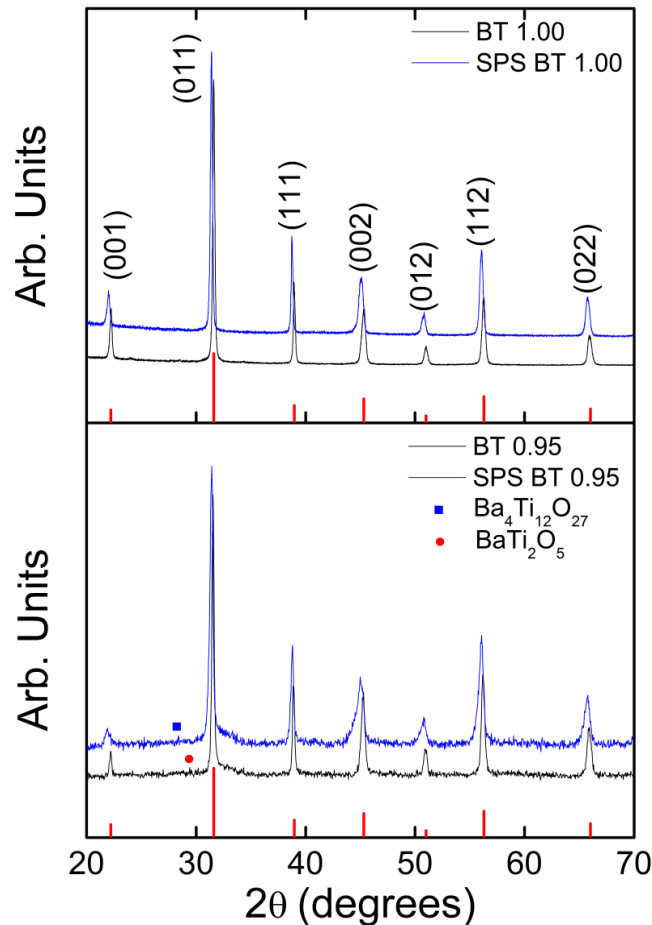


Figure 7-2. The X-ray diffraction patterns for the starting powders (BT 1.00 and 0.95) and the sintered ceramics (SPS BT 1.00 and 0.95).

Table 7-1. Summary of chemical composition, grain size and relative density of the sintered ceramics.

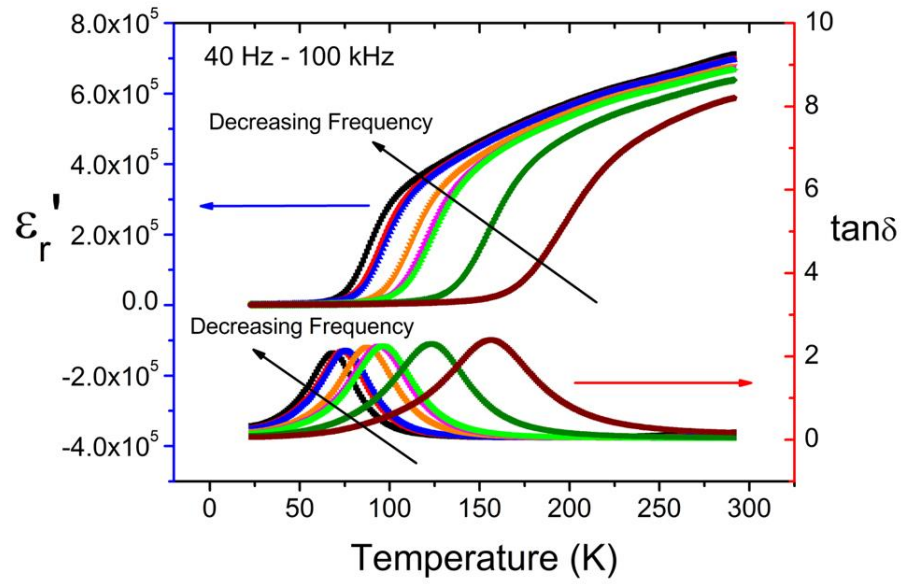
Samples	Ba/Ti ratio	Grain Size (nm)	Density (%)	Structure	2 nd Phase
---------	-------------	-----------------	-------------	-----------	-----------------------

SPS BT 0.95	0.95	56 ± 6	98	^{a)} C + ^{b)} T	Ba ₄ Ti ₁₂ O ₂₇ (~ 7 vol %)
SPS BT 1.00	1.00	72 ± 8	98	C+ T	None

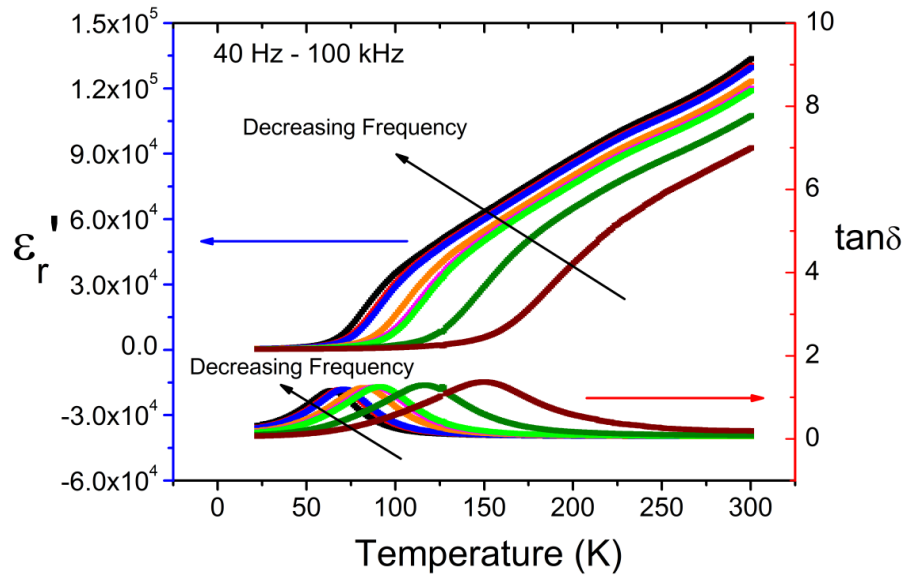
^{a)}C: cubic perovskite, ^{b)}T: tetragonal perovskite.

7.3 Broadband Dielectric Spectroscopy and Polarization Mechanism Investigation on Colossal Permittivity of Barium Titanate Ceramics

Relative permittivity and dielectric loss of SPS BT 0.95 and SPS BT 1.00 were measured as a function of temperature (25 K ~ 300 K) at different frequencies (40 Hz ~ 100 kHz), and the results are shown in Figure 7-3. Extremely high permittivity of up to 10^5 with low loss ($\tan \delta \sim 0.05$) is observed at room temperature in both samples. Table 7-2 shows dielectric properties of SPS BT 0.95 and SPS BT 1.00 at certain frequencies (1, 10, 100 kHz). The CP of the sintered ceramics decreases in a step-like shape as the temperature decreases, and the relative permittivity becomes independent of temperature below 50 K. This behavior is also found in a well-known high permittivity material CaCu₃Ti₄O₁₂ (CCTO).¹⁰⁵ The decrease of relative permittivity is accompanied by the dielectric loss peak at the given temperature, which indicates a temperature activated dielectric relaxation has occurred: the dielectric loss peaks appear at lower temperatures as frequencies decrease (Figure 7-3).



A



B

Figure 7-3. Dielectric property of A) SPS 0.95 and B) SPS 1.00 as a function of temperature (20 ~ 300 K).

Table 7-2. Dielectric property of SPS BT 0.95 and 1.00 at room temperature and 1, 10, and 100 kHz.

	1 kHz		10 kHz		100 kHz	
	ϵ'_r	$\tan \delta$	ϵ'_r	$\tan \delta$	ϵ'_r	$\tan \delta$
SPS BT 0.95	667,941	0.04	638,737	0.05	587,040	0.17
SPS BT 1.00	114,505	0.06	103,387	0.09	88,869	0.20

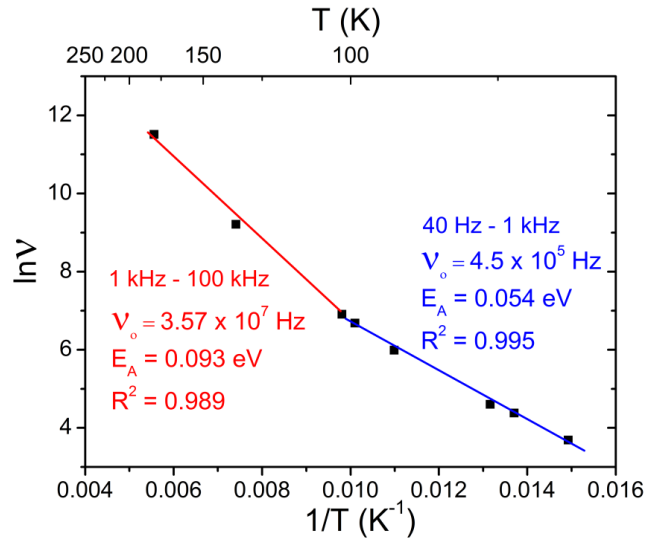
Generally, the Debye model can be used to describe the dielectric relaxation, and the relaxation frequency can be represented by,

$$\nu = \nu_o \exp\left(-\frac{E_A}{k_B T}\right) \quad (7-1)$$

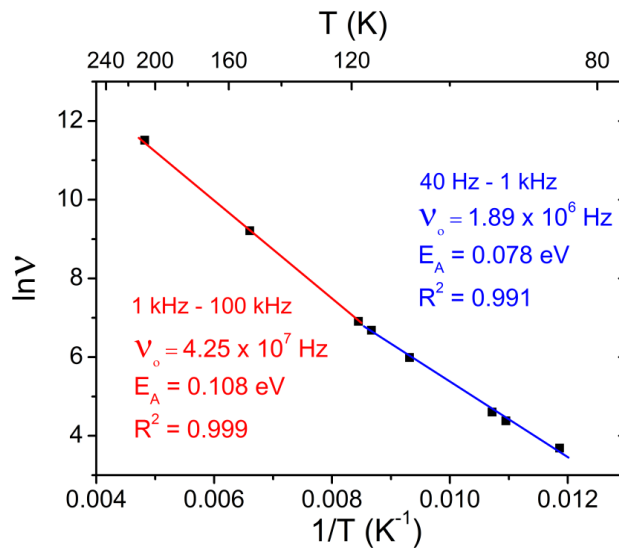
where ν_o , k_B , and E_A represent the pre-exponential factor, the Boltzmann constant, and the activation energy for relaxation, respectively.⁵⁷ The imaginary part of the dielectric response (ϵ''_r) is proportional to $\nu\tau / 1 + (\nu\tau)^2$, and the maxima of ϵ''_r occurs when $\nu\tau = 1$, where τ is the dielectric relaxation time. Thus, the relaxation temperatures at different frequencies can be extracted from the maximums of ϵ''_r and E_A can be calculated from the Arrhenius plot for Eq. (7-1).

As such, the ϵ''_r maxima for SPS BT 0.95 and 1.00 are determined from Figure 7-3 and the Arrhenius plots for the both samples are shown in Figure 7-4. The change in slope of the fitted curves for SPS BT 0.95 clearly indicates that two different thermally activated polarization mechanisms exist (Figure 7-4 (A)). By contrast, it is hard to distinguish a slope change for SPS BT 1.00 sample (Figure 7-4 (B)). The activation energies of 0.054 eV, 0.078 eV and the jump frequencies of 4.5×10^5 Hz, 1.89×10^6 Hz are obtained for SPS BT 0.95 and 1.00, respectively, in the low temperature region (30 K ~ 100 K), while 0.093 eV, 0.108 eV and 3.57×10^7 Hz, 4.25×10^7 Hz are calculated in

the high temperature region (100 K ~ 300 K) (Figure 7-4). Higher activation energy of the high temperature region is consistent with the co-existence of two polarization mechanisms.



A



B

Figure 7-4. Activation energy of thermally activated relaxations for A) SPS BT 0.95 and B) SPS BT 1.00.

As mentioned in Chapter 6, it has been widely investigated that reducing sintering atmosphere (vacuum) of SPS technique can cause high concentration of V_o^{**} , Ti^{3+} , and e' in the sintered ceramics.³⁷ Induced charged defects and electrons can be the localized charge carriers in the grain or at the grain boundary under the applied ac electric field. The origin of CP of barium titanate has been widely explained by the interfacial polarization effect by oxygen vacancies in the vicinity of grain boundaries and mobile electrons in the grains.^{37,106} However, it is also well known that the localized charge carriers can induce hopping dipoles in the material by polaron hopping such that can affect dielectric response of the material.¹⁰⁷ Thus, the second polarization mechanism of the CP in barium titanate could be attributed to a polaron hopping process in the grains. If that is the case, then the large change of activation energies in SPS BT 0.95 compared to SPS BT 1.00 (Figure 7-4 (A)) could be attributed to the higher concentration of polarons due to non-stoichiometric Ba / Ti ratio of SPS BT 0.95 sample.

To further investigate this hypothesis, the UDR model can be applied in order to investigate dielectric response due to localized charge carriers in the material.¹⁰⁸⁻¹¹¹ According to Jonscher's universal power law, the relative permittivity can be represented as a power law of ω^{s-1} resulting from the Kramers-Kronig transformation for a power law of the ac conductivity, ω^s (Eq. 3-76).¹¹¹ Therefore, relative permittivity (ϵ') can be written as,

$$\epsilon' = \tan(s\pi/2)\sigma_0 f^{s-1} / \epsilon_0 \quad (7-2)$$

where σ_0 and s represent the temperature dependent constants, and ϵ_0 and f denote the permittivity of free space and experimental frequency ($f = \omega / 2\pi$), respectively. Eq (7-2) also can be written as,

$$f\epsilon' = A(T)f^s \quad (7-3)$$

where $A(T) = \tan(s\pi/2)\sigma_0\epsilon_0$ and s is the constant value between 0 ~ 1. Thus, a straight line should appear in $\log_{10}(\epsilon'_r f)$ vs. $\log_{10}(f)$ plot at the given temperature, and the slope of the line indicates the value of s .

Figure 7-5 represents the $\log_{10}(\epsilon'_r f)$ vs. $\log_{10}(f)$ plot for SPS BT 0.95 at different temperatures (30 K ~ 300 K). A straight line does appear at high temperatures and low frequencies. However, the straight line is deviated from the slope as frequency increases due to relaxation, and consequently it decreases in a step-like shape and forms another straight line at the high frequency region. As temperature decreases, deviations from the slope are gradually occurred at lower frequencies as relaxation frequencies shift to lower frequencies at lower temperature (Figure 7-5). The values of s are found to be 0.98 and 0.95 when obtained from the slopes at high and low temperature regions, respectively. It should be noted that the value of s as closer to '1' indicates polarization charges that are more strictly localized.¹¹²

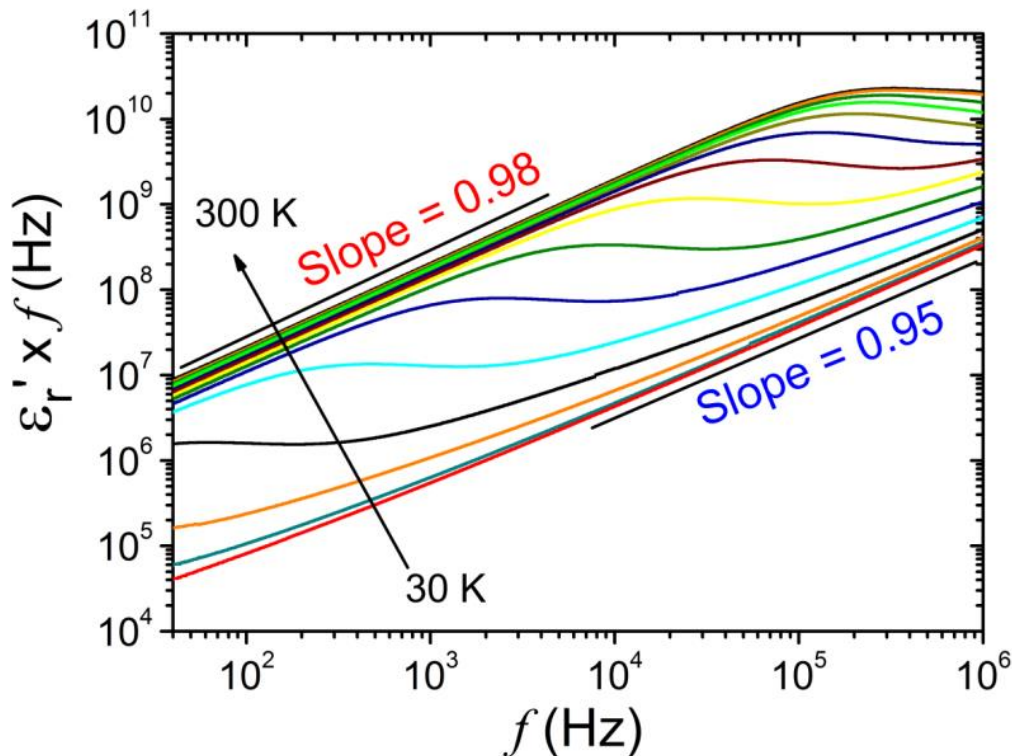


Figure 7-5. $\text{Log}_{10}(\epsilon_r' f)$ vs. $\text{log}_{10} f$ plot for the SPS (1150°C) BT at different temperatures (30 K ~ 300 K).

In the standard hopping polarization model, the value of s tends to increase and becomes closer to '1' as temperature decreases since the hopping dipoles freeze at low temperatures.¹¹² Interestingly however, it is shown here that for the CP of BT, the value of s decreases as temperature decreases, which means charge carriers for polarization are less localized at low temperatures when compared to high temperatures. This indicates that, while hopping polarization is becoming inactive at low temperatures due to insufficient energy to overcome energy barrier for polarization, interfacial polarization associated with mobile electrons in the grains and oxygen vacancies at the vicinity of the grain boundaries are still active as a polarization mechanism. Thus, the lower value of s may be due to the fact that the electrons for interfacial polarization are free to move

in the grains compared to hopped electrons with oxygen vacancies for hopping polarization.

Figure 7-6 shows the permittivity and dielectric loss change of the SPS BT 0.95 sample as a function of frequency (40 Hz – 1 MHz) at different temperatures (40 K – 300 K). At high temperatures, both polarization mechanisms (interfacial and hopping polarizations) are able to contribute to the CP of BT and form the upper plateau (Figure 7-6). As frequency increases, the permittivity decreases significantly with a correlated dielectric loss peak. This is consistent with dielectric relaxation as described by Debye theory,⁵⁷ where relaxation frequencies are also shifted to lower frequencies as temperature decreases.

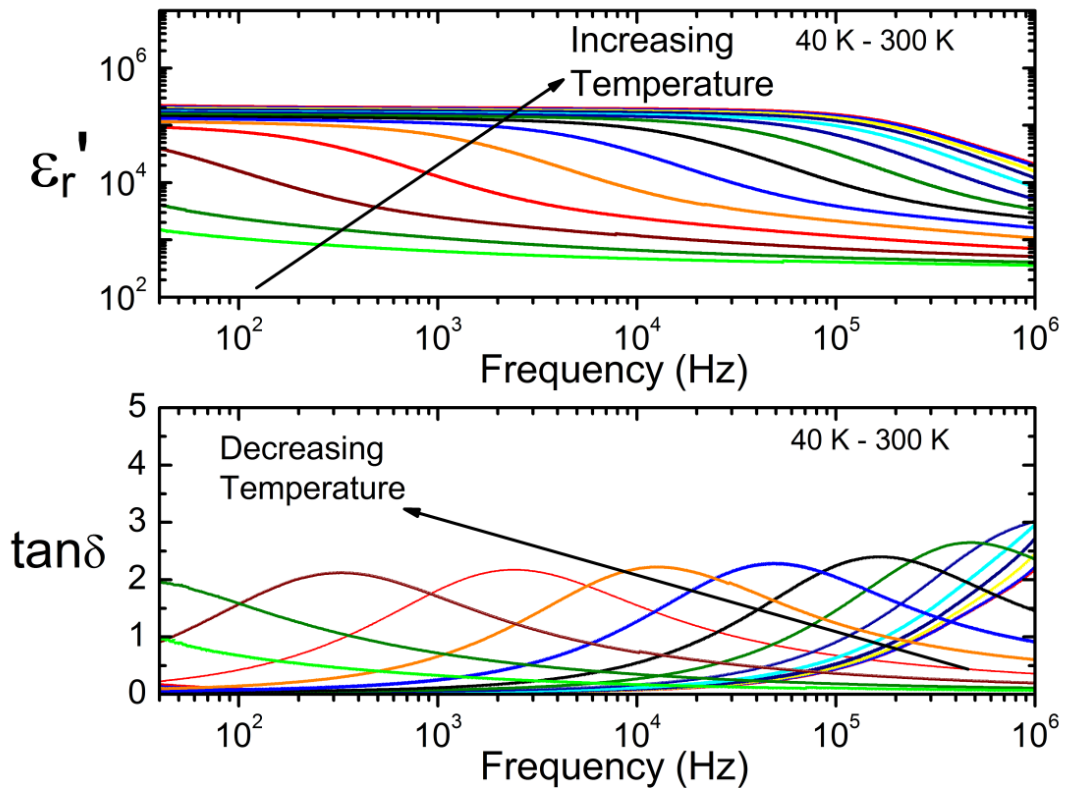


Figure 7-6. Dielectric properties of SPS BT 0.95 sample as a function of frequency (40 Hz – 1 MHz) at different temperatures (40 K – 300 K).

To further depict this behavior, the relative permittivity and dielectric loss of SPS BT 0.95 between 40 Hz ~ 1 MHz are separately shown in Figure 7-7 for representative temperatures across the range investigated (i.e. 300 K, 160 K, 100 K, and 30 K). It is observed that an extremely high permittivity of up to 2.4×10^5 and dielectric loss below 0.1 is achieved at 300 K between 40 Hz ~ 10 kHz. Here, the CP is maintained ($\epsilon'_r > 10^5$) up to 100 kHz, however, it drops significantly as frequency increases from 100 kHz to 1 MHz, and correspondingly dielectric loss shows sharp increases to $\tan \delta \sim 2.8$ (Figure 7-7 (A)); this physically meaningless value is rather a clear indication of the onset of conductivity at those higher frequencies.

By contrast, at low temperature, no CP is observed and for example, at 30 K, the highest permittivity is $\sim 1,000$. Moreover, the decrease in relative permittivity as the measuring frequency increases is markedly different when low and high temperature responses are compared. At high temperature (Figure 7-7 (A)), it is clear that the drop in permittivity undergoes two relaxation mechanisms with different characteristic frequencies, while at low temperature, only one relaxation mechanism with very low characteristic frequency is active (Figure 7-7 (D)). This further confirms that interfacial and polaron hopping polarizations contribute to the CP at high temperatures (300 K), however only interfacial polarization is active at low temperatures (30 K), which is consistent with the UDR analysis.

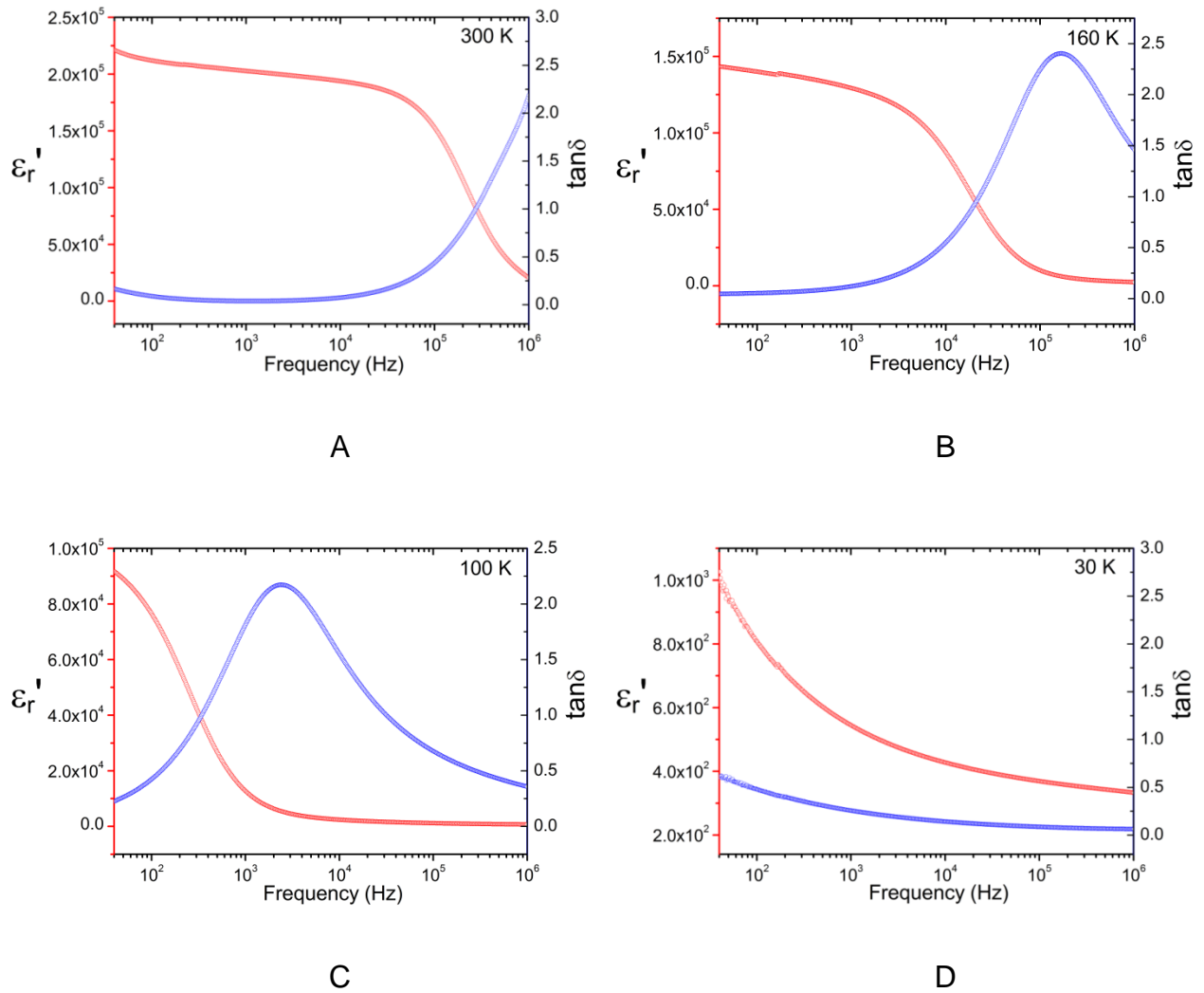


Figure 7-7. Dielectric properties of SPS BT 0.95 at A) 300 K, B) 160 K, C) 100 K, and D) 30 K in the frequency range of 40 Hz ~ 1 MHz.

Furthermore, to gain insight into the physical characteristics of the processes driving these relaxations, it is important to recall that in the thermally activated polaron hopping model, the maximum of the imaginary part of the relative permittivity, ϵ_r'' , is related to the number of hopping polarons by,

$$\epsilon_{\max}'' = N\mu^2 / 3k_B T \quad (7-4)$$

where N and μ represent the number of hopping polarons and the hopping dipole moment, respectively. N is exponentially dependent on the temperature, which can be written as,

$$N = N_0 \exp(-E_A / k_B T) \quad (7-5)$$

where N_0 is the pre-exponential factor and E_A is the activation energy associated with dielectric relaxation of hopping dipoles.^{113,114} Thus, substituting Eq. (7-5) into Eq. (7-4) results in,

$$T \epsilon''_{\max} = \frac{N_0 \mu^2}{3k_B} \exp(-E_A / k_B T) \quad (7-6)$$

The imaginary part of the relative permittivity for SPS BT 0.95 is plotted in Figure 7-8 as a function of frequency (40 Hz ~ 1 MHz) between 300 K ~ 100 K. The ϵ''_{\max} obtained for each temperature was then plotted in the Arrhenius form $\ln(\epsilon''_{\max} T)$ vs. $1/T$ to calculate the activation energy for hopping polarization (Figure 7-9). It is clear that two linear slopes appear with a transition temperature around 180 K. Accordingly, activation energies of 0.035 eV and 0.018 eV are calculated from the fitted line for high (300 K ~ 180 K) and low temperature (160 K ~ 100 K) regions, respectively. Not surprisingly ϵ''_{\max} increases as temperature increases, which further confirms that thermally activated polarization, associated with polaronic dipoles, is a contributing polarization mechanism to the CP of BT.

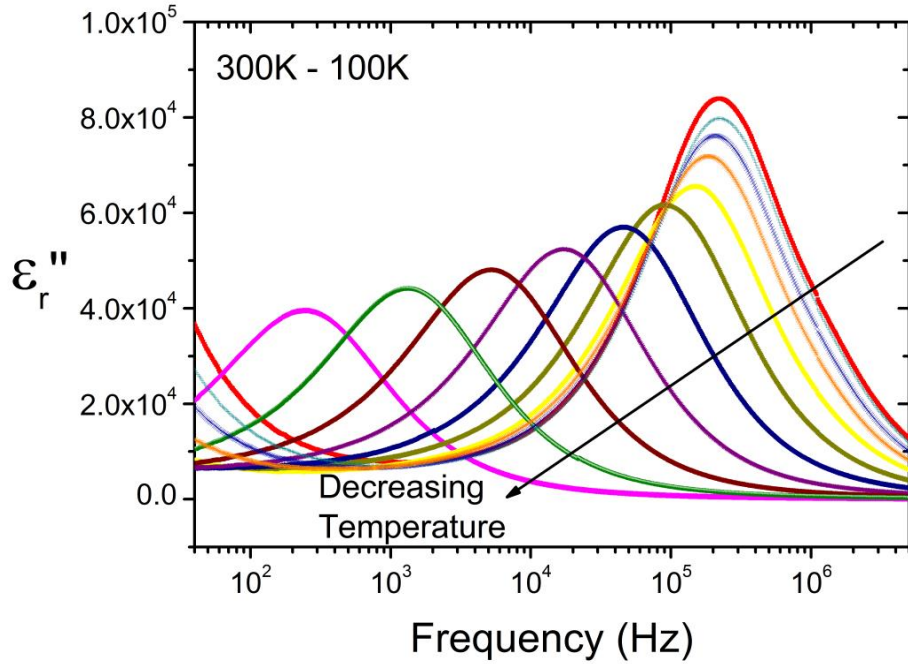


Figure 7-8. The imaginary part of the relative permittivity changes for SPS BT 0.95 as a function of frequencies (40 Hz ~ 1 MHz) at 300 K ~ 100 K.

More importantly, comparison between the activation energy for the high temperature (E_{AH}) and low temperature (E_{AL}) regions can reveal the activation energy for the different polarization mechanisms (similar to the analysis of the data in Figure 7-4) as follows:

$$E_{AH} = E_{AP} + E_{AI} \quad (7-7)$$

$$E_{AL} = E_{AI} \quad (7-8)$$

where E_{AP} and E_{AI} are the activation energies for hopping polarization and interfacial polarization in the CP of BT, respectively. From Figure 7-4 (A) E_{AH} and E_{AL} were calculated as 0.094 eV and 0.054 eV; using these values in Equation (7-7) and (7-8), E_{AP} of 0.039 eV and E_{AI} of 0.054 eV are obtained. These results are in good agreement with the calculated activation energy ($E_{AP} = 0.035$ eV) for high temperature region by

using the thermally activated polaronic model (Figure 7-9). All these results demonstrates that in addition to interfacial polarization mechanism, which has been widely accepted for the origin of CP in BT ceramics, a hopping polaron mechanism co-exists as an additional polarization mechanism contributing to the CP of BT ceramics.

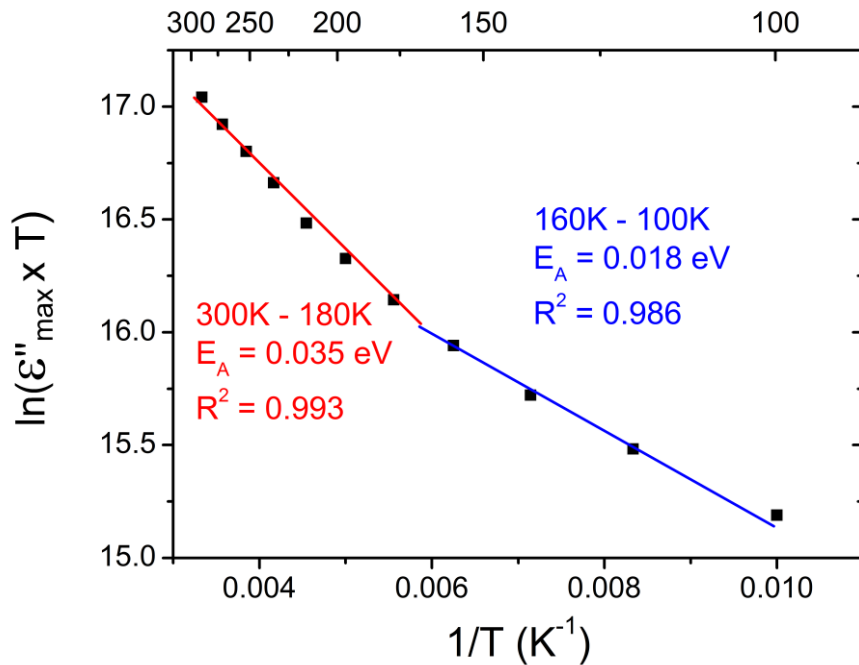


Figure 7-9. Activation energy for polaron hopping polarization at 300 K ~ 200 K.

7.4 Variable Range Hopping Conduction in Barium Titanate Ceramics Exhibiting Colossal Permittivity

Several techniques have been investigated to discover novel CP materials to be utilized in microelectronics, high energy density storage applications, and high performance dielectric devices.⁴¹⁻⁴⁸ However, a strong temperature and frequency dependency is commonly observed in dielectric properties of the CP materials, which limits the use of CP materials in conventional capacitive applications.¹¹⁵ It is widely accepted that in CP materials the temperature and frequency dependency of dielectric

properties is the result of extrinsic effects such as interfacial polarization and hopping conduction contributing to the bulk conductivity of the material.⁴⁹⁻⁵¹

Thus, understanding the fundamental mechanisms of the bulk conduction in CP materials is essential to tailor the temperature and frequency dependent dielectric response and thus fully realize their potential. Fundamental analyses of this kind have been attempted in the past for some CP materials such as CCTO and $\text{Ni}_{0.5}\text{Zn}_{0.5}\text{Fe}_2\text{O}_4$, but those results cannot be generalized to BT ceramics exhibiting CP.^{49,51}

In this chapter, a detailed analysis of the electrical conductivity of BT ceramics exhibiting CP is presented and a corresponding analytical model elucidating the conduction mechanisms is introduced. In addition, the relative contributions of the respective polarization mechanisms to the dc conductivity and the relative permittivity are estimated.

Figure 7-10 shows dielectric properties and the real part of ac conductivity (σ') for BT sintered by SPS technique (SPS BT) as a function of frequency (1 kHz – 4 MHz) at different temperature (110 K – 220 K). In Figure 7-10 (A), it is observed that CP up to 10^5 is maintained across a frequency range of 1 kHz – 100 KHz at 220 K. As frequency increases, a Debye type dielectric relaxation occurs, which is naturally accompanied by a dielectric loss peak at the relaxation frequency as expected (Figure 7-10 (B)). The relaxation frequency shifts to lower frequencies as temperature decreases. It is worth mentioning that a relative permittivity of 650 ~ 1150 was observed at 10 MHz in the measured temperature range presented here (110 K – 220 K). Also, the dielectric response at temperatures above 220 K to room temperature did not vary substantially

and was almost identical to that at 220 K. By contrast, the relative permittivity was significantly decreased to below 10^4 at temperatures lower than 110 K.

Towards a systematic analysis of this dielectric behavior, it is important to recall that according to Jonscher's UDR model, the conductivity of the material can be described as equation (7-9).¹¹⁶

$$\sigma'(f) = \sigma_{dc} + \sigma_0 f^s \quad (7-9)$$

where σ_0 and s are temperature dependent constants, f represents the experimental frequency ($f = \omega/2\pi$), and σ_{dc} is the dc conductivity. Figure 7-10 (C) shows the experimental conductivity data for SPS BT with fitted curves using equation (7-9). It can be observed that for a given temperature, two different types of response with characteristic frequency ranges occur. One range shows a strong decrease of the conductivity at low frequencies (below $\sim 10^4$ Hz),⁴⁹ however, in the high frequency range (above $\sim 10^4$ Hz), the conductivity of SPS BT shows low frequency dependence that can be well fitted by using the UDR model (equation (7-9)). Moreover, it should be noted that the exponent "s" obtained from the fitted curves is in around 0.50 ~ 0.64. Typically, it is understood that an "s" value closer to "0" indicates that charge carriers are more free to conduct through the material,¹¹⁶ while an "s" value between 0.5 and 0.8 is observed in materials with more localized charge carriers affecting not only conductivity but also the dielectric polarization of the material.^{116,117} In addition, σ_{dc} can be extracted at a given temperature from the fitted parameters using equation (7-9), which gives valuable information to understand conduction mechanisms in the material.

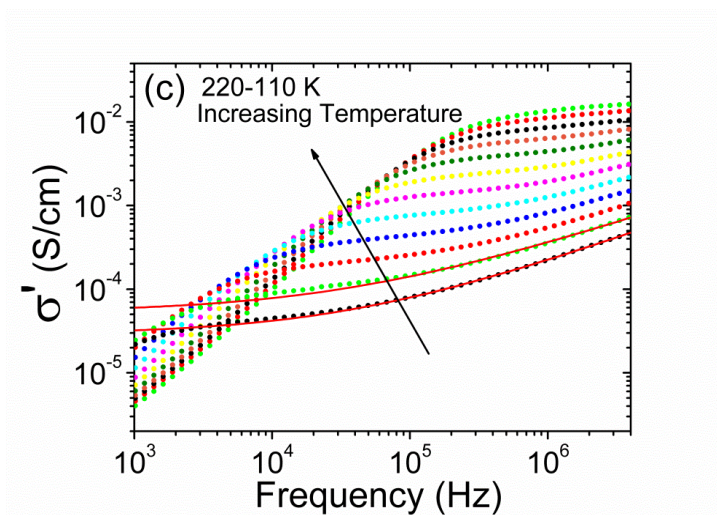
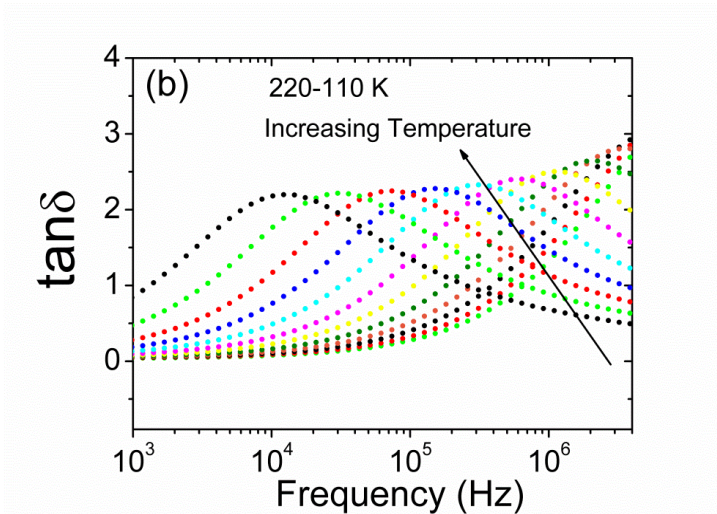
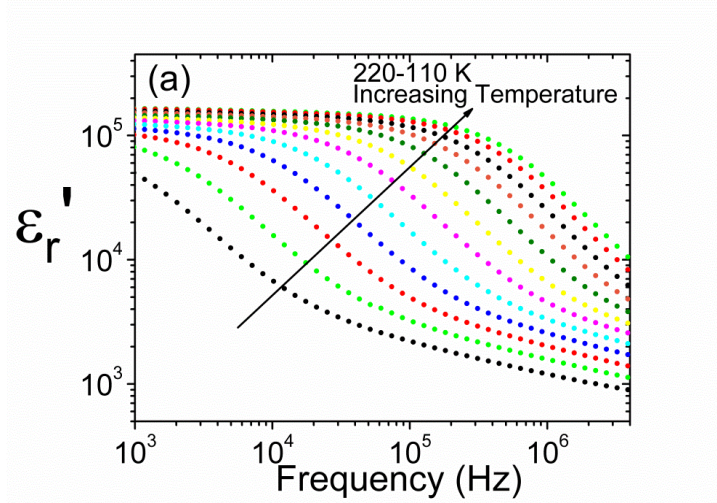


Figure 7-10. Dielectric properties and conductivity of SPS BT as a function of frequency (1 kHz ~ 4 MHz) at different temperatures (110 K ~ 220 K). A) The relative

permittivity. B) Dielectric loss. C) Conductivity.

In trying to understand the origin of these localized charges, it is worth remembering that materials sintered by fast-firing methods, such as SPS and MWS, are significantly reduced during the process.^{38,118,119} As such, a high concentration of oxygen vacancies, Ti^{3+} , and free electrons can be induced in the sintered ceramic. These anticipated charge carriers can then contribute to the conductivity of the material via long-range hopping conduction under applied electric field.

In hopping conduction, the dc conductivity of the material (σ_{dc}) can be well described by the Arrhenius equation described below

$$\sigma_{dc} = \sigma_1 \exp(-E_1 / k_B T) \quad (7-10)$$

where σ_1 is a constant and E_1 is the activation energy for hopping conduction.¹²⁰ In this model, hopping conduction always occurs through the neighboring sites, and hence the hopping range and activation energy are independent of temperature. This model is commonly referred to as the nearest-neighbor-hopping (NNH) conduction.^{120,121} In the NNH model, equation (7-10) can be applied to describe the temperature dependent σ_{dc} where the concentration of charge carriers for hopping conduction is temperature dependent. It is obvious from equation (7-10) that $\ln(\sigma_{dc})$ should have a linear relationship with $1/T$ for materials with a conduction mechanism following the NNH model. To test this model, σ_{dc} values extracted from each of the fitting curves in Figure 7-10 (C) were plotted as a function of inverse temperature ($1/T$), and are presented in Figure 7-11. It is clearly observed that σ_{dc} increases as temperature increases

indicating that thermally-activated bulk conduction exists in SPS BT. An activation energy of 112.5 ± 12.9 meV is obtained from the $\ln(\sigma_{dc})$ vs. $1/T$ plot.

However, contrary to the NNH model assumptions, Mott *et.al.* have pointed out that hopping conduction in certain materials would not process through the nearest site at low temperatures. According the theory proposed by Mott, the hopping range may vary as temperature decreases and become larger than the distance between neighboring sites due to the lower activation energy involved at lower temperatures. This model is generally referred to as Mott's variable-range-hopping (VRH) conduction. σ_{dc} that follows the Mott's VRH model can be represented as

$$\sigma_{dc} = \sigma_2 \exp[-(T_0 / T)^p] \quad (7-11)$$

$$T_0 = 24 / [\pi k_B N(E_F) \xi^3] \quad (7-12)$$

where σ_2 and T_0 are constants, ξ and $N(E_F)$ are the decay length of the localized wave function and the density of localized states at the Fermi level, respectively. The exponent p can be 1/4, 1/3, and 1/2 for different materials.^{121,122} According to equation (7-11), the linear relationship between $\ln(\sigma_{dc})$ and $1/T^p$ exists for the material following the VRH conduction mechanism.

In order to calculate the value of exponent “ p ” in equation (7-11), one should invoke the activation energy defining equation which is given by,¹²³

$$E_A = -d[\ln(\sigma_{dc})]/d(1/kT) \quad (7-13)$$

Most importantly, this equation also enables to investigate the activation energy of the bulk conductivity (E_A), regardless of a particular conduction mechanism. The inset in Figure 7-11 depicts the activation energies, calculated by using equation (7-13), as a

function of temperature. It is clearly shown that in Figure 7-11, E_A is temperature dependent, with E_A decreasing as temperature decreases. This result is in contradiction to the NNH conduction model, however consistent with the VRH theory, in which E_A is supposed to be variable as a function of temperature. Furthermore, it can be shown by comparing equation (7-13) and equation (7-11) that $1-p$ should be equal to the slope of $\log_{10} E_A$ vs. $\log_{10} T$ plot. As can be seen in the inset of Figure 7-11, the slope of ~ 0.5 is obtained from the linear fit of the $\log_{10} E_A$ vs. $\log_{10} T$ plot. Thus, it can be inferred that the most probable value of “p” in this case is $1/2$.

The temperature dependence of $\ln(\sigma_{dc})$ with respect to $1/T^{1/2}$ for SPS BT is represented in Figure 7-11. It is observed that the linear fit of $\ln(\sigma_{dc})$ against $1/T^{1/2}$ matches very well the experimental data over a whole range of temperature from 110 K to 220 K. It is important to note that compared to the NNH model, the linear relationship of σ_{dc} and temperature following the VRH model can more satisfactorily describe the experimental results in the whole range of temperatures, especially for the experimental data at low temperature regions. All these results support that the conduction mechanism in SPS BT follows VRH model rather than NNH model with the value of p as $1/2$, which is similar to the case of well-known CP materials, such as CCTO.⁴⁹

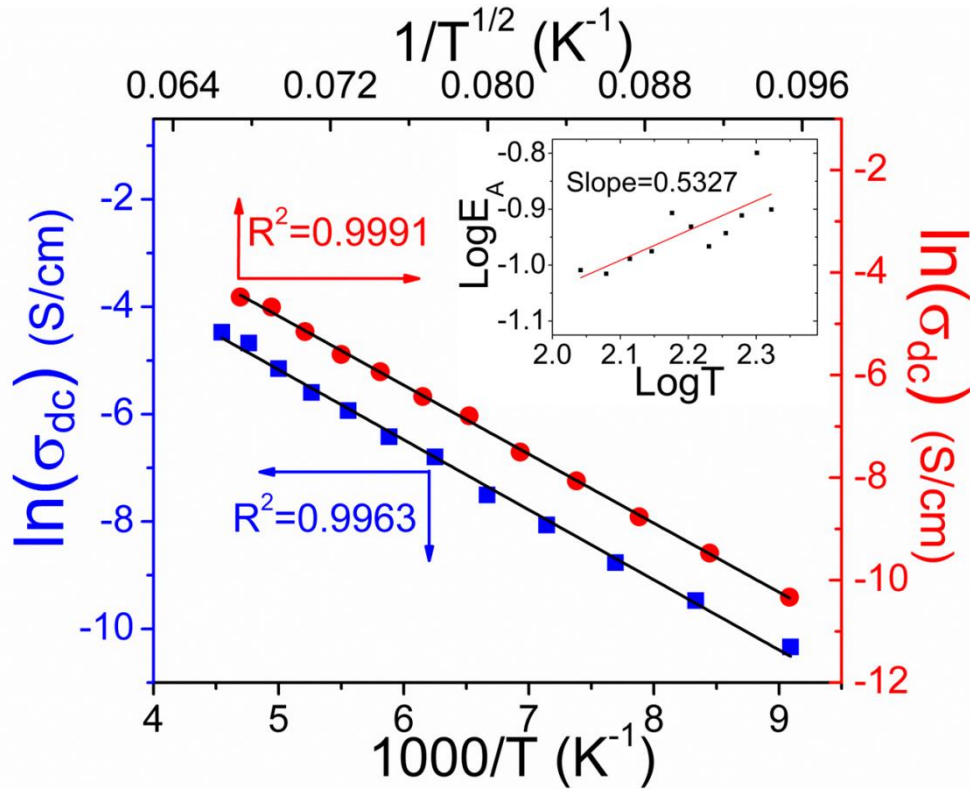


Figure 7-11. Temperature dependence of dc conductivity (σ_{dc}) with respect to $1/T$ and $1/T^{1/2}$. Black lines are the linear fits of the data.

In the VRH model, the activation energy (W) can be written as the following equation by substituting equation (7-11) into equation (7-13) .

$$W = 0.5k_B T_o^{0.5} T^{0.5} \quad (7-14)$$

From the fitted value of T_o (4.48×10^4 K), W can be calculated as a function of temperature, and the resulting values are shown in Figure 7-12. It is observed that W varies from 95.7 meV to 135.3 meV as temperature increases from 110 K to 220 K, which is well consistent with the activation energies calculated by using the defining equation, equation (7-13), ($E_A = 98.0 \sim 125.7$ meV at 110 K \sim 220 K). This also apparently suggests that the conduction mechanism in SPS BT follows the VRH model.

Furthermore, in the VRH model, it is possible to investigate the most probable hopping range (R) at a certain temperature by using the equation below,⁴⁹

$$R = \xi^{1/4} / [8\pi N(E_F) k_B T]^{1/4} \quad (7-15)$$

for SPS BT, ξ can be assumed as the distance between nearest Ti ions, which in the case of BT is approximately 0.40 nm. Using these values for T_0 and ξ , the density of localized states at the Fermi level can be estimated as $N(E_F) \cong 3.11 \times 10^{22} \text{ (eV}^{-1} \cdot \text{cm}^{-3}\text{)}$, which is three orders of magnitude higher than that of CCTO ($N(E_F) \cong 3.25 \times 10^{19} \text{ (eV}^{-1} \cdot \text{cm}^{-3}\text{)}$).⁴⁹ Then, the hopping range of R can be calculated for SPS BT as a function of temperature, which is also presented in Figure 7-12. It is found that R increases from 0.41 nm to 0.48 nm as temperature decreases from 220 K to 110 K. The hopping distance at 220 K for SPS BT is almost identical with the distance between nearest Ti ions, and it varies approximately 0.07 nm as temperature changes from 220 K to 110 K. It should be denoted that the variation of hopping distance for SPS BT is much less than that of other CP materials such as CCTO, which also follows the VRH conduction mechanism. For example, Lei Zhang *et. al.* have demonstrated that the hopping range of CCTO increases from 2.32 nm to 2.76 nm as temperature decreases from 180 K to 90 K.⁴⁹ The relatively high number of $N(E_F)$ and less variation of hopping range for SPS BT, compared to other CP materials, might be due to the high concentration of Ti^{3+} and oxygen vacancies existing in SPS BT, since the sample was sintered under severe reduction conditions (i.e., vacuum and fast heating rate).

Moreover, the activation energy for dielectric polarization (93 meV)¹¹⁵ of SPS BT calculated by using the Debye model is consistent with the activation energy of hopping conduction ($W \cong 90 \sim 120 \text{ meV}$) for the temperature range of 200 K \sim 100 K. This point to the possibility that an inherent correlation between bulk conduction and

polarization exists in SPS BT ceramics, which will be further demonstrated in the following discussions.

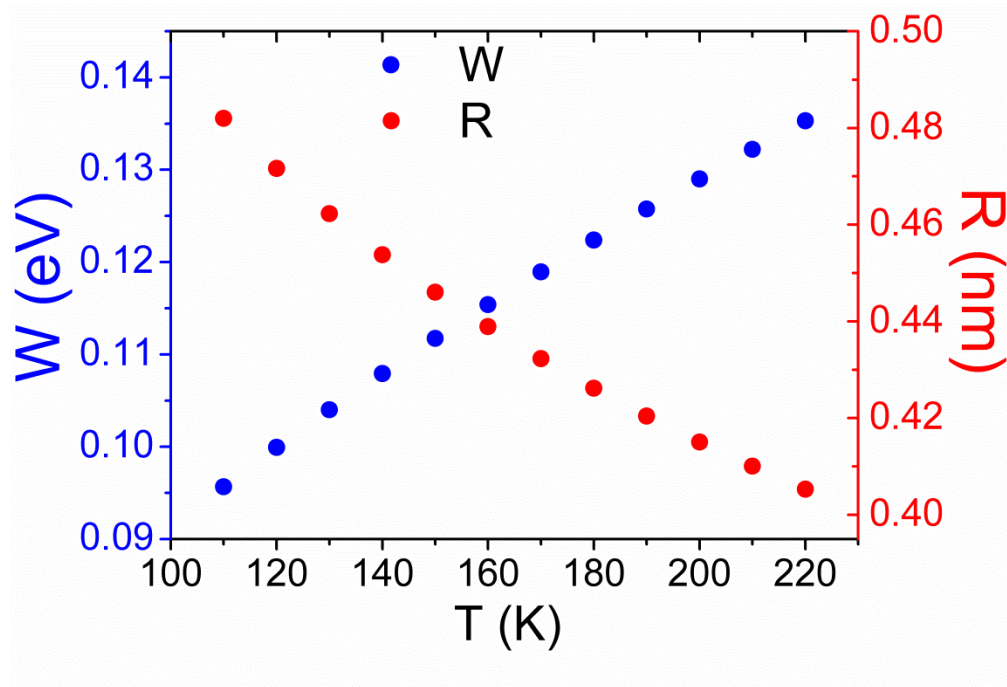


Figure 7-12. Activation energies and hopping distance as a function of temperature for VRH conduction in SPS BT.

7.5 Tailoring Contributions of Each Polarization Mechanism to Colossal Permittivity of Barium Titanate Ceramics

Recognizing that various polarization mechanisms are contributing to the observed CP, it is important to estimate their relative contribution. The dielectric response of CP materials can be well described by the Koop's equivalent circuit model.¹²⁴ In the Koop's equivalent circuit model, the grain and the grain boundary are supposed to be in series, and each component is composed of three parallel elements: a capacitance, a conductance, and a constant phase element (CPE). The analytical equation for this equivalent circuit can be driven as,⁵⁰

$$\epsilon_{BT}^* = \frac{[c_g(i\omega)^{1-p_g} + \sigma_{g,dc_j} + i\omega\epsilon_{BT,\infty}\epsilon_o][c_{gb}(i\omega)^{1-p_{gb}} + \sigma_{gb,dc_j} + i\omega\epsilon_{BT,\infty}\epsilon_o](1+\eta)}{i\epsilon_o\omega[c_{gb}(i\omega)^{1-p_{gb}} + \sigma_{gb,dc_j} + \eta\langle c_g(i\omega)^{1-p_g} + \sigma_{g,dc_j} \rangle] - \omega^2\epsilon_{BT,\infty}\epsilon_o^2(1+\eta)} \quad (7-16)$$

where $\sigma_{g(gb),dc_j}^*$ represent frequency independent part of the Jonscher's universal conductivity for grains (g) and grain boundaries (gb). ϵ_o , i , η and ω are the permittivity of the free space, the imaginary unit, $\sqrt{-1}$, the ratio of thickness of grain boundary to thickness of grain, and angular frequency ($= 2\pi f$), respectively. Also, $1-p_{g(gb)}$ is the exponent of angular frequency for the grains and the grain boundaries, and $c_{g(gb)}$ is equal to $\sigma_{g(gb),o} / [0.5\pi \cos(1-p_{g(gb)})]$ where $\sigma_{g(gb),o}$ is a prefactor. It is worth noting that in the model, the value of $p_{g(gb)}$ should be in between 0 and 1, and $p_{g(gb)}$ become closer to "1" for a more conductive response while a more capacitive response results in the $p_{g(gb)}$ value closer to "0".

The experimental data with theoretical fitted curves using equation (7-16) for the relative permittivity of SPS BT is shown in Figure 7-13. Additionally, Table 7-3 summarizes the fitting parameters used in equation (7-16). It is noticeable that the fitted curves are significantly in good agreement with the measured experimental data over the entire frequency range. Furthermore, $\sigma_{g,dc}$ is orders of magnitudes higher than $\sigma_{gb,dc}$, which is in accordance with the IBLC model (Table 7-3). As expected for the IBLC model, the value of p_g (≈ 0.91) is much closer to "1" compared to p_{gb} (≈ 0.03), which demonstrates that conductive grains and capacitive grain boundaries are present in SPS BT.

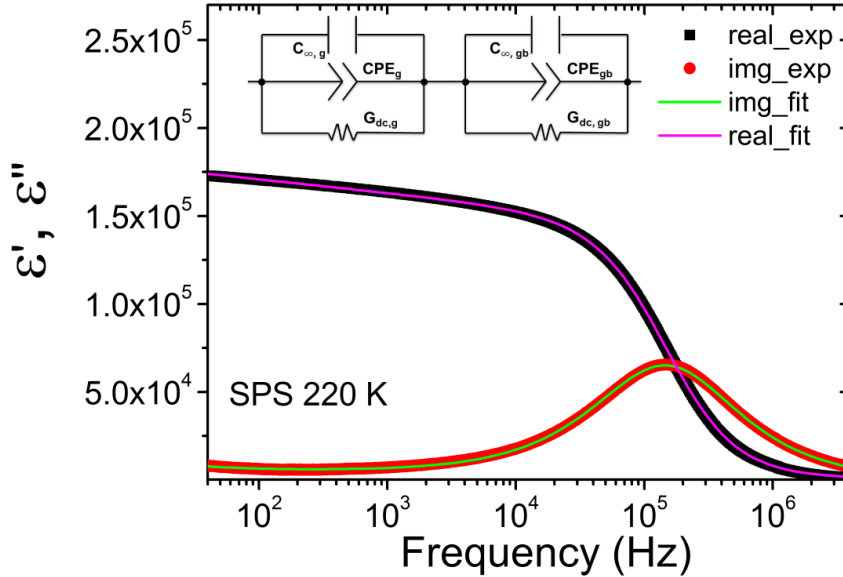


Figure 7-13. Experimental data with fitting data of the real and imaginary part of permittivity for SPS BT.

Table 7-3. Related fitting parameters for the SPS BT using Koop's equivalent circuit model.

Related parameters	SPS
C_g	0.32
C_{gb}	1.27×10^{-8}
ρ_g	0.90971
ρ_{gb}	0.02853
$\sigma_{g,dc}$ ($S \cdot cm^{-1}$)	1.39×10^{-3}
$\sigma_{gb,dc}$ ($S \cdot cm^{-1}$)	4.54×10^{-10}
η ($= t_b / t_g$)	0.0100
$\epsilon_{BT, \infty}$	494.03477

The contribution of interfacial polarization to the CP can be calculated by using the IBLC model, which can be presented by,

$$\epsilon_{eff} = \frac{\epsilon_r t_g}{t_b} \quad (7-17)$$

where ϵ_{eff} , ϵ_r , t_g , and t_b are the effective relative permittivity, relative permittivity of the material, grain size, and thickness of grain boundary, respectively. From the fitting

parameter in Table 7-3, relative permittivity (~ 494) and t_g/t_b (~ 100) are used to calculate the effective permittivity of SPS BT. An effective permittivity of 4.94×10^4 (equivalent to $\sim 28\%$ of the experimentally observed CP) is calculated for the SPS BT. It is important to note that this result is well agreeable with the experimentally calculated value. Relative permittivity of barium titanate ($\epsilon_r \sim 2,400$)¹²⁵, grain size (56 ± 6 nm, from Figure 7-1 (A)), and thickness of grain boundary (~ 1 nm)¹²⁶ were experimentally determined for SPS BT, and the contribution of interfacial polarization to the CP was calculated as 20.12 %.

Furthermore, as described in Chapter 6, the electrode effect due to Schottky junction between metal electrode and semiconductive surface of BT ceramics was estimated by subtracting permittivity measured with Al electrode from measured permittivity with Au. The calculation showed that about 15 % of the CP of SPS BT ceramics at low frequencies can be attributed to the extrinsic electrode effect. Moreover, the contribution of hopping polarization can also be obtained simply by subtracting the interfacial contribution from the total intrinsic permittivity resulting in $\sim 57\%$ of total relative permittivity.

It is interesting to note that the low loss ($\tan \delta \sim 0.05$) of SPS BT samples can be attributed to a thin re-oxidation layer on the surfaces associated with the short annealing treatment (850°C for 15 min). This is further confirmed as the measured dielectric loss of the samples is extensively increased ($\tan \delta > 1.00$) after polishing the surfaces. The surface of the samples become insulating after the short annealing process while the interior are still reduced (semi-conductive). This configuration is

comparable with a barrier layer capacitance (BLC) effect, and is able to effectively lower the dielectric loss while maintaining the high permittivity of sintered ceramics.

Thus, it can be stated that the origin of CP in BT ceramics is due to the combination effects of BLC (thanks to an insulating surface), interfacial polarization at the interior insulating grain boundaries, and hopping polarizations in semiconducting grains by a large number of induced charge carriers. These different contributions to the observed CP are schematically depicted in Figure 7-14.

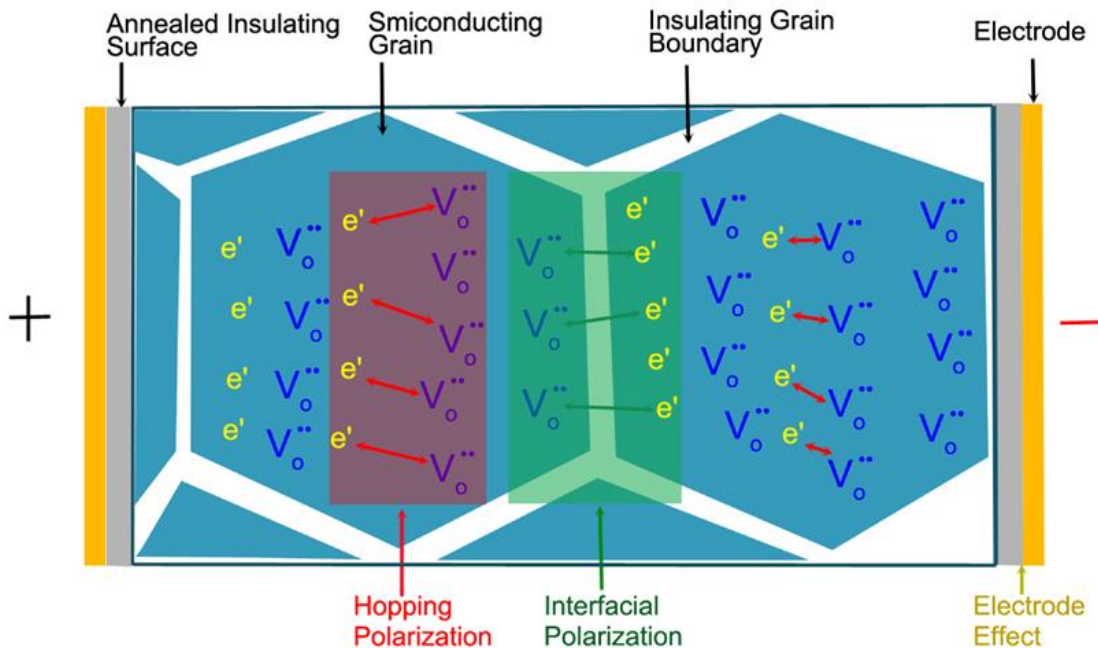


Figure 7-14. Interfacial and hopping polarization model for the colossal permittivity of BT ceramics.

7.6 Conclusion

BT ceramics with different Ba / Ti ratios (0.95 and 1.00) were synthesized by co-precipitation method and SPS sintering technique. Microstructure, chemical stoichiometry, and phase purity analyses were followed on sintered ceramics. Broadband dielectric spectroscopy was performed in order to reveal the polarization mechanisms in SPS BT ceramics. According to dielectric data analyses by Debye

relaxation and Jonscher's UDR models, in addition to interfacial polarization at insulating grain boundary, polarization due to polaron hopping was proposed as a co-existing polarization mechanism in the CP of BT ceramics. Analysis of the temperature dependent bulk dc conductivity reveals that the bulk conduction in fast-fired barium titanate is the result of VRH model rather than NNH model and the hopping distance was calculated as a function of temperature. Moreover, relative contributions of each polarization to the CP of BT ceramics were calculated as ~57 % hopping polarization, ~28 % interfacial polarization, and ~15 % electrode effect, respectively.

CHAPTER 8 SUMMARY AND FUTURE WORK

8.1 Summary

8.1.1 Defects and Electrical Property Relationships in BiI_3

Purification of the BiI_3 powder to a high level (6N) resulted in the overall improvement of properties of the BiI_3 detectors. Ultrapure powder with an impurity level of less than 10 ppm was synthesized by the PVT technique. The resistivity of the single crystals grown from the ultra-pure powder was found to be on the order of 10^{10} $\Omega\text{-cm}$ which is greater than the resistivity of crystals grown from commercial powder. An alpha particle spectrum (using a ^{241}Am source) was recorded at room temperature, using a prototype detector fabricated by using ultra-pure PVT powder. While the detector showed polarization effects, it constitutes as proof that room temperature detection using BiI_3 is possible and the improved resolution was observed in PVT BiI_3 detector compared to commercial BiI_3 detector. Electron mobility was estimated to be 433 ± 79 cm^2/Vs , hole mobility could not be estimated due to lack of signal generated by holes.

In order for improving the electrical properties of BiI_3 detectors, such as high resistivity, low leakage current, and radiation response, defect engineering was employed to reduce detrimental effects of iodine vacancies, based on proposed defect models for BiI_3 . DFT calculations and defect modeling verified that Sb dopants in BiI_3 can effectively reduce the formation and the migration of iodine vacancies by forming highly covalent bondings with surrounding ions or reducing jumping sites for iodine vacancies. Electrical and radiation detecting properties in the Sb-doped BiI_3 single crystal detector were significantly improved compared to undoped BiI_3 single crystal

detectors. Leakage current measurements and α -particle radiation response demonstrate that time-dependent detection properties were also remarkably enhanced in Sb-doped BiI_3 single crystal detector. In addition, the electron mobility of Sb-doped BiI_3 detector was significantly enhanced (~70 %) compared to that of undoped BiI_3 detector. Therefore, Sb-doped BiI_3 single crystals can now be considered realizable materials for gamma-ray detectors surpassing undoped BiI_3 based on enhanced electrical properties and long-term stability of the detector.

8.1.2 Colossal Permittivity in Fast-fired BaTiO_3

In the current work, BT ceramics were synthesized using conventional PS, SPS, and MWS sintering techniques from nanocrystalline BT powder. CP was observed in the SPS and MWS BT ceramics, sintered at 1050°C for 3 min and at 1320°C for 30 min, respectively. High sintering temperature and high heating rate of MWS were able to induce CP in the sintered ceramics. Post-sintering annealing treatments were performed to reoxidize SPS and MWS BT ceramics with the aim to improve insulating characteristic while still maintaining high permittivity. The best dielectric properties ($\epsilon' > 10^4$ and $\tan \delta \cong 0.04$) of SPS and MWS ceramics were achieved after annealing process at temperature 850°C for 15 min and 950°C ~ 1100°C for 12 ~ 24 hours, respectively.

Efforts were made on synthesizing SPS BT ceramics with specific Ba/Ti ratios (0.95 and 1.00). Dielectric spectroscopy demonstrated that sintered ceramics have CP up to $\sim 10^5$ at room temperature and 1 kHz. This CP can be maintained up to 100 kHz at room temperature. Onset of dielectric relaxation following Debye theory occurred as temperature decreased. Activation energy changes for relaxation indicate that at least

two different relaxational polarization mechanisms may be contributing the CP in fast-fired BT ceramics. According to Jonscher's UDR model, in addition to interfacial polarization at insulating grain boundary, hopping polarization due to induced defect dipoles was proposed as a co-existing polarization mechanism in the CP of BT ceramics. In addition, relative contributions of each polarization to the CP were calculated: ~57 % hopping polarization, ~28 % interfacial polarization, and ~15 % electrode effect.

Furthermore, in-depth analysis for revealing the conduction mechanism was conducted for the fast-fired BT ceramics, since defect dipoles are also attributed to bulk conductivity of the material which degrades its functional properties as dielectric material. The conduction mechanism in the fast-fired BT ceramics followed the variable-range-hopping (VRH) conduction mechanism rather than the nearest-neighboring-hopping (NNH) model. In addition, based on the Jonscher's UDR and Koop's equivalent circuit models, the dc conductivity and the relative permittivity of the fast-fired BT were deduced for each polarization mechanism.

8.2 Future Work

8.2.1 Defect Engineering of BiI₃: Controlling Atmospheric Pressure

It is well-known that changing the pressure of atmosphere will affect the defect formation, such as oxidation/reduction control in the oxide ceramics. Thus, in bismuth tri-iodide, iodine vacancy formation can be controlled by regulating iodine partial pressure through equation (8-1).



The equilibrium constant for this reaction can be represented as,

$$K_{V_i} = \frac{[V_i^\bullet] n P_{I_2}^{1/2}}{[I_i^X]} \quad (8-2)$$

since $[V_i^\bullet]$ is equal to n by the electroneutrality equation,

$$K_{V_i} = \frac{[V_i^\bullet]^2 P_{I_2}^{1/2}}{[I_i^X]}, [V_i^\bullet] \propto P_{I_2}^{-1/4} \quad (8-3)$$

Bismuth vacancy formation can be related with partial pressure of iodine by,



The equilibrium constant for bismuth vacancy formation can be established as,

$$K_{V_{Bi}} = \frac{[I_i^X]^6 [V_{Bi}''']^2 p^6}{P_{I_2}^3} \quad (8-5)$$

p needs to be same as $3[V_{Bi}''']$ for electroneutrality,

$$K_{V_{Bi}} = \frac{3^6 [I_i^X]^6 [V_{Bi}''']^8}{P_{I_2}^3}, [V_{Bi}'''] \propto P_{I_2}^{3/8} \quad (8-6)$$

Thus, the Kroger-Vink diagram for iodine and bismuth vacancies with respect to iodine partial pressure can be represented as

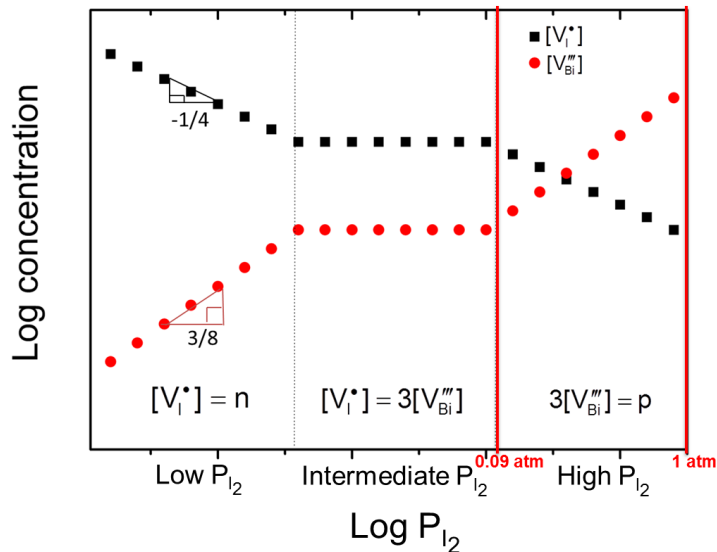


Figure 8-1. Kroger-Vink diagram for iodine and bismuth vacancies with respect to iodine partial pressure.

It is clearly shown in Figure 8-1 that the concentration of iodine vacancies can be controlled by changing the partial pressure of iodine vapor. The concentration of iodine vacancies are decreasing at high pressure region. Although the concentration of bismuth vacancies are increased at the expense of a decrease in iodine vacancies, provided that iodine vacancies are more mobile than bismuth vacancies, total conductivity could be reduced in terms of reduced iodine vacancies. At the melting point of BiI_3 (408°C), the maximum vapor pressure (0.09 atm) of iodine is calculated through equation (8-7).⁸²

$$\text{Log}P_{\text{I}_2} (\text{mmHg}) = -4310/T + 8.170, \quad (8-7)$$

Thus, the atmospheric pressure will be controlled between 0.09 atm to 1 atm by injecting iodine vapor into the single crystal growth chamber, and the effect of atmospheric pressure on the electrical properties of BiI_3 single crystals will be investigated.

8.2.2 Polarization Mechanism in (Nb+In) Co-doped TiO_2 Ceramics Exhibiting Temperature-frequency Independent Colossal Permittivity

Recently, Hu *et. al.* demonstrated that through novel defect engineering strategies, quasi-intrinsic CP (nearly temperature-frequency independent) can be achieved in (Nb + In) co-doped TiO_2 due to highly localized defect clusters.¹²⁷ Hopping distance of (Nb + In) co-doped TiO_2 remains constant at different temperatures due to highly localized defect-dipoles, which consequently gives rise to the excellent temperature-frequency-stable CP. While this approach suggested a promising strategy for the development of new high-performance CP materials, precise polarization mechanisms have not been determined on that material. Thus, detailed broadband dielectric spectroscopy analyzes following this work will be performed in order to reveal

polarization mechanisms in (Nb+In) co-doped TiO₂ ceramics and deduce CP in this material into respective intrinsic or extrinsic effects.

LIST OF REFERENCE

1. S.R. Phadke, C.R. Bowers, E.D. Wachsman, and J.C. Nino, "Proton Conduction in Acceptor Doped SnP_2O_7 ," *Solid State Ionics*, **183** [1] 26-31 (2011).
2. S. Omar, E.D. Wachsman, and J.C. Nino, "Higher Conductivity Sm^{3+} and Nd^{3+} Co-doped Ceria-based Electrolyte Materials," *Solid State Ionics*, **179** [33-34] 1951-1951 (2008).
3. S. Omar, E.D. Wachsman, and J.C. Nino, "Higher Ionic Conductive Ceria-based Electrolytes for Solid Oxide Fuel Cells," *Appl. Phys. Lett.*, **91** [14] (2007).
4. P. Caroff, K.A. Dick, J. Johansson, M.E. Messing, K. Deppert, and L. Samuelson, "Controlled Polytypic and Twin-plane Superlattices in III-V Nanowires," *Nat. Nanotechnol.*, **4** [1] 50-55 (2009).
5. A.A. Bonapasta and P. Giannozzi, "Defect Engineering in III-V Ternary Alloys: Effects of Strain and Local Charge on the Formation of Native Deep Defects," *Nucl. Instrum. Meth. B*, **186** 229-233 (2002).
6. A.A. Bonapasta and P. Giannozzi, "Defect Engineering in III-V Ternary Alloys: Effects of Strain and Local Charge on the Formation of Substitutional and Interstitial Native Defects," *Physica B*, **308** 846-849 (2001).
7. P.N.K. Deenapanray, A. Martin, and C. Jagadish, "Defect Engineering in Annealed n-type GaAs Epilayers Using $\text{SiO}_2/\text{Si}_3\text{N}_4$ Stacking Layers," *Appl. Phys. Lett.*, **79** [16] 2561-2563 (2001).
8. S. Ostapenko, "Defect Engineering in Polycrystalline Silicon Using Ultrasound," *Solid State Phenom.*, **67-8** 485-495 (1999).
9. R.M. Cohen, G. Li, C. Jagadish, P.T. Burke, and M. Gal, "Native Defect Engineering of Interdiffusion Using Thermally Grown Oxides of GaAs," *Appl. Phys. Lett.*, **73** [6] 803-805 (1998).
10. P. Kightley, R.I. Taylor, A.J. Moseley, P.D. Augustus, A.C. Marshall, and R.J.M. Griffiths, "Dislocation Engineering in Advanced III-V Device Structures," *Inst. Phys. Conf. Ser.*, [100] 187-192 (1989).
11. J. Lagowski and H.C. Gatos, "Defect Engineering in GaAs for Device Processing," *J. Electrochem. Soc.*, **134** [9] C576-C576 (1987).
12. V.Q. Nguyen, J.K. Kang, H.S. Han, H.Y. Lee, S.J. Jeong, C.W. Ahn, I.W. Kim, and J.S. Lee, "Bi-based Lead-free Ceramic Multilayer Actuators Using AgPd- $(\text{Na}_{0.51}\text{K}_{0.47}\text{Li}_{0.02})(\text{Nb}_{0.8}\text{Ta}_{0.2})\text{O}_3$ Composite Inner Electrodes," *Sensor Actuat. a-Phys.*, **200** 107-113 (2013).

13. J.G. Chen, G.X. Liu, X.T. Li, Z.J. Chen, and S.X. Dong, "High-Temperature Actuation Performance of BiScO₃-PbTiO₃ Ceramics and Their Multilayer Configuration," *IEEE T. Ultrason. Ferr.*, **60** [3] 446-450 (2013).
14. J. Wang, G. Elghoul, and S. Peters, "Lead Zirconium Titanate Alternatives for Nanoactuators," *IEEE T. Ultrason. Ferr.*, **60** [1] 256-260 (2013).
15. C.Y. Wu, X.P. Li, W.S. Li, B. Li, Y.Q. Wang, Y.T. Wang, M.Q. Xu, and L.D. Xing, "Fe₂O₃ Nanorods/Carbon Nanofibers Composite: Preparation and Performance As Anode of High Rate Lithium Ion Battery," *J. Power. Sources*, **251** 85-91 (2014).
16. Q. Wang, J. Zhao, W.F. Shan, X.B. Xia, L.L. Xing, and X.Y. Xue, "CuO Nanorods/Graphene Nanocomposites for High-performance Lithium-ion Battery Anodes," *J. Alloy. Compd.*, **590** 424-427 (2014).
17. B.H. Qu, L.L. Hu, Q.H. Li, Y.G. Wang, L.B. Chen, and T.H. Wang, "High-Performance Lithium-Ion Battery Anode by Direct Growth of Hierarchical ZnCo₂O₄ Nanostructures on Current Collectors," *Acs Appl. Mater. Inter.*, **6** [1] 731-736 (2014).
18. V.S. Puli, D.K. Pradhan, B.C. Riggs, D.B. Chrisey, and R.S. Katiyar, "Investigations on Structure, Ferroelectric, Piezoelectric and Energy Storage Properties of Barium Calcium Titanate (BCT) Ceramics," *J. Alloy. Compd.*, **584** 369-373 (2014).
19. L.F. Zhu, B.P. Zhang, W.G. Yang, N. Ma, X.K. Zhao, and L. Zhao, "High Piezoelectric Properties of (Ba,Ca)TiO₃-0.04LiF Ceramics Sintered at a Low Temperature," *J. Electroceram.*, **30** [1-2] 24-29 (2013).
20. M. Kuhn, S.R. Bishop, G. Ciampi, H.L. Tuller, W. Higgins, and K.S. Shah, "Ionic Conduction in TlBr - Impact of Te Acceptor Dopant Exsolution," *Solid State Ionics*, **241** 30-35 (2013).
21. H.L. Tuller, S.R. Bishop, D. Chen, Y. Kuru, J.J. Kim, and T.S. Stefanik, "Praseodymium Doped Ceria: Model Mixed Ionic Electronic Conductor with Coupled Electrical, Optical, Mechanical and Chemical Properties," *Solid State Ionics*, **225** 194-197 (2012).
22. S.R. Bishop, G. Ciampi, C.D. Lee, M. Kuhn, H.L. Tuller, W. Higgins, and K.S. Shah, "Ionic Conductivity of TlBr_{1-x}I_x (x=0, 0.2, 1): Candidate Gamma Ray Detector," *IEEE T. Nucl. Sci.*, **59** [5] 2424-2427 (2012).
23. S.R. Bishop, T.S. Stefanik, and H.L. Tuller, "Defects and Transport in Pr_xCe_{1-x}O_{2-delta}: Composition Trends," *J. Mater. Res.*, **27** [15] 2009-2016 (2012).
24. S.R. Bishop, H.L. Tuller, G. Ciampi, W. Higgins, J. Engel, A. Churilov, and K.S. Shah, "The Defect and Transport Properties of Acceptor Doped TlBr: Role of

- Dopant Exsolution and Association," *Phys. Chem. Chem. Phys.*, **14** [29] 10160-10167 (2012).
25. H.L. Tuller and S.R. Bishop, "Point Defects in Oxides: Tailoring Materials Through Defect Engineering," *Annu. Rev. Mater. Res.*, **41** 369-398 (2011).
 26. S.R. Bishop, T.S. Stefanik, and H.L. Tuller, "Electrical Conductivity and Defect Equilibria of $\text{Pr}_{0.1}\text{Ce}_{0.9}\text{O}_{2-\text{delta}}$," *Phys. Chem. Chem. Phys.*, **13** [21] 10165-10173 (2011).
 27. H.L. Tuller and S.R. Bishop, "Tailoring Material Properties through Defect Engineering," *Chem. Lett.*, **39** [12] 1226-1231 (2010).
 28. A.T. Lintereur, W. Qiu, J.C. Nino, and J. Baciak, "Characterization of Bismuth Tri-iodide Single Crystals for Wide Band-gap Semiconductor Radiation Detectors," *Nucl. Instrum. Meth. A*, **652** [1] 166-169 (2011).
 29. M. Matsumoto, K. Hitomi, T. Shoji, and Y. Hiratate, "Bismuth Tri-iodide Crystal for Nuclear Radiation Detectors," *IEEE T. Nucl. Sci.*, **49** [5] 2517-2520 (2002).
 30. D. Nason and L. Keller, "The Growth and Crystallography of Bismuth Tri-Iodide Crystals Grown by Vapor Transport," *J. Cryst. Growth.*, **156** [3] 221-226 (1995).
 31. F. Ayres, L.V.C. Assali, W.V.M. Machado, and J.F. Justo, "Role of Intrinsic Defects in the Electronic and Optical Properties of Alpha-HgI₂," *Appl. Phys. Lett.*, **88** [1] (2006).
 32. F. Ayres, W.V.M. Machado, J.F. Justo, and L.V.C. Assali, "Defects in Mercuric Iodide: an APW Investigation," *Physica B*, **340** 918-922 (2003).
 33. K. Biswas and M.H. Du, "First Principles Study of Native Defects in InI," *J. Appl. Phys.*, **109** [11] (2011).
 34. T.A. Kuku, "Ionic-Conductivity of SnI₂," *Solid State Ionics*, **20** [3] 217-222 (1986).
 35. Schoonma.J, "Role of Anion Vacancy Migration in Lead Halide Photolysis," *Solid State Commun.*, **13** [6] 673-676 (1973).
 36. T.B. Adams, D.C. Sinclair, and A.R. West, "Giant Barrier Layer Capacitance Effects in $\text{CaCu}_3\text{Ti}_4\text{O}_{12}$ Ceramics," *Adv. Mater.*, **14** [18] 1321-+ (2002).
 37. S. Guillemet-Fritsch, Z. Valdez-Nava, C. Tenailleau, T. Lebey, B. Durand, and J.Y. Chane-Ching, "Colossal Permittivity in Ultrafine Grain Size BaTiO_{3-x} and $\text{Ba}_{0.95}\text{La}_{0.05}\text{TiO}_{3-x}$ Materials," *Adv. Mater.*, **20** [3] 551-+ (2008).
 38. Z. Valdez-Nava, S. Guillemet-Fritsch, C. Tenailleau, T. Lebey, B. Durand, and J.Y. Chane-Ching, "Colossal Dielectric Permittivity of BaTiO_3 -based

- Nanocrystalline Ceramics Sintered by Spark Plasma Sintering," *J. Electroceram.*, **22** [1-3] 238-244 (2009).
39. M. Li, A. Feteira, and D.C. Sinclair, "Origin of the High Permittivity in $(\text{La}_{0.4}\text{Ba}_{0.4}\text{Ca}_{0.2})(\text{Mn}_{0.4}\text{Ti}_{0.6})\text{O}_3$ Ceramics," *J. Appl. Phys.*, **98** [8] (2005).
 40. D.C. Sinclair, T.B. Adams, F.D. Morrison, and A.R. West, "CaCu₃Ti₄O₁₂: One-step Internal Barrier Layer Capacitor," *Appl. Phys. Lett.*, **80** [12] 2153-2155 (2002).
 41. H.F. Hess, K. Deconde, T.F. Rosenbaum, and G.A. Thomas, "Giant Dielectric-Constants at the Approach to the Insulator-Metal Transition," *Phys. Rev. B*, **25** [8] 5578-5580 (1982).
 42. C.C. Homes, T. Vogt, S.M. Shapiro, S. Wakimoto, and A.P. Ramirez, "Optical Response of High-dielectric-constant Perovskite-related Oxide," *Science*, **293** [5530] 673-676 (2001).
 43. N. Ikeda, H. Ohsumi, K. Ohwada, K. Ishii, T. Inami, K. Kakurai, Y. Murakami, K. Yoshii, S. Mori, Y. Horibe, and H. Kito, "Ferroelectricity from Iron Valence Ordering in the Charge-frustrated System LuFe₂O₄," *Nature*, **436** [7054] 1136-1138 (2005).
 44. B.G. Kim, S.M. Cho, T.Y. Kim, and H.M. Jang, "Giant Dielectric Permittivity Observed in Pb-based Perovskite Ferroelectrics," *Phys. Rev. Lett.*, **86** [15] 3404-3406 (2001).
 45. S. Krohns, P. Lunkenheimer, C. Kant, A.V. Pronin, H.B. Brom, A.A. Nugroho, M. Diantoro, and A. Loidl, "Colossal Dielectric Constant up to Gigahertz at Room Temperature," *Appl. Phys. Lett.*, **94** [12] (2009).
 46. M. Shu-Nan and M. Maki, "Dielectric Anisotropy in the Charge-Density-Wave State of K_{0.3}MoO₃," *J. Phys. Soc. Jpn.*, **80** [8] (2011).
 47. C.C. Wang and L.W. Zhang, "Surface-layer Effect in CaCu₃Ti₄O₁₂," *Appl. Phys. Lett.*, **88** [4] (2006).
 48. J.B. Wu, C.W. Nan, Y.H. Lin, and Y. Deng, "Giant Dielectric Permittivity Observed in Li and Ti doped NiO," *Phys. Rev. Lett.*, **89** [21] (2002).
 49. L. Zhang and Z.J. Tang, "Polaron Relaxation and Variable-range-hopping Conductivity in the Giant-dielectric-constant Material CaCu₃Ti₄O₁₂," *Phys. Rev. B*, **70** [17] (2004).
 50. H. Zheng, L. Li, Z.J. Xu, W.J. Weng, G.R. Han, N. Ma, and P.Y. Du, "Ferroelectric/ferromagnetic Ceramic Composite and Its Hybrid Permittivity Stemming from Hopping Charge and Conductivity Inhomogeneity," *J. Appl. Phys.*, **113** [4] (2013).

51. H. Zheng, W.J. Weng, G.R. Han, and P.Y. Du, "Colossal Permittivity and Variable-Range-Hopping Conduction of Polarons in Ni_{0.5}Zn_{0.5}Fe₂O₄ Ceramic," *J. Phys. Chem. C*, **117** [25] 12966-12972 (2013).
52. W. Barsoum, *Fundamentals of Ceramics*, Taylor & Francis, 2002.
53. R.J.D. Tilley, *Defects in Solids*, Wiley, 2008.
54. F.A. Kroger and H.J. Vink, "Relations Between the Concentrations of Imperfections in Solids," *J. Phys. Chem. Solids*, **5** [3] 208-223 (1958).
55. W.C. Chueh and S.M. Haile, "Electrochemical Studies of Capacitance in Cerium Oxide Thin Films and Its Relationship to Anionic and Electronic Defect Densities," *Phys. Chem. Chem. Phys.*, **11** [37] 8144-8148 (2009).
56. W. Lai and S.M. Haile, "Impedance Spectroscopy as a Tool for Chemical and Electrochemical Analysis of Mixed Conductors: A Case Study of Ceria," *J. Am. Ceram. Soc.*, **88** [11] 2979-2997 (2005).
57. E. Barsouk and J.R. Macdonald, *Impedance Spectroscopy: Theory, Experiment, and Applications*, Wiley, 2005.
58. T.S. Stefanik and H.L. Tuller, "Nonstoichiometry and Defect Chemistry in Praseodymium-cerium Oxide," *J. Electroceram.*, **13** [1-3] 799-803 (2004).
59. R.A. De Souza and M. Martin, "Probing Diffusion Kinetics with Secondary Ion Mass Spectrometry," *Mrs. Bull.*, **34** [12] 907-914 (2009).
60. M. Yashima and T. Kamioka, "Neutron Diffraction Study of the Perovskite-type Lanthanum Cobaltite La_{0.6}Sr_{0.4}Co_{0.8}Fe_{0.2}O_{3-delta} at 1260°C and 394°C," *Solid State Ionics*, **178** [39-40] 1939-1943 (2008).
61. Y. Kuru, S.R. Bishop, J.J. Kim, B. Yildiz, and H.L. Tuller, "Chemomechanical Properties and Microstructural Stability of Nanocrystalline Pr-doped Ceria: An in Situ X-ray Diffraction Investigation," *Solid State Ionics*, **193** [1] 1-4 (2011).
62. E.D. Wachsman, N. Jiang, C.W. Frank, D.M. Mason, and D.A. Stevenson, "Spectroscopic Investigation of Oxygen Vacancies in Solid Oxide Electrolytes," *Appl. Phys. a-Mater.*, **50** [6] 545-549 (1990).
63. S.R. Rotman, H.L. Tuller, and C. Warde, "Defect-Property Correlations in Garnet Crystals .6. The Electrical-Conductivity, Defect Structure, and Optical-Properties of Luminescent Calcium and Cerium-Doped Yttrium-Aluminum-Garnet," *J. Appl. Phys.*, **71** [3] 1209-1214 (1992).
64. K.C. Kao, *Dielectric Phenomena in Solids*, Elsevier Science, 2004.

65. A.J. Moulson, J. Binner, R. Morrell, and I.o.C.B.S. Section, Electroceramics, Institute of Ceramics, 1988.
66. H.C. Hsueh, R.K. Chen, H. Vass, S.J. Clark, G.J. Ackland, W.C.K. Poon, and J. Crain, "Compression Mechanisms in Quasimolecular XI_3 ($X = As, Sb, Bi$) Solids," *Phys. Rev. B*, **58** [22] 14812-14822 (1998).
67. J. Trotter and T. Zobel, "Crystal Structure of SbI_3 and BiI_3 ," *Z. Kristallogr. Krist.*, **123** [1] 67-& (1966).
68. V.B. Timofeev and Vashchen.Vi, "Optical Properties of BiI_3 Single Crystals near Long-Wavelength Edge of Fundamental Absorption," *Opt. Spectrosc-Ussr.*, **24** [5] 396-& (1968).
69. Y. Kaifu and T. Komatsu, "Optical-Properties of Bismuth Tri-Iodide Single-Crystals .2. Intrinsic Absorption-Edge," *J. Phys. Soc. Jpn.*, **40** [5] 1377-1382 (1976).
70. T. Komatsu and Y. Kaifu, "Optical-Properties of Bismuth Tri-Iodide Single-Crystals .1. Interband-Transitions," *J. Phys. Soc. Jpn.*, **40** [4] 1062-1068 (1976).
71. T. Komatsu, Y. Kaifu, S. Takeyama, and N. Miura, "Effects of High Magnetic-Fields on Cationic Exciton Lines in BiI_3 ," *Phys. Rev. Lett.*, **58** [21] 2259-2262 (1987).
72. G.H. Kwei, A.C. Lawson, S.J.L. Billinge, and S.W. Cheong, "Structures of the Ferroelectric Phases of Barium-Titanate," *J. Phys. Chem-Us.*, **97** [10] 2368-2377 (1993).
73. W. Qiu, G.J. Dudder, X.Y. Zhao, S.S. Perry, and J.C. Nino, "Interfacial Reactivity of Au, Pd, and Pt on BiI_3 (001): Implications for Electrode Selection," *Acs Appl. Mater. Inter.*, **3** [6] 1910-1917 (2011).
74. P.E. Blochl, "Projector Augmented-Wave Method," *Phys. Rev. B*, **50** [24] 17953-17979 (1994).
75. G. Kresse and D. Joubert, "From Ultrasoft Pseudopotentials to the Projector Augmented-wave method," *Phys. Rev. B*, **59** [3] 1758-1775 (1999).
76. W. Kohn and L.J. Sham, "Self-Consistent Equations Including Exchange and Correlation Effects," *Phys. Rev.*, **140** [4A] 1133-& (1965).
77. G. Kresse and J. Furthmuller, "Efficient Iterative Schemes for ab Initio Total-energy Calculations Using a Plane-wave Basis Set," *Phys. Rev. B*, **54** [16] 11169-11186 (1996).
78. H.J. Monkhorst and J.D. Pack, "Special Points for Brillouin-Zone Integrations," *Phys. Rev. B*, **13** [12] 5188-5192 (1976).

79. S.R. Bishop, W. Higgins, G. Ciampi, A. Churilov, K.S. Shah, and L. Tuller, "The Defect and Transport Properties of Donor Doped Single Crystal TlBr," *J. Electrochem. Soc.*, **158** [2] J47-J51 (2011).
80. F.V. Motsnyi, S.S. Ishchenko, S.M. Okulov, and D.I. Bletskan, "Nature of Infrared Photoluminescence and of Doping of Layer Bismuth Iodide Single-Crystals," *Sov. Phys. Semicond.*, **11** [6] 617-620 (1977).
81. J.F. Condeles, R.C.Z. Lofrano, J.M. Rosolen, and M. Mulato, "Stoichiometry, Surface and Structural Characterization of Lead Iodide Thin Films," *Braz. J. Phys.*, **36** [2A] 320-323 (2006).
82. D. Cubicciotti and F.J. Keneshea, "The Vapor Pressures of BiI₃ over Liquid Bi-BiI₃ Solutions," *J. Phys. Chem-U.S.*, **63** [2] 295-297 (1959).
83. Z.H. Li, W.T. Li, J. Liu, B.J. Zhao, S.F. Zhu, H.P. Xu, and H. Yuan, "Improved Technique for HgI₂ Purification," *J. Cryst. Growth.*, **156** [1-2] 86-90 (1995).
84. D.M. Bercha, I.I. Nebola, S.I. Radautsan, N.N. Syrbu, V.K. Kiosev, and V.E. Tezlevan, "Photoelectric Properties of Ni-CdP₂ Schottky Barriers," *Sov. Phys. Semicond.*, **8** [11] 1343-1347 (1975).
85. R.D. Shannon, "Revised Effective Ionic-Radii and Systematic Studies of Interatomic Distances in Halides and Chalcogenides," *Acta Crystallogr. A*, **32** [Sep1] 751-767 (1976).
86. N.J. Podraza, W. Qiu, B.B. Hinojosa, H.X. Xu, M.A. Motyka, S.R. Phillpot, J.E. Baciak, S. Trolier-McKinstry, and J.C. Nino, "Band Gap and Structure of Single Crystal BiI₃: Resolving Discrepancies in Literature," *J. Appl. Phys.*, **114** [3] (2013).
87. D.J. Singh, "Structure and Optical Properties of High Light Output Halide Scintillators," *Phys. Rev. B*, **82** [15] (2010).
88. H. Yorikawa and S. Muramatsu, "Theoretical Study of Crystal and Electronic Structures of BiI₃," *J. Phys-Condens. Mat.*, **20** [32] (2008).
89. J.E. Baciak and Z. He, "Long-term Stability of 1-cm thick Pixelated HgI₂ Gamma-ray Spectrometers Operating at Room Temperature," *IEEE T. Nucl. Sci.*, **51** [4] 1886-1894 (2004).
90. Y. Eisen and A. Shor, "CdTe and CdZnTe Materials for Room-temperature X-ray and Gamma Ray Detectors," *J. Cryst. Growth.*, **184** 1302-1312 (1998).
91. A. Owens and A. Peacock, "Compound Semiconductor Radiation Detectors," *Nucl. Instrum. Meth. A*, **531** [1-2] 18-37 (2004).

92. J.E. Baciaak and Z. He, "Spectroscopy on Thick HgI₂ Detectors: A Comparison Between Planar and Pixelated Electrodes," *IEEE T. Nucl. Sci.*, **50** [4] 1220-1224 (2003).
93. Z. He, G.F. Knoll, and D.K. Wehe, "Direct Measurement of Product of the Electron Mobility and Mean Free Drift Time of CdZnTe Semiconductors Using Position Sensitive Single Polarity Charge Sensing Detectors," *J. Appl. Phys.*, **84** [10] 5566-5569 (1998).
94. J.G.P. Binner and I.A.H. Al-Dawery, "Bulk YBCO High-Tc Superconductors with Uniform and Full Oxygen Content via Microwave Processing," *Supercond. Sci. Tech.*, **11** [5] 449-457 (1998).
95. A. Goldstein and M. Kravchik, "Sintering of PZT Powders in MW Furnace at 2.45 GHz," *J. Eur. Ceram. Soc.*, **19** [6-7] 989-992 (1999).
96. Y.J. Wu, S.H. Su, J.P. Cheng, and X.M. Chen, "Spark Plasma Sintering of Barium Zirconate Titanate/Carbon Nanotube Composites with Colossal Dielectric Constant and Low Dielectric Loss," *J. Am. Ceram. Soc.*, **94** [3] 663-665 (2011).
97. J.D. Katz, "Microwave Sintering of Ceramics," *Annu. Rev. Mater. Sci.*, **22** 153-170 (1992).
98. H. Abrams, "Grain Size Measurement by the Intercept Method," *Metallography*, **4** [1] 59-78 (1971).
99. A. von Hippel, "Ferroelectricity, Domain Structure, and Phase Transitions of Barium Titanate," *Reviews of Modern Physics*, **22** [3] 221-237 (1950).
100. N.H. Chan and D.M. Smyth, "Defect Chemistry of Donor-Doped BaTiO₃," *J. Am. Ceram. Soc.*, **67** [4] 285-288 (1984).
101. K. Kinoshita and A. Yamaji, "Grain-Size Effects on Dielectric Properties in Barium-Titanate Ceramics," *J. Appl. Phys.*, **47** [1] 371-373 (1976).
102. W. Heywang, "Semiconducting Barium Titanate," *J. Mater. Sci.*, **6** [9] 1214-& (1971).
103. D.Y. Lu, M. Toda, and M. Sugano, "High-permittivity Double Rare-earth-doped Barium Titanate Ceramics with Diffuse Phase Transition," *J. Am. Ceram. Soc.*, **89** [10] 3112-3123 (2006).
104. S. Lee, C.A. Randall, and Z.K. Liu, "Comprehensive Linkage of Defect and Phase Equilibria through Ferroelectric Transition Behavior in BaTiO₃-based Dielectrics: Part 2. Defect Modeling Under Low Oxygen Partial Pressure Conditions," *J. Am. Ceram. Soc.*, **91** [6] 1753-1761 (2008).

105. M.A. Subramanian, D. Li, N. Duan, B.A. Reisner, and A.W. Sleight, "High Dielectric Constant in $ACu_3Ti_4O_{12}$ and $ACu_3Ti_3FeO_{12}$ phases," *J. Solid State Chem.*, **151** [2] 323-325 (2000).
106. M. Maglione, "Dielectric Relaxation of Space Charges and Polarons in Ferroelectric Perovskites," *Ferroelectrics*, **254** [1-4] 151-158 (2001).
107. Y.H. Li, L. Fang, L.J. Liu, Y.M. Huang, and C.Z. Hu, "Giant Dielectric Response and Charge Compensation of Li- and Co-doped NiO Ceramics," *Mater. Sci. Eng. B-Adv.*, **177** [9] 673-677 (2012).
108. A. Isnin and A.K. Jonscher, "Dielectric Response of Some Ferroelectrics at "low" Frequencies I," *Ferroelectrics*, **210** [1-4] 47-65 (1998).
109. A.K. Jonscher, "The Universal Dielectric Response and Its Physical Significance," *IEEE T. Electr. Insul.*, **27** [3] 407-423 (1992).
110. K.L. Ngai, A.K. Jonscher, and C.T. White, "Origin of the Universal Dielectric Response in Condensed Matter," *Nature*, **277** [5693] 185-189 (1979).
111. A.K. Jonscher, "Universal Dielectric Response," *Nature*, **267** [5613] 673-679 (1977).
112. A.S. Nowick and B.S. Lim, "Electrical Relaxations: Simple Versus Complex Ionic Systems," *Phys. Rev. B*, **63** [18] (2001).
113. L.L. Hench and J.K. West, *Principles of Electronic Ceramics*, Wiley, 1990.
114. S. Komine and E. Iguchi, "Relation of Conduction Changes and Magnetic Properties in $Nd_{1-x}Pb_xMnO_3$ ($0.10 \leq x \leq 0.25$)," *J. Phys-Condens. Mat.*, **16** [7] 1061-1073 (2004).
115. H. Han, C. Voisin, S. Guillemet-Fritsch, P. Dufour, C. Tenailleau, C. Turner, and J.C. Nino, "Origin of Colossal Permittivity in $BaTiO_3$ via Broadband Dielectric Spectroscopy," *J. Appl. Phys.*, **113** [2] (2013).
116. A.K. Jonscher, "Dielectric Relaxation in Solids," *J. Phys. D Appl. Phys.*, **32** [14] R57-R70 (1999).
117. S.R. Elliott, "AC Conduction in Amorphous-Chalcogenide and Pnictide Semiconductors," *Adv. Phys.*, **36** [2] 135-218 (1987).
118. D. Ghosh, H. Han, J.C. Nino, G. Subhash, and J.L. Jones, "Synthesis of $BaTiO_3$ -20wt% $CoFe_2O_4$ Nanocomposites via Spark Plasma Sintering," *J. Am. Ceram. Soc.*, **95** [8] 2504-2509 (2012).

119. H. Han, D. Ghosh, J.L. Jones, and J.C. Nino, "Colossal Permittivity in Microwave-Sintered Barium Titanate and Effect of Annealing on Dielectric Properties," *J. Am. Ceram. Soc.*, **96** [2] 485-490 (2013).
120. G.H. Jonker, "Analysis of the Semiconducting Properties of Cobalt Ferrite," *J. Phys. Chem. Solids*, **9** [2] 165-175 (1959).
121. N.F. Mott and E.A. Davis, *Electronic Processes in Non-Crystalline Materials*, OUP Oxford, 2012.
122. A.L. Efros and B.I. Shklovskii, "Coulomb Gap and Low-Temperature Conductivity of Disordered Systems," *J. Phys. C Solid State*, **8** [4] L49-L51 (1975).
123. S.S.N. Bharadwaja, C. Venkatasubramanian, N. Fieldhouse, S. Ashok, M.W. Horn, and T.N. Jackson, "Low Temperature Charge Carrier Hopping Transport Mechanism in Vanadium Oxide Thin Films Grown Using Pulsed dc Sputtering," *Appl. Phys. Lett.*, **94** [22] (2009).
124. C.G. Koops, "On the Dispersion of Resistivity and Dielectric Constant of Some Semiconductors at Audiofrequencies," *Phys. Rev.*, **83** [1] 121-124 (1951).
125. G. Arlt, D. Hennings, and G. Dewith, "Dielectric-Properties of Fine-Grained Barium-Titanate Ceramics," *J. Appl. Phys.*, **58** [4] 1619-1625 (1985).
126. Z. Valdez-Nava, C. Tenailleau, S. Guillemet-Fritsch, N. El Horr, T. Lebey, P. Dufour, B. Durand, and J.Y. Chane-Ching, "Structural Characterization of Dense Reduced BaTiO₃ and Ba_{0.95}La_{0.05}TiO₃ Nanoceramics Showing Colossal Dielectric Values," *J. Phys. Chem. Solids*, **72** [1] 17-23 (2011).
127. W.B. Hu, Y. Liu, R.L. Withers, T.J. Frankcombe, L. Noren, A. Snashall, M. Kitchin, P. Smith, B. Gong, H. Chen, J. Schiemer, F. Brink, and J. Wong-Leung, "Electron-pinned Defect-dipoles for High-performance Colossal Permittivity Materials," *Nat. Mater.*, **12** [9] 821-826 (2013).

BIOGRAPHICAL SKETCH

HyukSu Han was born in 1982 in Cheongju, Republic of Korea. He obtained his B.S. degree in materials science and engineering at Hanyang University, Seoul, Republic of Korea. He spent about one year (2008) researching in Dr. Hideo Hosono's group at Tokyo Institute of Technology as an exchange student. In 2010, he began his Ph.D. study in Dr. Juan C. Nino's research group at University of Florida (UF).